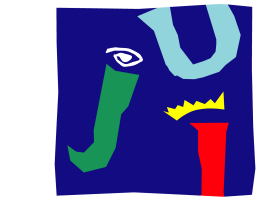

UNIVERSITAT JAUME·I

Doctoral School of Universitat Jaume I
Doctoral Programme in Science

TRAPPING FLEXURAL WAVES IN THIN ELASTIC PLATES BY COMPLEX ENGINEERED SURFACES

A dissertation submitted by Marc Martí Sabaté to obtain the degree of Doctor of Philosophy from Universitat Jaume I

MARC| MARTI| SABATE Firmado digitalmente por MARC|MARTI|SABATE Fecha: 2023.07.11 15:47:36 +02'00'

JESUS| LANCIS|SAEZ Firmado digitalmente por JESUS|LANCIS|SAEZ Fecha: 2023.07.11 16:44:39 +02'00'

DANIEL| TORRENT|MARTI Digitally signed by DANIEL|TORRENT|MARTI Date: 2023.07.11 15:51:01 +02'00'

AUTHOR
Marc Martí Sabaté

ADVISORS
Dr. Jesús Lancis Sáez
Dr. Daniel Torrent Martí

Castelló de la Plana, July 2023

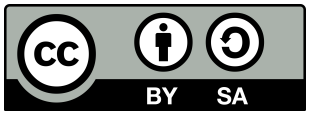

The author and supervisors specially thank Ministry of Science, Innovation and Universities of Spain for the financial support through the FPU program, under Grant No. FPU18/02725.

RESUM DE LA TESI DOCTORAL

Localització d'ones flexurals en plaques elàstiques fines mitjançant superficies dissenyades complexes

de

Marc Martí Sabaté
Doctor en Ciències per l'Escola de Doctorat en Ciències
Escola Superior de Tecnologia i Ciències Experimentals, ESTCE
Universitat Jaume I, Setembre 2023

L'objectiu d'aquest treball de tesi ha sigut el de dissenyar estructures geòmetriques de resonadors sobre una placa elàstica fina amb la finalitat de localitzar les ones mecàniques que es propaguen a través de la placa en un espai reduït. S'ha buscat aconseguir un gran nombre d'estats localitzats en un ampli rang de freqüències, doncs pot resultat atractiu per desenvolupar dispositius basats en el control de les ones mecàniques.

Els sistemes que es presenten al llarg d'aquest treball s'han analitzant utilitzant la teoria de la dispersió múltiple. Com els resonadors han sigut aproximats com interaccions resonants puntuals, aquesta teoria permet el seu anàlisi d'una manera adequada i fidel.

Primerament, s'ha estudiat un anàlog mecànic de les estructures coneguides com bicapes girades. Sistemes formats per dues xarxes periòdiques superposades les quals han sigut rotades amb un angle entre elles. Aquest tipus d'estructures ha despertat l'interès de la comunitat científica en els darrers anys degut a les seues extraordinàries propietats com conductor/aïllant. En aquest treball s'examina la possibilitat de descriure el comportament dels estats propis del sistema mitjançant la interacció de parells de resonadors.

Les distribucions quasiperiòdiques unidimensionals ofereixen la capacitat de confinar les ones que es propaguen pel medi i presenten una certa robustesa davant de problemes associats amb la fabricació, degut a la seua protecció topològica. En aquest treball s'ha mostrat la possibilitat d'implementar aquests principis en propagació bidimensional d'ones elàstiques mitjançant una estructura unidimensional, que permet simplificar el sistema necessari per confinar les ones i mostrar resultats similars als d'aquesta estructura aplicada en altres àmbits.

Finalment, s'ha estudiat i desenvolupat una solució per disseñar estats confinats en el continu (BICs) mitjançant una disposició circular de resonadors. Aquestes solucions de l'equació d'ona permeten obtenir modes amb un temps de vida infinit que no es propaguen per la resta del sistema, y que per tant presenten un confinament perfecte. Aquesta solució s'ha trobat tant per a ones flexurales en plaques elàstiques fines, com per a una guia d'ones bidimensional en acústica.

RESUMEN DE LA TESIS DOCTORAL

Localización de ondas flexurales en placas elásticas finas mediante superficies diseñadas complejas

de

Marc Martí Sabaté
Doctor en Ciencias por la Escuela de Doctorado en Ciencias
Escola Superior de Tecnologia i Ciències Experimentals, ESTCE
Universitat Jaume I, Septiembre 2023

El objetivo de este trabajo de tesis ha sido diseñar estructuras geométricas de resonadores sobre una placa elástica fina con el fin de localizar las ondas que se propagan a través de la placa en un espacio reducido. Se ha buscado producir un gran número de estados localizados en un rango amplio de frecuencias, pues puede resultar atractivo de cara a desarrollar dispositivos basados en el control de las ondas mecánicas.

Los sistemas que se presentan a lo largo del trabajo se han analizado utilizando la teoría de la dispersión múltiple, ya que los resonadores han sido aproximados como interacciones resonantes puntuales, y en ese caso, dicha teoría ha demostrado ser la más adecuada.

En primer lugar, se ha estudiado un análogo mecánico de las estructuras conocidas como bicapas giradas; sistemas formados por dos redes periódicas superpuestas las cuales han sido rotadas con un ángulo dado entre ellas. Este tipo de estructuras ha despertado el interés de la comunidad científica en los últimos años gracias a sus extraordinarias propiedades como conductor/aislante. En este trabajo se estudia la posibilidad de describir el comportamiento de los estados propios del sistema mediante la interacción de pares de resonadores.

Las distribuciones cuasiperiódicas unidimensionales ofrecen la capacidad de confinar las ondas que se propagan por el medio y presentan una cierta robustez ante problemas de fabricación debido a su protección topológica. Este trabajo ha demostrado la posibilidad de implementar estos principios en propagación bidimensional de ondas elásticas mediante una estructura unidimensional, simplificando el sistema necesario para confinar ondas y mostrando resultados similares a los de esta misma estructura aplicada en otros ámbitos.

Por último, se ha estudiado y desarrollado una solución para diseñar estados confinados en el continuo (BICs) mediante una disposición circular de resonadores. Dichas soluciones de la ecuación de ondas permiten obtener modos con un tiempo de vida infinito que no se propagan a través del resto del sistema, y que por tanto presentan un confinamiento perfecto. Dicha solución se ha hallado tanto para ondas flexurales en capas elásticas finas, como para una guía de ondas bidimensional en acústica.

ABSTRACT OF THE DOCTORAL THESIS

Trapping flexural waves in thin elastic plates by complex engineered surfaces

by

Marc Martí Sabaté
Doctor of Philosophy by the Science Doctoral School
Escola Superior de Tecnologia i Ciències Experimentals, ESTCE
Universitat Jaume I, September 2023

The main objective of this PhD thesis has been to design geometrical structures of resonators on top of a thin elastic plate for trapping waves that propagate through the medium in a reduced space. High density of modes in a wide frequency range is desired, as it can be appealing for developing mechanical wave control devices.

Structures discussed throughout this work have been analysed using multiple scattering theory. This mathematical tool has proved to be really adequate when treating with point-like interactions between resonators and the continuum medium, as is the case in our systems.

In the first place, a mechanical analogue for the twisted bilayer structure has been studied. This system is based on two periodic lattices superimposed with a relative rotation angle between them. It has recently attracted the attention of the scientific community due to its exotic properties as conductor/isolator. In this work, we will study a mechanism for describing the behavior of the eigenmodes of the structure based on the dimerized interaction between resonators.

Quasi-periodic one-dimensional distribution of scatterers offers the possibility of confining waves that propagate through the medium, and presents robustness against disorder based on its topological protection. This work has proven the possibility of confining mechanical waves in a two-dimensional space using one-dimensional quasi-periodic structures, simplifying the necessary system for confining waves and showing similar results to the same kind of structures applied in other domains.

Lastly, solutions for having bound states in the continuum (BICs) within a circular arrangement of scatterers have been studied and developed. These solutions to the wave equation allow to have infinite lifetime modes that do not propagate through the rest of the system, and therefore present perfect confinement. In this work, solutions have been found both for flexural waves in thin elastic plates, and for two-dimensional acoustic waveguides.

Contents

Chapter 1

Introduction

1.1 Motivation

The precise control of wave propagation and localisation plays a paramount role in contemporary applications reliant on the utilization of wave energy. Regardless of the specific field—acoustics, electronics or optics— there is a need for achieving meticulous control over the propagation of waves. Thus, the localisation of states emerges as a critical factor in the advancement of these applications. The capacity for confining the energy of the wave in a certain area opens up several possibilities for achieving enhanced sensitivity in sensing applications, wave-matter interaction or even wave emission. In the latter half of the 20th century, significant progress was made in developing a theory for wave localisation in random media. Notwithstanding, subsequent research has demonstrated the potential for confinement in deterministic systems as well [1], which can be seen advantageous in some aspects.

Throughout this document, we shall examine various mechanisms aimed at achieving the localisation of mechanical waves. With the exception of a proof of concept presented in airborne acoustics (Chapter 6), conceived structures will be implemented in thin elastic plates (thereby employing Kirchhoff-Love theory for flexural waves). These structures will consist of an arrangement of point-like resonators (mass-spring systems) attached to the upper surface of the plate. Our main goal is to achieve a high density of localized states within a frequency range, making them applicable to scenarios where trapped waves are required, while ensuring that the overall complexity and affordability of the structure are preserved. Simplicity is essential in applications characterized by high operational frequencies. In such cases, the wavelength is significantly small, increasing manufacturing costs and limiting technological capabilities for building complex systems.

Numerous contemporary applications require precise control over the energy carried by waves: optomechanics, for instance, which is the use of laser light to control the motion of mechanical vibrations, usually micrometre or nanometre scale resonators [2–6]. In the realm of quantum computing, the objective of manipulating single phonons has garnered attention [6–9]. Furthermore, there are some imaging applications, such as complex modulation of electromagnetic fields by means of phase changes due to mechanical vibrations. This work seeks to shed light on the types of structures that might facilitate advancements for these applications.

1.2 Background

Originally, the concept of localisation arose from the pursuit of understanding the metal-insulator transition, where "disorder" prevents the electrons in a semiconductor to move freely [10]. Building upon this notion, Anderson proposed his model for localisation of waves in random media by the end of the 1950s [11]. This seminal work initiated a new way of thinking, influencing numerous fields beyond its original domain (radiative transfer, seismology, atomic physics or high-energy physics). It has been at the origin of mesoscopic physics, which bridges the gap between microscopic and macroscopic scales [12].

Anderson localisation was traditionally associated with disorder and random lattices. However, in 1982, Shechtman made a groundbreaking discovery by providing evidence of the absence translational symmetry in a crystal [13]. This finding startled the solid state physics community and gave rise to many questions concerning the physics of quasicrystals. These systems were not new (they are the result of an extensive interdisciplinary effort that started with Greek philosophers and involved physicists, crystallographers and mathematicians; for those who want to keep track of this wonderful journey, I strongly recommend reading the introduction chapter in Senechal's *Quasicrystals and Geometry* [14]), but Shechtman's measurements were the first evidence of these structures in nature. In the following years, the ideas of localisation were tested for quasicrystals, expanding the theory of localisation to deterministic structures [1, 15].

These concepts transcended the solid state community and found application in classical wave systems. The milestone for the practical implementation of disordered systems and quasicrystals in optics and acoustics was the advent of metamaterials. The foundation for this advancement was laid to Veselago, who sought to solve the electromagnetic wave equation for a double negative material [16] (negative permittivity and permeability), and Pendry found a way of implementing such a material in practical settings [17, 18]. Metamaterials might be defined as 'an arrangement of artificial structural elements, designed to achieve advantageous and unusual properties' [19]. Although the conventional definition emphasizes electromagnetic properties, I intentionally adop a broader interpretation that encompasses all wave phenomena. Metamaterials are, therefore, the ideal framework for bridging concepts from solid state physics and quantum physics to classical wave propagation. Over the past two decades, researchers have actively pursued this apporach, demonstrating the existence of wave phenomena such as the quantum hall effect, chirality, slow light, topological protection, etc. in the realms of acoustics, mechanics and optics.

Besides, significant scientific advancements were made at the beginning of the 21st century, when a group of researchers successfully isolated a thin monolayer of graphite (graphene), and conducted comprehensive analyses on its properties [20]. The extraordinary characteristics of this two-dimensional material induced many researchers to work in that field, studying this structure or seeking analogues for mechanical and optical waves. In 2018, Jarillo's group [21, 22] achieved to experimentally stack two layers of graphene with a given relative angle that could be tuned. This new structure, called twisted bilayer graphene, exhibited transitions between insulating and conducting behaviors, depending on the precise angle of twist. The tunability of the system positions it as an ideal candidate for a wide range of modern applications. In recent years, researchers have also ventured into exploring mechanical and

optical counterparts of twisted bilayer structures, aiming to unveil extraordinary physical phenomena in alternative wave domains.

Lastly, there is another kind of wave localisation that has been known since the 1920s. Bound states in the continuum (BICs) were originally formulated by von Newmann and Wigner as solutions to the Schrödinger's equation in quantum mechanics [23]. These states represent solutions to the wave equation whose field is confined in space with an infinite lifetime while their energy lies within the continuous spectrum. Throughout the 20th century, numerous studies have been published, invesigating these solutions not only in the context of the Schrödinger equation but also for electromagnetic, acoustic or mechanical waves. Recently, due to technological advancements enabling new manufacturing possibilities, this field has regained attention, particularly in terms of the experimental measurement of these modes.

1.3 Objectives

As previously discussed, controlling the propagation of waves is of capital importance for the development of modern applications. In this sense, this work is going to focus on wave energy localisation in space. Specifically, some mechanical systems will be analysed using a thin plate as a continuous medium (supporting flexural waves) and a collection of mass-spring resonators attached on the upper plane of the plate. Different geometries will be conceived and analysed, seeking for a platform that allows us to have a high density of localized states in a straightforward manner. To achieve this goal, three systems are going to be compared: quasicrystals (modulated crystals), twisted bilayers and BICs. In order to compare these structures, some key questions need to be addressed:

- Which is the underlying mechanism responsible for wave localisation in the examined systems?
- To what extent is the proposed system compatible with real-world manufacturing processes, and does it exhibit robustness against potential defects?
- Can the system accommodate the required complexity for practical applications?

1.4 Outline

This thesis consists of the following chapters:

- **Chapter 2:** Multiple Scattering Theory (MST) for flexural waves in thin elastic plates. This chapter sheds light on the physics underlying the deformation of solids under stress, specifically flexural waves in thin elastic plates (Love-Kirchhoff theory). Then, MST—a framework for taking into account interactions in many-body systems—is explained and applied to the described physical equations. Further discussions on incident fields, eigenmodes and resonances are also present in the chapter.

- **Chapter 3:** Dimerized localisation of waves in twisted bilayer crystal plates. Here, we apply the theory developed in the previous chapter to analyse the geometrical configurations known as twisted bilayers. Some theoretical discussion on the periodicity of these structures is commented, and numerical simulations are presented, focusing on those modes that can be explained by the interaction of few resonators in the cluster.

- **Chapter 4:** Quasi-periodic linear arrays of scatterers. In this chapter, we propose a different geometrical configuration for achieving localisation of flexural waves in thin plates. We have used a modulated array of resonators for generating aperiodic structures that map their spectra into a Hofstadter's butterfly feature. Edge states appear under some circumstances, and they are claimed to be topologically protected, making them robust enough for their practical implementation.

- **Chapter 5:** Bound states in the continuum in circular clusters of scatterers. We propose a third structure, in which we look into the radiation continuum of the spectrum looking for a bounded solution with infinite lifetime. This condition is found for circular arrays of resonators. Equations are derived, showing the limitations of our approach, and numerical simulations are presented, proving their suitability for experimental implementation.

- **Chapter 6:** Acoustic BIC in a circular cluster of resonators. This chapter retakes the main configuration of the previous chapter, and applies the same concept in a slightly different theoretical framework. Airborne acoustics and mode-matching theory are used in order to prove the existence of a BIC in our system. Theory, simulations and experimental results are presented, stating that our model is valid and it can be used for creating robust BICs which can be directly measured.

- **Chapter 7** Conclusion. Finally, this thesis provides a concise summary and discussion of the main findings, along with potential directions for future research.

Chapter 2

Multiple Scattering Theory for flexural waves in thin elastic plates

2.1 Elastic waves

A solid body becomes deformed when subjected to external forces. The origin of the forces causing the deformation is not necessarily mechanical; it can be of thermal, electrical or magnetical nature. Nevertheless, thermoelastic effects are slower compared to the other types, and both electrostrictive coupling and magnetostrictive coupling provide nonlinear stresses proportional to the square of the electric and magnetic field, thus being insignificant for small fields. Therefore, when talking about elastic wave generation, it is commonly adopted a linear behaviour of the material (piezoelectric or piezomagnetic coupling).

The appropriate way to define the deformation of a solid is in terms of a displacement vector field: $\boldsymbol{u} = \boldsymbol{u}(\boldsymbol{r}, t)$. This vector relates the initial position of a point in the medium before the deformation, $\boldsymbol{r}$, with its position after the modification, $\boldsymbol{r}' = \boldsymbol{r}'(\boldsymbol{r}, t)$,

$$\boldsymbol{u} = \boldsymbol{r}' - \boldsymbol{r}. \tag{2.1}$$

The displacement of two neighbouring points in the medium (at spatial positions $\boldsymbol{x}$ and $\boldsymbol{x} + d\boldsymbol{x}$) is described as

$$\boldsymbol{u}(\boldsymbol{x}) = \boldsymbol{u}(\boldsymbol{x}), \tag{2.2}$$

$$\boldsymbol{u}(\boldsymbol{x} + d\boldsymbol{x}) = \boldsymbol{u}(\boldsymbol{x}) + \sum_{j=1}^{3} \frac{\partial \boldsymbol{u}}{\partial x_j} dx_j = \boldsymbol{u}(\boldsymbol{x}) + d\boldsymbol{u}. \tag{2.3}$$

The medium is considered as deformed only if different material points are displaced relative to each other; in other words, if the gradient of displacements $\partial \boldsymbol{u}/\partial x_j$ is non-zero. Nonetheless, the gradient

of displacements is not a suitable magnitude for expressing deformation of a solid, considering that it is non-zero in cases where no deformation occurs, for instance simple overall rotation of the solid. The gradient tensor resulting in the case of overall rotation is antisymmetric. Thus, the antisymmetric part of the gradient must be excluded from the definition of any magnitude representing deformation. The strain tensor, characterizing deformation of the solid, is expressed as

$$\varepsilon_{ij} = \frac{1}{2}\left(\frac{\partial u_i}{\partial x_j} + \frac{\partial u_j}{\partial x_i}\right). \tag{2.4}$$

This term is included naturally after the exclusion of the antisymmetric part of the gradient tensor (which we will call $\Omega_{ij} = \frac{1}{2}\left(\frac{\partial u_i}{\partial x_j} - \frac{\partial u_j}{\partial x_i}\right)$) in the expression of the line element. Line elements $|d\boldsymbol{r}|$ and $|d\boldsymbol{r}'|$ are the difference in position between the two points of the solid before and after the deformation. They can be related to the displacement vector in the following way:

$$|d\boldsymbol{r}'|^2 = |d\boldsymbol{r} + d\boldsymbol{u}|^2 = \sum_{k=1}^{3} \left(dx_k dx_k + du_k du_k + 2du_k dx_k\right). \tag{2.5}$$

Since, by applying the chain rule

$$du_k = \sum_{m=1}^{3} \frac{\partial u_k}{\partial x_m} dx_m, \tag{2.6}$$

the line element will be

$$|d\boldsymbol{r}'|^2 = |d\boldsymbol{r}|^2 + \sum_{k,l,m=1}^{3} \frac{\partial u_k}{\partial x_m}\frac{\partial u_k}{\partial x_l} dx_l dx_m + 2\sum_{k,m=1}^{3} \frac{\partial u_k}{\partial x_m} dx_m dx_k. \tag{2.7}$$

In this equation, the term containing the partial derivatives $\partial_l u_k \partial_m u_k$ can be neglected under the assumption of a linear approximation. Both k and m are dummy indices, which allows us to finally express the line element as

$$|d\boldsymbol{r}'|^2 = |d\boldsymbol{r}|^2 + \sum_{m,k}\left(\frac{\partial u_k}{\partial x_m} + \frac{\partial u_m}{\partial x_k}\right) dx_m dx_k = |d\boldsymbol{r}|^2 + 2\sum_{m,k} \varepsilon_{km} dx_m dx_k. \tag{2.8}$$

The strain tensor ε_{mk} relates the deformation of the line element of some elastic medium with the displacement vector $\boldsymbol{u}$. This strain or deformation appears in a solid as a consequence of some external (or internal) force field $\boldsymbol{F}$ defined through the Cauchy stress second order tensor $\boldsymbol{\sigma}$ by means of

$$F_i = \int_S \sum_{k=1}^{3} \boldsymbol{\sigma}_{ik} dS_k = \int_V \sum_{k=1}^{3} \frac{\partial \boldsymbol{\sigma}_{ik}}{\partial x_k} dV, \tag{2.9}$$

where the stress tensor and the movement of the solid are related each other through Newton's second law

$$\rho a_i = \sum_k \frac{\partial \boldsymbol{\sigma}_{ik}}{\partial x_k}, \tag{2.10}$$

being ρ the density of the medium and the acceleration vector $\boldsymbol{a}$,

$$\boldsymbol{a} = \frac{d\boldsymbol{v}}{dt} = \frac{\partial \boldsymbol{v}}{\partial t} + \sum_{k=1}^{3} \frac{\partial \boldsymbol{v}}{\partial x_k} v_k. \tag{2.11}$$

The convective term $v_k \partial_k \boldsymbol{v}$ will be neglected here, as it is a non linear term and we are supposing linear approximation, while the time derivative can be related with the displacement vector

$$\frac{\partial \boldsymbol{v}}{\partial t} = \frac{\partial}{\partial t}\frac{\partial \boldsymbol{x}}{\partial t} = \frac{\partial^2 \boldsymbol{u}}{\partial t^2}. \tag{2.12}$$

Thus, Newton's second law is rewritten as

$$\rho \frac{\partial^2 u_i}{\partial t^2} = \sum_{k=1}^{3} \frac{\partial \boldsymbol{\sigma}_{ik}}{\partial x_k}. \tag{2.13}$$

The stress tensor will be assumed to be some function of the strain. This function should be expressed in a Taylor series, being the zero order term null (there is no stress if there is no strain) and neglecting the orders higher than one because of the linear assumption, then the more general form for this function is

$$\sigma_{ik} = \sum_{lm} C_{iklm} \varepsilon_{lm}. \tag{2.14}$$

In the case of the works that will be presented in the following chapters, a linear Hooke's law in an isotropic material has been adopted as the relationship between stress and strain tensors. Therefore, the fourth order stiffness tensor C_{iklm} is highly simplified to

$$\left(c_{ij}\right) = \begin{pmatrix} c_{11} & c_{12} & c_{12} & 0 & 0 & 0 \\ c_{12} & c_{11} & c_{12} & 0 & 0 & 0 \\ c_{12} & c_{12} & c_{11} & 0 & 0 & 0 \\ 0 & 0 & 0 & c_{66} & 0 & 0 \\ 0 & 0 & 0 & 0 & c_{66} & 0 \\ 0 & 0 & 0 & 0 & 0 & c_{66} \end{pmatrix}, \tag{2.15}$$

with $c_{66} = (c_{11} - c_{12})/2$. Here, matrix notation (Voigt notation) of elastic coefficients has been used, instead of tensor notation. For more information about this notation, please refer to [24]. In terms of Young's elastic modulus and Poisson's ratio ($E = c_{11} - 2c_{12}^2/(c_{11} + c_{12})$ and $\nu = c_{12}/(c_{11} + c_{12})$), the stresses can be written as

$$\sigma_{ij} = \frac{E\nu}{(1+\nu)(1-2\nu)} S\delta_{ij} + \frac{E}{(1+\nu)} S_{ij}, \tag{2.16}$$

where $S = S_{11} + S_{22} + S_{33}$ is the dilatation of the solid. Depending on the geometry of the domain of study, these expressions will be simplified.

2.2 Love-Kirchhoff plate theory

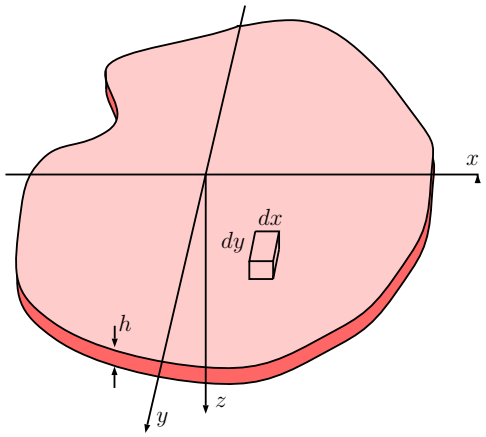

Figure 2.1: Thin elastic plate with differential element.

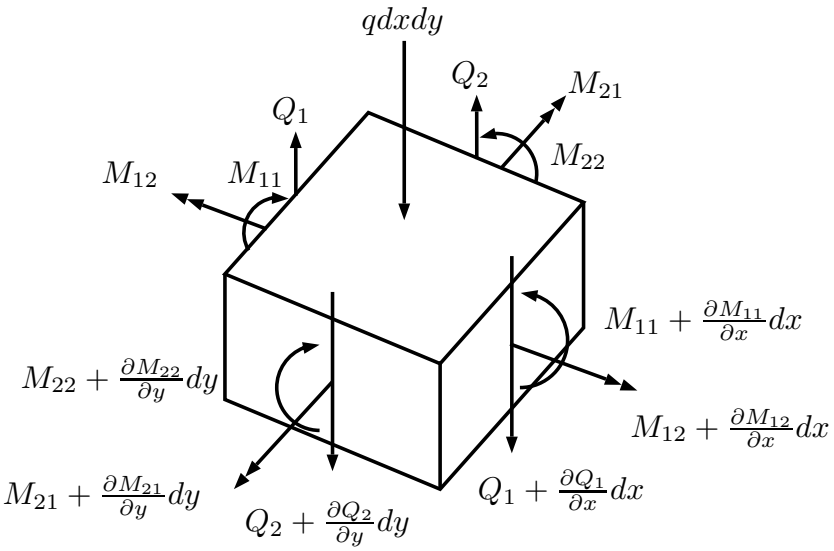

Figure 2.2: Differential element of a plate subjected to forces and moments.

In the following, we will focus on the solution of the elastic field for thin elastic films under bending moments. Although various kinds of waves can propagate through a plate, bending (or flexural) waves are well-known and have been largely studied due to their structure-fluid interaction. Bending waves produce displacements in a direction transverse to the direction of propagation, interacting with the properties of any adjacent fluid. The theory involving thin plates is the same as that of Bernoulli-Euler beams.

Consider a plate of thickness h and of infinite extent having its undeflected surface in the x, y-plane, such as in Fig. 2.1. Take a differential element $h\,dx\,dy$ of the plate and consider the moments and forces acting on the differential element as in Fig. 2.2. The bending moments per unit length M_{11}, M_{22} arise

from distributions of normal stresses σ_{11}, σ_{22}, while the twisting moments per unit length M_{12}, M_{21} arise from shearing stresses σ_{12}, σ_{21}. The shear forces per unit length Q_1, Q_2 arise from shearing stresses σ_{13}, σ_{23}. There are three force equations of motion to be applied, but only that in the z direction is non-trivial (the z axis is the only direction with free boundary conditions, the plate is infinite in both x and y directions). The equations of motion give

$$-Q_1 dy + \left(Q_1 + \frac{\partial Q_1}{\partial 1} dx\right) dy - Q_2 dx + \left(Q_2 + \frac{\partial Q_2}{\partial y} dy\right) dx + q dx dy = \rho h dx dy \frac{\partial^2 w}{\partial t^2}, \tag{2.17}$$

$$\left(M_{22} + \frac{\partial M_{22}}{\partial y} dy\right) dx - M_{22} dx + M_{12} dy - \left(M_{12} + \frac{\partial M_{12}}{\partial x} dx\right) dy - Q_2 dx dy = 0, \tag{2.18}$$

$$\left(M_{11} + \frac{\partial M_{11}}{\partial x} dx\right) dy - M_{11} dy + \left(M_{21} + \frac{\partial M_{21}}{\partial y} dy\right) dx - M_{21} dx - Q_1 dy dx = 0, \tag{2.19}$$

where q is the external loading, and the displacement $w(x, y, t)$ measures the deflection of the middle plane of the plate. Rotary-inertia effects have been neglected in the moment equations. Higher-order contributions to the moments from the loading q have also been neglected in these equations. After cancelling terms, these equations are reduced to

$$\frac{\partial Q_1}{\partial x} + \frac{\partial Q_2}{\partial y} + q = \rho h \frac{\partial^2 w}{\partial t^2}, \tag{2.20}$$

$$\frac{\partial M_{22}}{\partial y} - \frac{\partial M_{12}}{\partial x} - Q_2 = 0, \tag{2.21}$$

$$\frac{\partial M_{11}}{\partial x} + \frac{\partial M_{21}}{\partial y} - Q_1 = 0. \tag{2.22}$$

Solving the last two equations for Q_1, Q_2 and substituting them in the first equation gives a single equation in terms of the various moments,

$$\frac{\partial^2 M_{11}}{\partial x^2} + \frac{\partial^2 M_{21}}{\partial x \partial y} - \frac{\partial^2 M_{21}}{\partial y \partial x} + \frac{\partial^2 M_{22}}{\partial x^2} + q = \rho h \frac{\partial^2 w}{\partial t^2}. \tag{2.23}$$

The relation between moments and deflection must be established. A typical lamina (abcd) of a differential element of plate is shown in Fig. 2.3. The lamina is located at a distance z below the mid plane of the plate. When the element is subjected to pure bending, it is assumed to deform as shown in Fig. 2.4. It is assumed that plane sections remain plane and perpendicular to the mid plane. A similar behaviour also holds in the y, z-plane. It follows that the normal strains in the lamina are given by

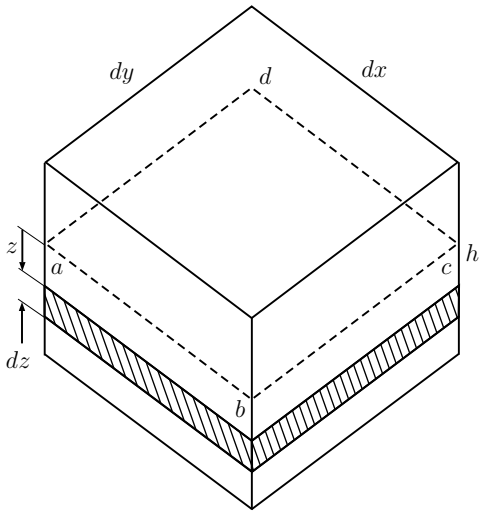

Figure 2.3: Differential element of plate with a lamina $abcd$ shown shaded.

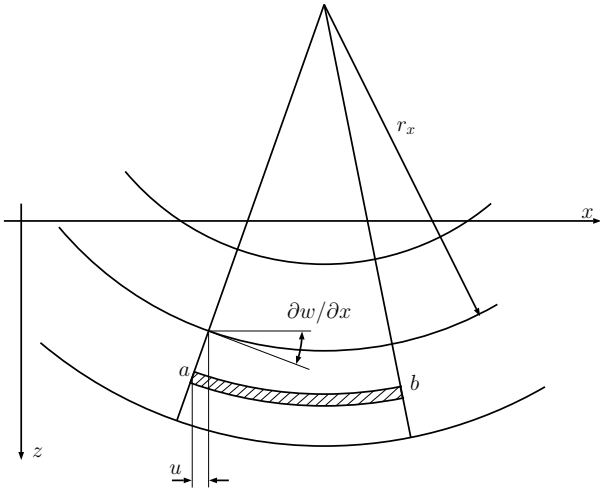

Figure 2.4: Deformation of the differential element in the xz plane. The lamina $abcd$ appears shaded.

$$\varepsilon_{11} = \frac{z}{r_x}, \tag{2.24}$$

$$\varepsilon_{22} = \frac{z}{r_y}, \tag{2.25}$$

where r_x, r_y are the radii of curvature in the x, z- and y, z-planes. If small deflections and slopes are assumed, the curvatures may be approximated by $-\partial^2 w/\partial x^2$, $-\partial^2 w/\partial y^2$,

$$\varepsilon_{11} = -z\frac{\partial^2 w}{\partial x^2}, \tag{2.26}$$

$$\varepsilon_{22} = -z\frac{\partial^2 w}{\partial y^2}. \tag{2.27}$$

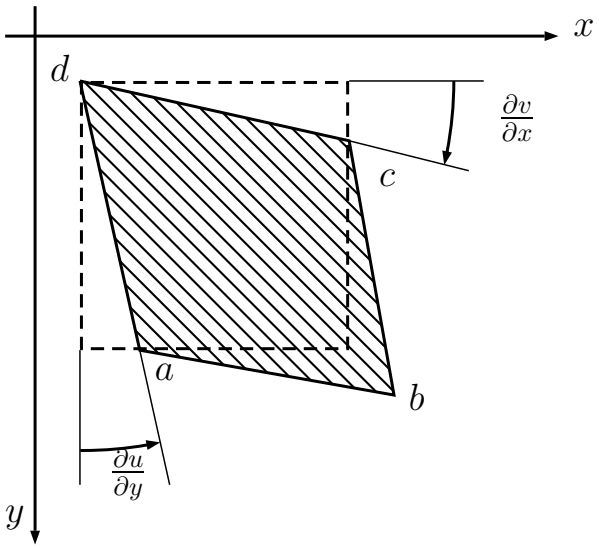

Figure 2.5: Shear deformation of the differential element in the xy plane. The lamina $abcd$ is shown shaded.

The lamina is shown in Fig. 2.5 in a sheared configuration (extensional strains are not shown in this representation). The rotations of the sides are given by $\partial u_x/\partial y$ and $\partial u_y/\partial x$. The shear strain in the lamina is given by

$$\varepsilon_{xy} = \frac{\partial u_x}{\partial y} + \frac{\partial u_y}{\partial x}. \tag{2.28}$$

Displacement component u_x is given by $u_x = -z\partial w/\partial x$. Similarly, $u_y = -z\partial w/\partial y$, so that

$$\varepsilon_{12} = -2z\frac{\partial^2 w}{\partial x \partial y}. \tag{2.29}$$

$$\varepsilon_{12} = \frac{1}{2}\left(\frac{\partial u_x}{\partial y} + \frac{\partial u_y}{\partial x}\right) = -z\frac{\partial^2 w}{\partial x \partial y}. \tag{2.30}$$

Recalling Hooke's Law in equation (2.16), now the relationship between stress and strain can be developed under the assumption of plane stress; the thin plate is infinite in both x and y directions, while it has two free boundaries in the z axis. Therefore, $\sigma_{31} = \sigma_{13} = \sigma_{32} = \sigma_{23} = \sigma_{33} = 0$. Taking equation (2.16) for σ_{33} will give us S_{33} as a function of S_{11} and S_{22}, and then, introducing this expression in equation (2.16) for σ_{11} and σ_{22},

$$\sigma_{11} = \frac{E}{1-\nu^2}\left(S_{11} + \nu S_{22}\right) = -\frac{Ez}{1-\nu^2}\left(\frac{\partial^2 w}{\partial x^2} + \nu\frac{\partial^2 w}{\partial y^2}\right). \tag{2.31}$$

$$\sigma_{22} = \frac{E}{1-\nu^2}\left(S_{22} + \nu S_{11}\right) = -\frac{Ez}{1-\nu^2}\left(\frac{\partial^2 w}{\partial y^2} + \nu\frac{\partial^2 w}{\partial x^2}\right), \tag{2.32}$$

$$\sigma_{12} = G\varepsilon_{12} = -2Gz\frac{\partial^2 w}{\partial x \partial y}, \tag{2.33}$$

where G is the shear modulus, related to Young's modulus E by $G = E/2\left(1+\nu\right)$. Consider the face of the element defined by $h\ dy$. The bending moment on that face due to σ_{11} will be

$$M_{11} = \int_{-h/2}^{h/2} z\sigma_{11} dz = -D\left(\frac{\partial^2 w}{\partial x^2} + \nu\frac{\partial^2 w}{\partial y^2}\right), \tag{2.34}$$

where

$$D = \frac{Eh^3}{12\left(1-\nu^2\right)} \tag{2.35}$$

is the plate's stiffness. Similarly,

$$M_{22} = -D\left(\frac{\partial^2 w}{\partial y^2} + \nu\frac{\partial^2 w}{\partial x^2}\right). \tag{2.36}$$

For M_{12}, the integral is

$$M_{12} = -\int_{-h/2}^{h/2} z\sigma_{12} dz. \tag{2.37}$$

Moreover, we have that $M_{12} = -M_{21}$. Substituting all these expressions in equation (2.23), we obtain

$$D\left(\frac{\partial^4 w}{\partial x^4} + 2\frac{\partial^4 w}{\partial x^2 \partial y^2} + \frac{\partial^4 w}{\partial y^4}\right) - q = -\rho h\frac{\partial^2 w}{\partial t^2}. \tag{2.38}$$

The expression in parenthesis may be written as

$$\frac{\partial^4 w}{\partial x^4} + 2\frac{\partial^4 w}{\partial x^2 \partial y^2} + \frac{\partial^4 w}{\partial y^4} = \left(\frac{\partial^2}{\partial x^2} + \frac{\partial^2}{\partial y^2}\right)\left(\frac{\partial^2 w}{\partial x^2} + \frac{\partial^2 w}{\partial y^2}\right) = \nabla^2\nabla^2 w. \tag{2.39}$$

The Laplacian of the Laplacian is designated as the biharmonic operator ∇^4. The governing equation is then

$$D\nabla^4 w(\boldsymbol{r}, t) + \rho h\frac{\partial^2 w(\boldsymbol{r}, t)}{\partial t^2} = q(\boldsymbol{r}, t). \tag{2.40}$$

Consider now that we are in an harmonic regime and the propagation occurs only in a direction contained in the x,y-plane, that is to say, $w(\boldsymbol{r},t) = w(\boldsymbol{r})e^{-i(\omega t - k_x x - k_y y)}$. In the absence of external forces ($q = 0$),

$$\left(\nabla^4 - k_b^4\right) w(\boldsymbol{r}) = 0, \tag{2.41}$$

where $k_b^2 = k_x^2 + k_y^2$, or $\boldsymbol{k}_b = \boldsymbol{k}_x + \boldsymbol{k}_y$ and $k_b = \left(\omega^2 \rho h/D\right)^{1/4}$ is the dispersion relation of the flexural waves in the plate.

2.3 Multiple Scattering Theory

A general definition for multiple scattering could be "the interaction of fields with two or more obstacles" [25]. Classical examples of these problems in classic physics are the scattering of sound waves by two rigid spheres or the scattering of spherical electron waves by a cluster of atoms in condensed-matter physics.

These kind of problems can be stated as a set of N disjoint obstacles, $B_i, i = 1, 2, ..., N$ with boundary S_i where a given incident wave illuminates the cluster of objects and the problem is to calculate the scattered waves. Everything about the obstacles is known (location, shape, orientation and boundary condition) and if the objects are penetrable, the internal composition is also known. Mathematically, the deterministic multiple-scattering problem is easily posed; it is an exterior boundary-value problem where the boundary is not simply-connected and with a radiation condition at infinity. Despite this, the problem is usually hard, as long as the geometry of the obstacles is not trivial.

When it comes to simple boundary objects, such as points, circles or spheres, MST proves to be a very efficient method from the numerical point of view. It has been widely applied to electromagnetic and mechanical waves, offering a complementary tool for numerical methods. Analytical methods are still a reliable tool for science, allowing a better understanding of the physics underneath the system.

Let us assume that some incident field ψ_0, e.g. a plane wave, arrives to a region of the space where there is an object which scatters waves. The total field ψ_T in space now will be

$$\psi_T = \psi_0 + \psi_{SC}, \tag{2.42}$$

where ψ_{SC} is the scattered field by the object. This scattered field depends on the incident field via an operator (which we will call T matrix). Thus, we can write

$$\psi_{SC} = T\psi_0, \tag{2.43}$$

and the total field is therefore given by

$$\psi_T = (1 + T)\,\psi_0. \tag{2.44}$$

Now, let us assume that we have instead a cluster of N objects located in positions $\boldsymbol{R}_\alpha$, for $\alpha = 1, 2, ..., N$. Each object scatters a field ψ^α_{SC}, thus

$$\psi_T = \psi_0 + \sum_{\alpha=1}^{N} \psi^\alpha_{SC}. \tag{2.45}$$

We know the T matrix of each scatterer, labelled T_α, however it relates the response of the scatterer to its incident field, and now this incident field is not only ψ_0, but the incident field ψ_0 plus the scattered field by all the other scatterers $\beta \neq \alpha$. Then we can write

$$\psi^\alpha_{SC} = T_\alpha \psi_{0\alpha} = T_\alpha \left(\psi_0 + \sum_{\beta \neq \alpha} \psi^\beta_{SC} \right), \tag{2.46}$$

which is equivalent to

$$\psi^\alpha_{SC} - T_\alpha \sum_{\beta \neq \alpha} \psi^\beta_{SC} = T_\alpha \psi_0. \tag{2.47}$$

The above equation, which is often called the *Foldy-Lax self-consistent method*, is actually a set of N equations from which we can obtain the N unknowns ψ^α_{SC}.

In the case of this thesis, as previously developed in Section (2.2), the equation of motion describing the movement of a plate was stated in equation 2.41. For a scattering problem, the incident field is expressed as

$$w_0(\boldsymbol{r}) = \sum_{q=-\infty}^{+\infty} \left[A^J_q J_q(k_b r) + A^I_q I_q(k_b r) \right] e^{iq\theta}, \tag{2.48}$$

where $J_q(k_b r)$ is the q-order Bessel function of the first kind, and $I_q(k_b r)$ is the q-order modified Bessel function of the first kind. The scattered field, however, is given by

$$w_{sc}(\boldsymbol{r}) = \sum_{q=-\infty}^{+\infty} \left[B^H_q H_q(k_b r) + B^K_q K_q(k_b r) \right] e^{iq\theta}, \tag{2.49}$$

where $H_q(k_b r)$ is the q-order Hankel function of the first kind (or Bessel function of the third kind). All along this work, we will work with the first definition of the Hankel function:

$$H^{(1)}_q(k_b r) = J_q(k_b r) + iY_q(k_b r), \tag{2.50}$$

where $Y_q(k_b r)$ is the q-order Bessel function of the second kind. Finally, $K_q(k_b r)$ is the q-order modified Bessel function of the second kind. The choice of the wave functions is dictated by the conditions that the scattered response is finite at $r = 0$ and must be outgoing, or radiating, as $r \to \infty$ [26].

2.4 Sources (Excitation fields)

Two main types of incident fields will be treated in the following chapters; the plane wave and the point source. The response given by the systems under more complicated sources can be understood by means of these two basic fields. In this work, we are interested in representing the field as an expansion in terms of Bessel functions, so as to introduce later the MST that will help us compute the scattering field of a collection of resonators under some incident wave.

2.4.1 The plane wave

A plane wave is a field distribution that propagates in a two-dimensional space with some direction given by the wavenumber $\boldsymbol{k} = k_x\hat{\boldsymbol{x}} + k_y\hat{\boldsymbol{y}} = k(\cos\theta_0, \sin\theta_0)$ and a complex amplitude C_0

$$w_0(\boldsymbol{r}) = C_0 e^{i\boldsymbol{k}\cdot\boldsymbol{r}}, \tag{2.51}$$

where the subscript indicates that it is an incident field. The scalar product can be expressed as $\boldsymbol{k}\cdot\boldsymbol{r} = kr\cos(\theta)$, where θ is the angle between the wavenumber and the position vector. Then, it is clear that equation (2.51) is periodic, and can therefore be expanded as a Fourier series

$$e^{i\boldsymbol{k}\cdot\boldsymbol{r}} = \sum_{q=-\infty}^{\infty} c_q(kr)e^{in\theta}. \tag{2.52}$$

The expression of the Fourier coefficients is

$$c_q(kr) = \frac{1}{2\pi}\int_0^{2\pi} e^{ikr\cos(\theta)}e^{-iq\theta}d\theta, \tag{2.53}$$

which is closely related to the integral definition of the Bessel function [27]. Thus, the incident field can be expressed as

$$w_0(\boldsymbol{r}) = C_0\sum_{q=-\infty}^{\infty} i^q e^{-iq\theta_0}J_q(kr)e^{iq\theta} = \sum_{q=-\infty}^{\infty} A_q^J J_q(kr)e^{iq\theta}, \tag{2.54}$$

where the incident coefficients are defined $A_q^J = C_0 i^q e^{-iq\theta}$. Comparing this result with the generic expression of an incident field in equation (2.48), it can be seen that for an incident plane wave, $A_q^I = 0$.

Before moving on the second kind of incident field, let us express this same field in another reference frame $\boldsymbol{r}'$, such that

$$\boldsymbol{r}' = \boldsymbol{r} - \boldsymbol{R}'. \tag{2.55}$$

In order to transform the Bessel function summation from one reference frame to the other one, Graf's addition theorem [27] must be used. However, in the case of a simple plane wave, the transformation can be done directly over equation 2.51.

$$w_0(\boldsymbol{r}) = C_0 e^{i\boldsymbol{k}\cdot\boldsymbol{r}} = C_0 e^{i\boldsymbol{k}\cdot\boldsymbol{R}'} e^{i\boldsymbol{k}\cdot\boldsymbol{r}} = C_0 e^{i\boldsymbol{k}\cdot\boldsymbol{R}'} \sum_{q=-\infty}^{\infty} i^q e^{-iq\theta_0} J_q(kr') e^{iq\theta'}, \tag{2.56}$$

then,

$$A_q'^J = C_0 e^{i\boldsymbol{k}\cdot\boldsymbol{R}'} i^q e^{-iq\theta_0} = e^{i\boldsymbol{k}\cdot\boldsymbol{R}'} A_q^J. \tag{2.57}$$

2.4.2 The point source

The point source is the same as the Green function of the system. Henceforth, the following equation must be solved:

$$\Delta^2 G(\boldsymbol{r}) - k_b^4 G(\boldsymbol{r}) = \delta(\boldsymbol{r}). \tag{2.58}$$

The solution we are looking for represents outgoing waves as $r \to \infty$. First of all, applying a two-dimensional Fourier transform,

$$G(\boldsymbol{k}) = \int\int G(\boldsymbol{r}) e^{-\boldsymbol{k}\cdot\boldsymbol{r}} d\boldsymbol{r}, \tag{2.59}$$

where the integral is over the whole plate's plane. Then,

$$\zeta(k) = k^4 - k_b^4, \tag{2.60}$$

being $k = |\boldsymbol{k}|$. This ζ function is the operator applied in the Fourier space. It has four zeros, $k = \pm k_b$ and $k = \pm i k_b$; during integration, these zeros must be handled properly. In Fourier space, $G(\boldsymbol{k}) = 1/\zeta(k)$; therefore, we can now define the green function in the real space as the inverse Fourier transform,

$$G(\boldsymbol{r}) = \frac{1}{(2\pi)^2} \int\int \frac{e^{i\boldsymbol{k}\cdot\boldsymbol{r}}}{\zeta(f)} d\boldsymbol{k}. \tag{2.61}$$

By changing into polar coordinates, $\boldsymbol{r} = r(\cos\theta, \sin\theta)$ and $\boldsymbol{k} = k(\cos\beta, \sin\beta)$, the integration over β can be easily solved by expanding

$$e^{i\boldsymbol{k}\cdot\boldsymbol{r}} = \sum_{n=-\infty}^{\infty} i^n J_n(kr) e^{in(\theta-\beta)}, \tag{2.62}$$

obtaining

$$G(\boldsymbol{r}) = \frac{1}{2\pi} \int_0^{\infty} \frac{J_0(kr)}{k^4 - k_b^4} k dk. \tag{2.63}$$

From the four zeros we have defined before, the only ones involved in this integral is the one at $k = k_b$. Thus, we must define a contour below the singularity so that the radiation condition is satisfied. Following [28], the integral might be split into two, using

$$2J_0(kr) = H_0^{(1)}(kr) + H_0^{(2)}(kr). \tag{2.64}$$

The Green function is then split into

$$G(\boldsymbol{r}) = \frac{1}{4\pi}(G^{(1)}(\boldsymbol{r}) + G^{(2)}(\boldsymbol{r})), \tag{2.65}$$

with

$$G^{(n)}(\boldsymbol{r}) = \int_0^\infty \frac{H_0^{(n)}(kr)}{k^4 - k_b^4} k dk, \; n = 1, 2. \tag{2.66}$$

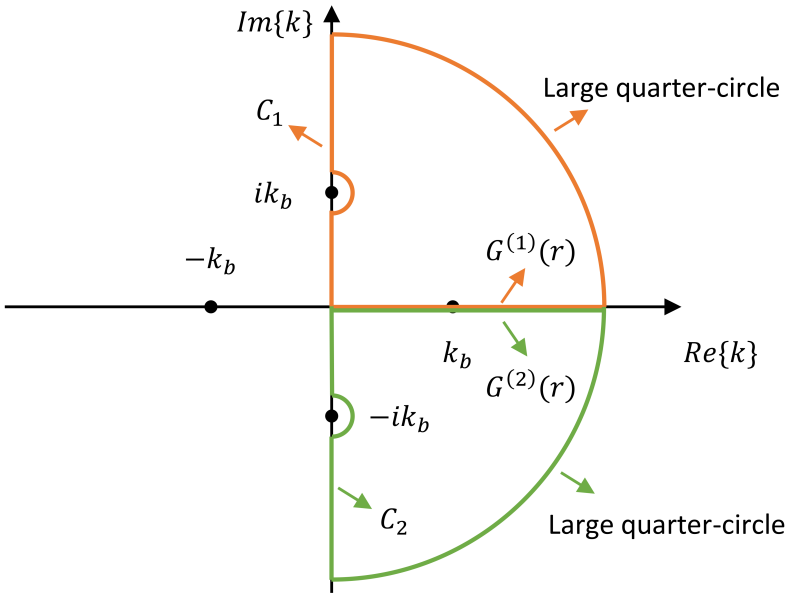

Figure 2.6: Contour path for solving the two integrals in the complex frequency plane.

To evaluate the first integral ($G^{(1)}(\boldsymbol{r})$), the contour chosen is defined in Fig. 2.6 by the orange line; it is formed by the positive real axis, a large quarter-circle in the first quadrant of the complex k-plane and the positive imaginary line, with an indented part to the right of the pole at $k = ik_b$ (C_1). The quarter-circle does not contribute to the integral, due to the vanishing behavior of $H_0^{(1)}$ for large-arguments. The pole at $k = k_b$ makes a residue contribution of

$$2\pi i \frac{1}{4k_b^2} H_0^{(1)}(kr). \tag{2.67}$$

Thus,

$$G^{(1)}(r) + \int_{C_1} \frac{H_0^{(1)}(kr)}{k^4 - k_b^4} k dk = \frac{\pi i}{2k_b^2} H_0^{(1)}(kr). \tag{2.68}$$

Concerning the integral term over C_1, the contribution from the pole $k = ik_b$ is

$$-\pi i \frac{ik_b}{4(ik_b)^3} H_0^{(1)}(ikr) = \frac{1}{2k_b^2} K_0(k_b r). \tag{2.69}$$

The straight parts of C_1 give a principal-value integral; if we put $k = i\alpha$ on that piece of the contour, we see that

$$\int_{C_1} = \frac{1}{2k_b^2} K_0(k_b r) + \int_{\infty}^{0} \frac{H_0^{(1)}(i\alpha r)}{\alpha^4 - k_b^4} (id\alpha) \tag{2.70}$$

$$= \frac{1}{2k_b^2} K_0(k_b r) + \frac{2}{\pi i} \int_0^{\infty} \frac{K_0(\alpha r)}{\alpha^4 - k_b^4} \alpha d\alpha, \tag{2.71}$$

then,

$$G^{(1)}(r) = \frac{\pi i}{2k_b^2} H_0^{(1)}(kr) - \frac{1}{2k_b^2} K_0(kr) - \frac{2}{\pi i} \int_0^{\infty} \frac{K_0(\alpha r)}{\alpha^4 - k_b^4} \alpha d\alpha. \tag{2.72}$$

$G^{(2)}(r)$ can be solved in a similar way. We define the contour of integration as the one depicted in Fig. 2.6 by the green line; the positive real axis is the one that will give us the Green function. We close the path by adding a large quarter-circle in the fourth quadrant of the k-plane and the negative imaginary line, where we have indented again around the pole $k = -ik_b$ (C_2). The large-argument behavior of $H_0^{(2)}$ ensures that the quarter-circle does not contribute to the integral, as happened in $G^{(1)}(r)$. In this second situation, there are no poles inside the contour. Thus,

$$G^{(2)}(r) + \int_{C_2} \frac{H_0^{(2)}(kr)}{k^4 - k_b^4} k dk = 0, \tag{2.73}$$

The pole at $k = -ik_b$ contributes

$$\pi i \frac{-ik_b}{4(-ik_b)^3} H_0^{(2)}(-ik_b r) = \frac{1}{2k_b^2} K_0(k_b r). \tag{2.74}$$

The straight parts of C_2 give a principal-value integral; if we put $k = -i\alpha$ on that piece of the contour, we see that

$$\int_{C_2} = \frac{1}{2k_b^2} K_0(k_b r) + \int_{\infty}^{0} \frac{H_0^{(2)}(-i\alpha r)}{\alpha^4 - k_b^4} (-i\alpha)(-id\alpha) \tag{2.75}$$

$$= \frac{1}{2k_b^2} K_0(k_b r) - \frac{2}{\pi i} \int_0^{\infty} \frac{K_0(k_b r)}{\alpha^4 - k_b^4} \alpha d\alpha, \tag{2.76}$$

which gives

$$G^{(2)}(r) = -\frac{1}{2k_b^2}K_0(k_b r) + \frac{2}{\pi i}\int_0^\infty \frac{K_0(\alpha r)}{\alpha^4 - k_b^4}\alpha d\alpha. \tag{2.77}$$

Adding $G^{(1)}(r)$ and $G^{(2)}(r)$, the principal-value integrals cancel, leaving

$$G(\boldsymbol{r}) = \frac{i}{8k_b^2}\left(H_0^{(1)}(k_b r) + \frac{2i}{\pi}K_0(k_b r)\right), \tag{2.78}$$

which is equivalent to

$$G(\boldsymbol{r}) = \frac{i}{8k_b^2}\left(H_0^{(1)}(k_b r) - H_0^{(1)}(ik_b r)\right). \tag{2.79}$$

2.5 Scattering by a cluster of mass-spring resonators

In this section, the equation of motion in equation (2.40) is considered, where the external loading q is substituted by the distribution of point-like spring-mass resonators. This model has been chosen throughout this PhD thesis because it can approximate adequately the behavior of nanopillars attached to the plate, which is the immediate envisioned application for this work. As for inclusions from other materials, they will not only exhibit monopolar behavior as the point-like approximation does, but more multipoles must be also considered in the MST equations, as in [29]. Nevertheless, our approach has been proven useful for pillars and spheres on a plate [30] or embedded bolts [31–33]. These resonators are all equal and characterized with force constant k_α and mass m_α. There are N resonators located at positions $\boldsymbol{R}_\alpha$. The governing equation of motion for the plate's transverse displacement w is now written as

$$\left(D\nabla^4 - \omega^2\rho h\right)w(\boldsymbol{r}) = \sum_{\boldsymbol{R}_\alpha} f(\boldsymbol{R}_\alpha)\delta(\boldsymbol{r} - \boldsymbol{R}_\alpha), \tag{2.80}$$

where $f(\boldsymbol{R}_\alpha)$ is the force due to the presence of the spring-mass resonator [34]. This force is responsible for the movement of the mass attached to the plate. Then, applying Newton's second law in the resonator's position,

$$\omega^2 m_\alpha w_2(\boldsymbol{R}_\alpha) = f(\boldsymbol{R}_\alpha), \tag{2.81}$$

where $w_2(\boldsymbol{R}_\alpha)$ is the resonator's mass displacement. Moreover, Hook's law (in its one dimensional simplest form, not as in section (2.1)) is

$$f(\boldsymbol{R}_\alpha) = -k_\alpha\left[w(\boldsymbol{R}_\alpha) - w_2(\boldsymbol{R}_\alpha)\right]. \tag{2.82}$$

Using equations 2.81 and 2.82 into the motion equation 2.80, it becomes

$$\left(\nabla^4 - \omega^2 \frac{\rho h}{D}\right) w(\boldsymbol{r}) = \sum_{\boldsymbol{R}_\alpha} t_\alpha w(\boldsymbol{R}_\alpha)\delta(\boldsymbol{r} - \boldsymbol{R}_\alpha), \tag{2.83}$$

where t_α is the resonator's strength, which has been defined as

$$t_\alpha = \frac{m_\alpha}{D} \frac{\omega_\alpha^2 \omega^2}{\omega_\alpha^2 - \omega^2}, \tag{2.84}$$

and $\omega_\alpha = \sqrt{k_\alpha / m_\alpha}$ is the resonant frequency of the α resonator.

The multiple scattering problem is solved by building a system of self-consistent equations, so that the solution for the field $w(\boldsymbol{r})$ under some incident excitation $w_0(\boldsymbol{r})$ is given by

$$w(\boldsymbol{r}) = w_0(\boldsymbol{r}) + \sum_\alpha T_\alpha w_e(\boldsymbol{R}_\alpha) G_0(\boldsymbol{r} - \boldsymbol{R}_\alpha), \tag{2.85}$$

where $w_e(\boldsymbol{R}_\alpha)$ is the 'external' field: the incident field on the scatterer α; thus

$$w_e(\boldsymbol{R}_\alpha) = w_0(\boldsymbol{R}_\alpha) + \sum_{\beta \neq \alpha} T_\beta w_e(\boldsymbol{R}_\beta) G_0(\boldsymbol{R}_\alpha - \boldsymbol{R}_\beta). \tag{2.86}$$

The coefficients T_α can be obtained from the response of a single scatterer, in which $w_e(\boldsymbol{R}_\alpha) = w_0(\boldsymbol{R}_\alpha)$ and the field is

$$w(\boldsymbol{r}) = w_0(\boldsymbol{r}) + T_\alpha w_0(\boldsymbol{R}_\alpha) G_0(\boldsymbol{r} - \boldsymbol{R}_\alpha). \tag{2.87}$$

Inserting it into the left-hand side of the wave equation (2.83),

$$\left(\nabla^4 - k^4\right) \left[w_0(\boldsymbol{r}) + T_\alpha w_0(\boldsymbol{R}_\alpha) G_0(\boldsymbol{r} - \boldsymbol{R}_\alpha)\right] = T_\alpha w_0(\boldsymbol{R}_\alpha)\delta(\boldsymbol{r} - \boldsymbol{R}_\alpha), \tag{2.88}$$

and from the right-hand side,

$$t_\alpha w(\boldsymbol{R}_\alpha)\delta(\boldsymbol{r} - \boldsymbol{R}_\alpha) = t_\alpha \left[w_0(\boldsymbol{R}_\alpha) + T_\alpha w_0(\boldsymbol{R}_\alpha) G_0(\boldsymbol{0})\right] \delta(\boldsymbol{r} - \boldsymbol{R}_\alpha), \tag{2.89}$$

which allows then solving T_α as

$$T_\alpha = \frac{t_\alpha}{1 - i t_\alpha / (8k^2)}, \tag{2.90}$$

where $G_0(\boldsymbol{0}) = i/(8k^2)$. It is worth mentioning that, unlike multiple scattering methods for point scatterers for other kinds of waves, the Green's function for flexural waves in thin elastic plates given in equation (2.78) is not divergent at the origin; which means that no finite-size effect must be taken into account and the field infinitely close to the scatterer is solvable and non-divergent.

Finally, $w_e(\boldsymbol{R}_\alpha)$ coefficients can be found by solving the system of equations

$$\sum_{\beta=1}^{N} \left[\delta_{\alpha\beta} - (1-\delta_{\alpha\beta}) T_\beta G_0(\boldsymbol{R}_\alpha - \boldsymbol{R}_\beta)\right] w_e(\boldsymbol{R}_\beta) = w_0(\boldsymbol{R}_\alpha)$$

$$\sum_{\beta=1}^{N} M_{\alpha\beta} w_e(\boldsymbol{R}_\beta) = w_0(\boldsymbol{R}_\alpha). \tag{2.91}$$

Thus, the scattered field can be completely computed by inserting the solutions of the system into equation (2.86). The M matrix can be defined as in the previous equation, or, if the resonator's strength (t_α) is used instead of the T_α coefficients. If equation (2.90) is applied to equation (2.91),

$$\sum_{\beta=1}^{N} \left[\delta_{\alpha\beta} - (1-\delta_{\alpha\beta}) \frac{t_\beta}{1 - i t_\beta/(8k^2)} G_0(\boldsymbol{R}_\alpha - \boldsymbol{R}_\beta)\right] w_e(\boldsymbol{R}_\beta) = w_0(\boldsymbol{R}_\alpha), \tag{2.92}$$

rearranging some terms,

$$\sum_{\beta=1}^{N} \left[\delta_{\alpha\beta}(1 - i t_\beta/(8k^2)) - (1-\delta_{\alpha\beta}) t_\beta G_0(\boldsymbol{R}_\alpha - \boldsymbol{R}_\beta)\right] \frac{1}{1 - i t_\beta/(8k^2)} w_e(\boldsymbol{R}_\beta) = w_0(\boldsymbol{R}_\alpha). \tag{2.93}$$

Then, as $G_0(\mathbf{0}) = i/(8k^2)$,

$$\sum_{\beta=1}^{N} \left[\delta_{\alpha\beta} - t_\beta G_0(\boldsymbol{R}_\alpha - \boldsymbol{R}_\beta)\right] \frac{1}{1 - i t_\beta/(8k^2)} w_e(\boldsymbol{R}_\beta) = w_0(\boldsymbol{R}_\alpha). \tag{2.94}$$

Finally, applying again equation (2.90),

$$\sum_{\beta=1}^{N} \left[\delta_{\alpha\beta} t_\alpha^{-1} - G_0(\boldsymbol{R}_\alpha - \boldsymbol{R}_\beta)\right] T_\beta w_e(\boldsymbol{R}_\beta) = w_0(\boldsymbol{R}_\alpha). \tag{2.95}$$

If we redefine the scattering coefficients as $B_\beta = T_\beta w_e(\boldsymbol{R}_\beta)$, we end up with the following system,

$$\sum_{\beta=1}^{N} M_{\alpha\beta} B_\beta(\boldsymbol{R}_\beta) = w_0(\boldsymbol{R}_\alpha) \tag{2.96}$$

$$M_{\alpha\beta} = t_\alpha^{-1}\delta_{\alpha\beta} - G(R_{\alpha\beta}). \tag{2.97}$$

2.6 Eigenmodes and resonances of a finite cluster of resonators

In this section, a brief discussion on how to analyze the MST matrix and find the resonances of the system is done. Considering that we have an infinite thin plate in which we have arranged a finite set of point-like resonators, the motion equation that represents our system is equation (2.80), that can be rearranged as in equation (2.91). The later equation relates the incident field $w_0(\boldsymbol{R}_\alpha)$ and the scattering coefficients $w_e(\boldsymbol{R}_\beta)$. By definition, the eigenmodes of a system are the solution for this equation giving non-trivial solutions for the scattering coefficients when there is no incident field. In other words, we look for

$$\sum_{\beta=1}^{N} M_{\alpha\beta} w_e(\boldsymbol{R}_\beta) = 0, \;\; w_e(\boldsymbol{R}_\beta) \neq 0. \tag{2.98}$$

This condition implies the cancellation of the determinant of the MST matrix ($|M| = 0$). When dealing with finite amounts of resonators, the eigenmodes lie in the radiation part of the spectrum. Depending on the spatial and spectral properties of the eigenmodes, we will be able to distinguish between extended states, leaky resonances or BICs. The first type shows no confinement in the structure and the wave field propagates through the system. Leaky resonances are states whose energy is gathered at some reduced area, but there is some leakage of energy to the rest of the system. They present a complex frequency value. Finally, BICs are waves that remain localized even though they coexist with a continuous spectrum of radiating waves that can carry energy away [35]. They are characterized by an infinite lifetime (i.e., the imaginary frequency term is zero).

Therefore, we are looking for the cancellation of the M matrix in the complex frequency plane, which can be a computationally consuming problem in the case of big clusters. Nevertheless, we know that

$$|M| = 0 \rightarrow \prod_{i=1}^{N} \lambda_i = 0 \rightarrow \lambda_{min} = 0. \tag{2.99}$$

The smallest eigenvalue of the matrix is the responsible for the cancellation of the determinant. Thus, evaluating the behavior of this parameter we can evaluate the behavior of the whole matrix. Moreover, most of the eigenmodes will have complex frequencies; the real part of such a frequency corresponds to the peak expected upon excitation of the cluster. The imaginary part is inversely related with the quality factor of the resonance.

Finding the complex zeros of a determinant can be a difficult problem, as the determinant is usually complex-valued. An approximate value only using the real part of the frequency can be obtained. If the quality of the resonance is high, the imaginary frequency term will be close to zero, so that the complex frequency will be close to be purely real. Therefore, we can assume that the real frequency will not suffer from a big shift with respect to the real frequency obtained in the complex frequency plane.

The quality factor can also be estimated directly from the analysis in the real frequency line,

$$Q = \frac{f_0}{\Delta f}, \tag{2.100}$$

with f_0 being the resonant frequency and Δf the Full Width Half Maximum (FWHM).

Chapter 3

Dimerized localisation of waves in twisted bilayer crystal plates

3.1 Introduction

Twisted materials have received special attention from the scientific community in recent years due to their outstanding properties, specially twisted bilayer graphene. A twist between two layers of graphene (honeycomb lattice) has proven unprecedented electronic properties (flat bands [36], moiré effect [37], non-abelian gauge potentials [38] or superconductivity [21,22,39–44]), in such a way that a new research field called "twistronics" [45] is completely devoted to these structures. Analogs to twisted bilayers have been done for classical wave physics, finding new exotic behaviour in optics [46–53], phononics [54–58] and acoustics [59–63]. From the point of view of classical waves, these structures have shown strong localisation regimes with dependence on the rotation angle between the monolayers, making them suitable for wave control applications.

Depending on the twisting angle between both monolayers, the resulting structure might be periodic or aperiodic. Only for a set of discrete angles the bilayer will result in a periodic pattern, which we will call a commensurable phase [64]. Patterns formed when the twisted angle is not in a commensurate phase belong to the category of quasicrystals (they can be understood from the point of view of the cut and project method in [65]). Theoretical work concerning these structures has been done within the framework of periodic materials, by coupling the eigenmodes of the original lattices by means of an interaction term [37, 66, 67]. Even though, for most of the twisting angles, the resulting cluster is nonperiodic, and thus it cannot be analysed using Floquet-Bloch theory. In this sense, more work needs to be done in order to understand the dispersion relation of this kind of structures.

In this chapter, a comprehensive study on the localisation of waves in twisted bilayer crystals is done. Following a different approach to the one used in the analysis of quasicrystals [68], with resonant features found in three-dimensional structures [69], we are going to focus on the finite size features of the clusters. Multiple scattering between closer scatterers plays a major role in the localisation of eigenstates. Section 3.2 pays special attention to the commensurable phases and the formation of periodic structures in

twisted bilayer. Hence, a deeper analysis on the apparition of localized modes around these commensurate phases is done in section 3.3, as well as the apparition of a high density of localized modes for small rotation angles. Numerical examples using MST are given, using flexural waves for thin elastic plates with point-like resonators as the physical system, even if the conclusions in this chapter are valid for any kind of wave. Section 3.4 discusses on the role of the scatterers' strength, while 3.5 treats the effect of the anisotropy of the system. Finally, 3.6 focuses on analysing the quality factor of the dimerized resonances, while section 3.7 evaluates the robustness of these modes.

3.2 Commensurate phases in twisted bilayers

Let us assume that we have a cluster of scatterers divided into two sets, a and b, which positions are $\boldsymbol{R}_a = n_1\boldsymbol{a}_1 + n_2\boldsymbol{a}_2$ and $\boldsymbol{R}_b = m_1\boldsymbol{b}_1 + m_2\boldsymbol{b}_2$, with the vector lattice set $\boldsymbol{b}_1, \boldsymbol{b}_2$ being a rotated version of the set $\boldsymbol{a}_1, \boldsymbol{a}_2$. The angle θ_0 is defined as the rotation between both sets. For certain rotation angles, the two lattices are incommensurable, that is to say, $\boldsymbol{R}_a \neq \boldsymbol{R}_b$ for all the possible lattice points, i.e, periodicity is broken. On the other side, some special values of θ_0 can be found such that $\boldsymbol{R}_a = \boldsymbol{R}_b \equiv \boldsymbol{R}_p$ when $\boldsymbol{R}_p \neq 0$, so that periodicity is recovered. These commensurable phases are found for a given set of integers n_1, n_2, m_1, m_2.

Let us define the lattice vectors in the two-dimensional space as a complex vector, such that $a_\ell = a_{\ell x} + i a_{\ell y}$, for $\ell = 1, 2$, and similarly for $\boldsymbol{b}$. Under this representation, the rotation of set $\boldsymbol{b}$ is simply expressed by $\boldsymbol{b} = e^{i\theta_0}\boldsymbol{a}$. The condition for commensurability of the resulting lattice is given by

$$\theta_0 = i \ln\left[\frac{n_1 a_{1x} + n_2 a_{2x} + i(n_1 a_{1y} + n_2 a_{2y})}{m_1 a_{1x} + m_2 a_{2x} + i(m_1 a_{1y} + m_2 a_{2y})}\right] \in \mathcal{R}. \tag{3.1}$$

This equation is valid without lost of generality for every periodic lattice. In the case of a square lattice with a as lattice parameter, it gets reduced to

$$\theta_0 = i \ln\left[\frac{n_1 + i n_2}{m_1 + i m_2}\right] \in \mathcal{R}, \tag{3.2}$$

this condition implies that the number inside the natural logarithm must be a pure imaginary number,

$$n_1 m_1 + n_2 m_2 = 0. \tag{3.3}$$

In the case of a triangular lattice,

$$\theta_0 = i \ln\left[\frac{(n_1 - n_2) + i\sqrt{3}(n_1 + n_2)}{m_1 - m_2 + i\sqrt{3}(m_1 + m_2)}\right], \tag{3.4}$$

which can be simplified to

$$\frac{n_1}{n_2} = -\frac{2m_2 + m_1}{2m_1 + m_2}. \tag{3.5}$$

Honeycomb lattice shares its lattice vectors with triangular lattice; the latter has only one scatterer per unit cell, whereas honeycomb lattice has two scatterers per unit cell. Despite this, the existence of commensurability depends only on the relative rotation of the lattice vectors of each layer, and not on the structure of the unit cells [70]. Therefore, the commensurability condition is also shared for both lattices. It has been deeply analysed in [40], discussing Bravais lattice's symmetries, and also in [70] by finding the solutions for the diophantine equation. These studies show how the number of unknowns can be reduced to only two integer numbers (co prime numbers[1]):

$$\cos(\theta_0) = \frac{3m^2 + 3mr + r^2/2}{3m^2 + 3mr + r^2}, \tag{3.6}$$

where m and r are the coprime integers.

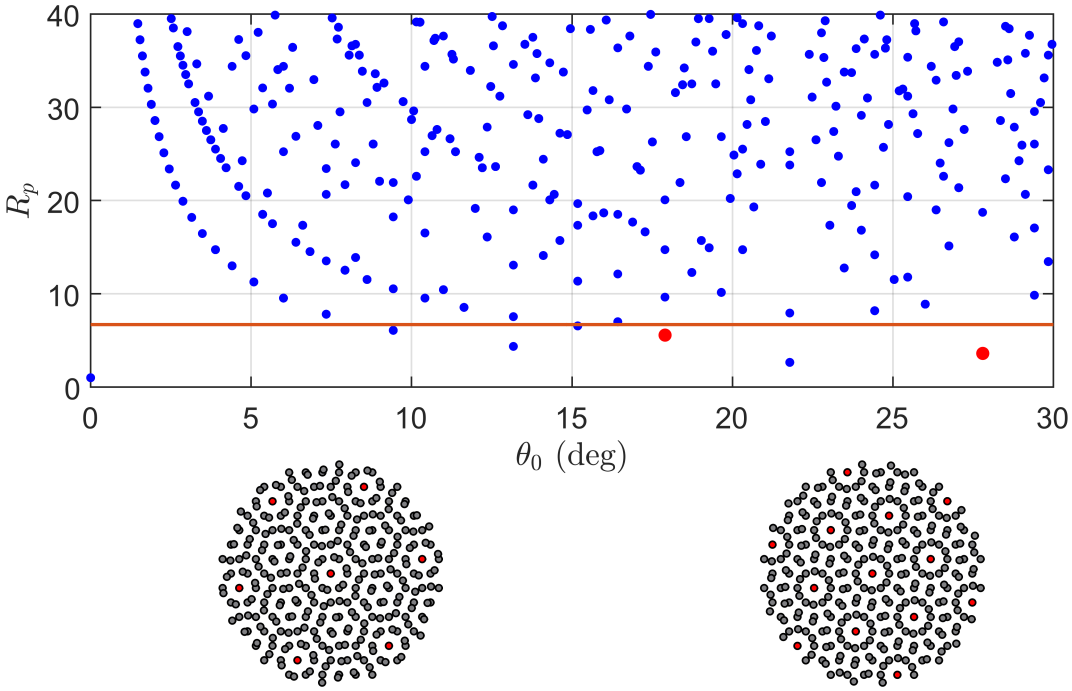

Figure 3.1: Commensurable phases for triangular lattice twisted bilayer. The upper panel shows the periodicity R_p and the rotation angle θ_0 at which the commensurability condition is fulfilled. Both clusters on bottom represent the system for the red points in the upper diagram. The radius of the cluster is $6.7a$, where a is the lattice parameter.

Figure (3.1) shows the commensurate phases of a twisted bilayer formed by twisting two triangular lattices. The upper panel is also valid for a twisted bilayer made of honeycomb lattices. Blue points represent conditions for which the resulting superlattice is periodic; the x axis is the twisting angle θ_0 and the y axis is the period of the superlattice R_p. For a finite size cluster, it is enough to draw a horizontal

[1]Co prime numbers are those numbers whose only common factor is 1.

line (such as the one in orange at $R_p = 6.7a$) and take a look at which points appear below that line. Basically, such a finite cluster can have all these commensurate phases by playing with the twisting angle. The two clusters on below the graph represent two commensurable phases of a $r = 6.7a$ cluster, marked in red in the upper graph. Red scatterers in the cluster indicate the position of the points where both lattices coincide, that is to say, the period of the superlattice. As it can be seen, even if the structures are different, they keep six-fold symmetry.

Relative rotation between clusters allows for the formation of a set of "dipoles".This parameter tunes the distance between the scatterers forming the dipole. These resonators are closer to each other than they are to the scatterers of the individual lattices, allowing stronger interaction between them. The centre of the cluster is also the centre of the rotation; therefore, the relative distance between the dipoles depends on the relative position of the scatterers in the cluster. A large number of dipoles is formed, and a large number of different resonant modes appears.

3.3 Potential function and matrix analysis

The aforementioned dipoles are responsible for the strong localisation characteristics of these kind of structures. It is certainly necessary to define a "cluster potential" function to find whether we are geometrically close to a strong localisation area. The function $\mathcal{U}$ is defined as

$$\mathcal{U} = \frac{1}{N_c^2} \sum_{\forall a,b} \frac{1}{|\boldsymbol{R}_a - \boldsymbol{R}_b|}, \tag{3.7}$$

where N_c is the number of scatterers in one of the original lattices, so that the total number of resonators in the cluster is $N = 2N_c$. This potential function quantifies how close the scatterers from lattice a are with respect to lattice b. The function will diverge when the commensurable condition is attained, indicating that the resulting cluster is periodic. Furthermore, this function depends on the radius of the cluster; therefore, only commensurate phases whose periodicity is smaller than the cluster's radius will be shown.

Once the mechanism describing the formation of localized modes has been understood, numerical simulations can be done so as to check our model. These simulations have been performed using the MST approach for flexural waves in thin elastic plates explained in Chapter 2. Taking the definition of the M in equation (2.97), we will assume that only the dipolar interaction in our cluster is relevant, so we consider that the matrix can be factorized into a set of 2×2 matrices M_d. Then, the modes of the cluster are given by the different modes of each dipole. Dipolar modes are defined by the zeros of the determinant of matrix M_d,

$$|M_d| = \left[t_0^{-1} - G(\mathbf{0})\right]^2 - G(\boldsymbol{R}_{\alpha\beta})^2, \tag{3.8}$$

where $\boldsymbol{R}_{\alpha\beta}$ is the distance between both scatterers. Resonators have been considered identical, so that $t_\alpha = t_0$, and their characteristic impedance does not have a resonance, avoiding the cancellation of the determinant by the resonance of the scatterers themselves. When the clusters are rotated, the position

of the particles in the dipole will change, and so the relative distance between them, having therefore a different resonance.

The system under analysis is an open system with no bounded modes of an infinite lifetime. Thus, condition $|M_d| = 0$ is only achieved for complex frequencies. Nevertheless, an approximated position for the modes (leaky modes) can be inferred by checking the smallest eigenvalue of M_d for real frequencies.

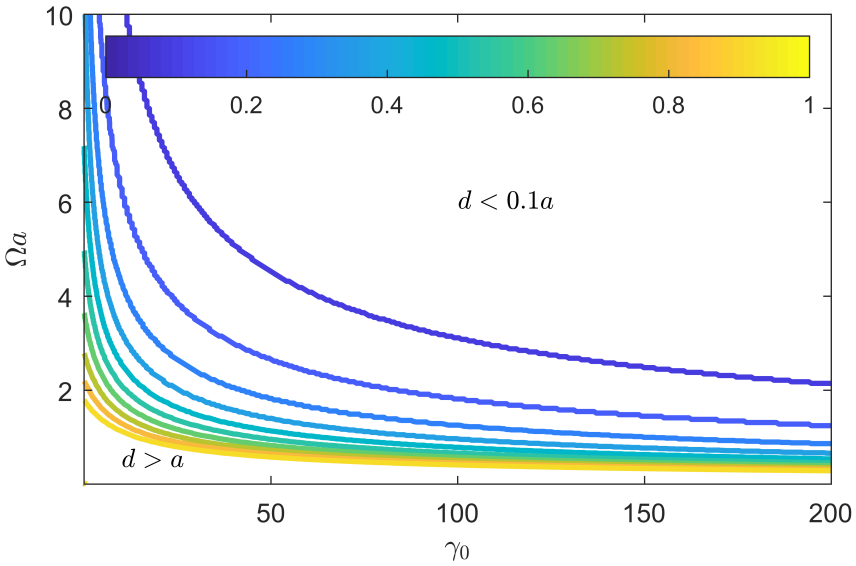

Figure 3.2: Dipolar distance (d) as a function of the frequency of the system (Ωa) and the normalized mass of the resonators (γ_0). The diagram defines three localisation regimes.

Figure 3.2 shows the contours for a constant distance between the dipoles, $d = |\boldsymbol{R}_{\alpha\beta}|$, as a function of the normalized frequency Ωa and the impedance factor γ_0. The resonance of the scatterer is selected to be far from the frequency range that we are analysing ($\Omega_R a = 20\pi$). Areas with $d > a$ and $d < 0.1a$ are left blank on purpose, since in the first case we can consider that the scatterers are separated enough so that other scatterers of the cluster interfere in the formation of resonances, while in the second case the scatterers are so close that resonances will only appear near the commensurate angles of the lattice. Dipolar resonances whose field is not so localized near the scatterers can be found in the middle range. Consequently, we will define three regions for the bilayer structure: weak localisation ($d > a$), spread dipolar localisation ($0.1a < d < a$), and strong dipolar localisation, $d < 0.1a$.

Figure 3.3 represents the behaviour of the whole cluster, by showing the evolution of the smallest eigenvalue (λ_{min}) of the M matrix of a circular cluster of radius $R_c = 6.7a$ and hard scatterers with $t_0 \approx \gamma_0 = 200$ (as explained in chapter 2, equation (2.84) defines the impedance of the resonator. We will consider "hard" or "soft" scatterers whenever the resonant frequency of the scatterer is higher than the frequency at which the system is evaluated, and the value of the normalized mass is high or low, respectively) as a function of the twisting angle and the normalized frequency of the system. The underlying lattice is a honeycomb lattice, and the total number of scatterers in each cluster is $N_c = 331$. The upper panel shows the cluster potential $\mathcal{U}$ corresponding to this family of structures. Blue points in

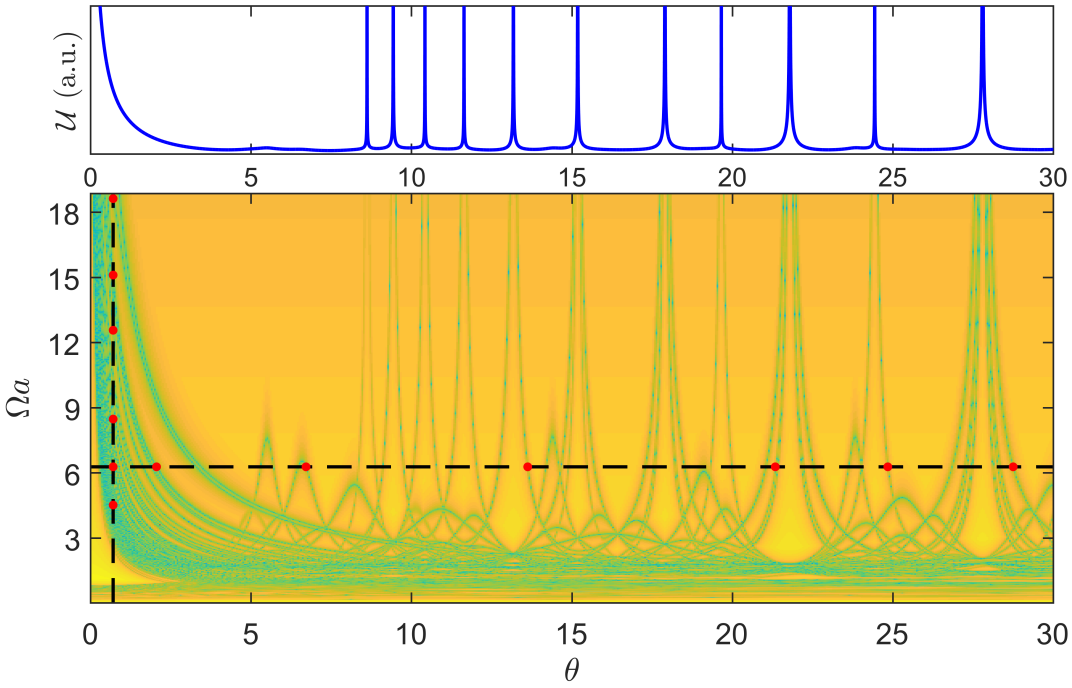

Figure 3.3: Behavior of a twisted bilayer finite cluster with honeycomb lattices as original lattices. The upper panel shows the evolution of the cluster potential $\mathcal{U}$ with the rotation angle, while the lower panel represents the smallest eigenvalue of the M matrix as a function of the rotation angle and the frequency of the system. The radius of the cluster is $R_c = 6.7a$. The modes indicated in red are depicted in Fig. 3.4 and Fig. 3.5.

the colormap represent values of the eigenvalue that are close to zero, that is to say, conditions where the mode is likely to happen. On the contrary, green and yellow areas represent conditions for which resonances are not likely to appear. In the eigenvalue map, above $\Omega a = 2\pi$, strong dipolar localisation drives the formation of resonances, and two different types of modes can be distinguished. The first type of mode can be found in the map in the small rotation angle region ($\theta_0 \in [0°, 5°]$). In this region, the scatterers of the two clusters are very close to each other. This is the main reason for having so many modes in this region; for a small twisting angle, many dipoles are formed between the two lattices, but the distance of the scatterers is slightly different for the different dipoles, spanning their resonances through a wide frequency region. Above these firsts angles, the scatterers of each cluster are too far away from each other, making dipolar modes not possible. The second type of mode is related to the peaks of $\mathcal{U}$, i.e. the commensurate phases of the cluster. There are some modes corresponding to some of the commensurable phases that seem to be split in two. This phenomenon can be explained by taking a look at the periodicity for these commensurable phases. The period is so small in these cases that two periods appear at the same time. Due to the distance to the centre of the structure, the relative distance of the dipoles belonging to the first period are different from the distance of the dipoles belonging to the second period. Thus, the resonance is divided in two branches with different resonant frequencies. Near some

other angles in the map ($\theta_0 = 5°, 6°$ or $14°$), some modes appear, but they do not correspond to any peak of the $\mathcal{U}$ function. However, there are some dipoles in these structures that are close enough to excite a resonance.

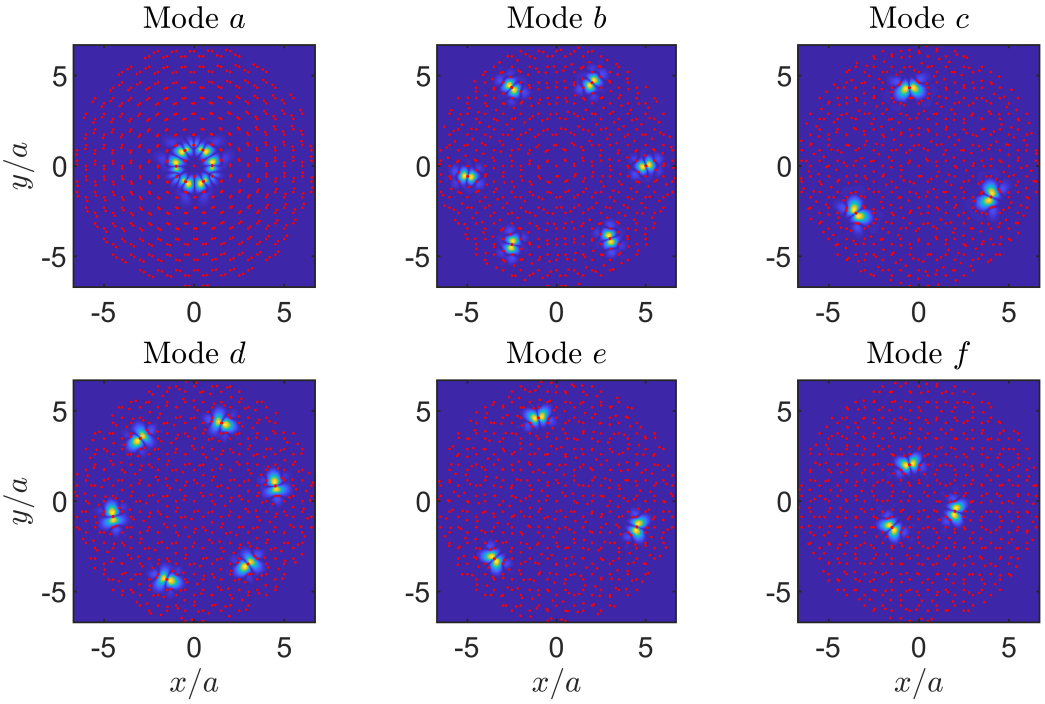

Figure 3.4: Eigenmodes corresponding to the red dots of the horizontal line $\Omega a = 2\pi$ of Fig. 3.3.

Figure 3.4 shows some examples of the different localized eigenmodes that are found in the previous figure. All the modes are found at the same frequency $\Omega a = 2\pi$, and they are marked in Fig. 3.3 as red dots in the horizontal line. From $\boldsymbol{a}$ to $\boldsymbol{f}$, the twisting angles at which they are found are 2.05°, 6.71°, 13.62°, 21.34°, 24.84° and 28.75° respectively. These modes are found for the same frequency, but different geometrical configuration; they present localisation, however, we cannot have two of them in the same experimental set up with the same structure, unless we unveil a mechanism for rotating both lattices actively. On the other hand, we can study the same geometrical configuration and analyse its behavior with frequency. As explained before, twisting configurations with really small angles present higher density of modes than the rest of the map. Therefore, we will chose some small angle to study the variation of modes with frequency.

Figure 3.5 shows six different modes belonging to the vertical line $\theta = 0.7012°$. Each mode has different frequency, but the geometrical properties are the same for all of them. From $\boldsymbol{a}$ to $\boldsymbol{f}$, they can be found at 1.44π, 2π, 2.7π, 4π, 4.81π and 5.93π respectively. These are modes that also present localisation. In this scenario, all the six modes can be obtained with the same structure, just by properly tuning the frequency range. Furthermore, the modes are spanning a wide frequency range, from 1.4π to almost 6π.

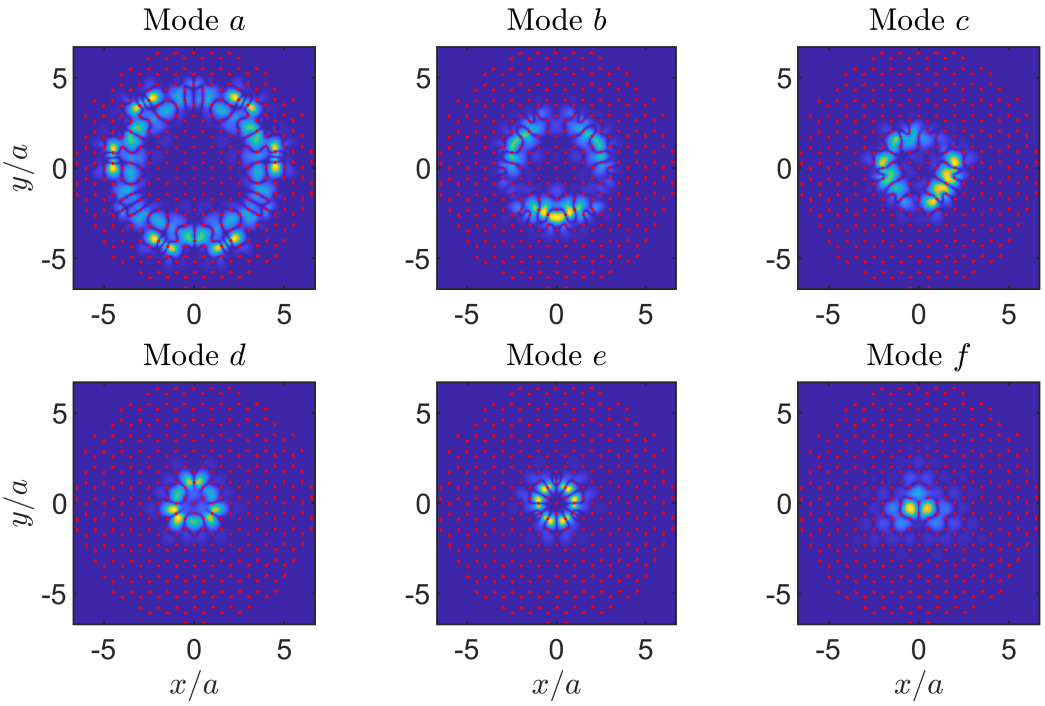

Figure 3.5: Eigenmodes corresponding to the red dots of the vertical line $\theta = 0.7012°$ of Fig. 3.3.

3.4 Scatterer's impedance

In this section, the impact of the scatterer's impedance on the dimerized localisation of states is discussed. Figure 3.6 depicts the behaviour of the smallest eigenvalue of the M matrix for a twisted bilayer made with two honeycomb lattices as a function of the twisting angle and the frequency. In this picture, the scatterers' impedance is "soft" ($\gamma_0 = 2$).

When compared with the map in Fig. 3.4, the number of modes (blue colour in the map) that appear is higher; the complexity of the system is enormous, and we cannot distinguish any more the modes located around the commensurate phases of the crystal. If we visualize the eigenstates corresponding to some eigenmodes, we will be able to see that we do not have strong dipolar interaction between scatterers, but the elastic field is located within a bigger group of resonators. Undoubtedly, the behaviour of these modes is more complicated and difficult to predict. Our model of resonator, defined in equation (2.84) allows us to find a frequency for which the impedance of the resonator is higher, therefore we will retrieve the strong dipolar interaction at higher frequencies, close to the resonance of the scatterers.

As it can be seen in Fig. 3.7, the spatial distribution of the eigenmodes for a $\gamma_0 = 2$ twisted bilayer is more complex than in the case of hard scatterers. Modes ***a*** and ***b*** present spread dipolar interaction instead of strong dipolar interaction, as it happened for the $\gamma_0 = 200$ structure. In order to achieve high impedances, when γ_0 is small we have to increase the frequency. Thus, those modes having higher frequencies are the ones that are more confined in space (panels ***e*** and ***f***).

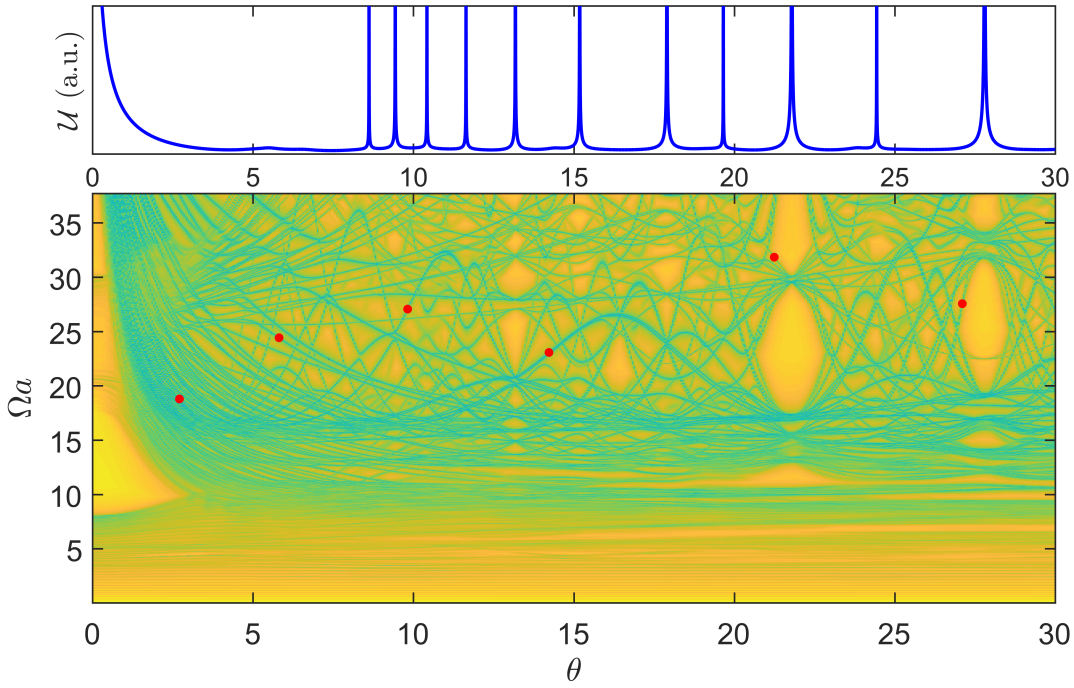

Figure 3.6: Absolute value of the smallest eigenvalue of the M matrix as a function of the twisting angle and the frequency of the system for a $\gamma_0 = 2$ honeycomb twisted bilayer. The modes indicated in red are depicted in Fig. 3.7

3.5 Anisotropy

This section focuses on the effect of changing the anisotropy of the original lattices forming the bilayer. For that purpose, we are going to use twisted bilayers made out of rectangular lattices. The point positions in the lattice will be defined as

$$\boldsymbol{R}_{nm} = na + im\eta a, \tag{3.9}$$

where a is the original lattice parameter (square lattice), and η is the anisotropy ratio of the lattice.

Figure 3.8 shows how anisotropy in the lattice affects the dimerized behavior of the system. First of all, a frequency of the system in which the modes found are dimers is fixed. Panel **a** shows the evolution of the modes of the system as a function of the twisting angle and the frequency of the system. This is the same graph as Fig. 3.3, but we have a square lattice, not a honeycomb one. At $\Omega a = 2\pi$, we can clearly see that the system is dominated by a bunch of modes around the commensurate phases of the cluster, as explained in section 3.3. Therefore, this frequency will be fixed, and anisotropy is going to be introduced in the system.

Panel **b** depicts the evolution of the dimerized modes as a function of the twisting angle and the anisotropy ratio of the original lattices. The bottom line of this panel ($\eta = 1$) is the same as the black

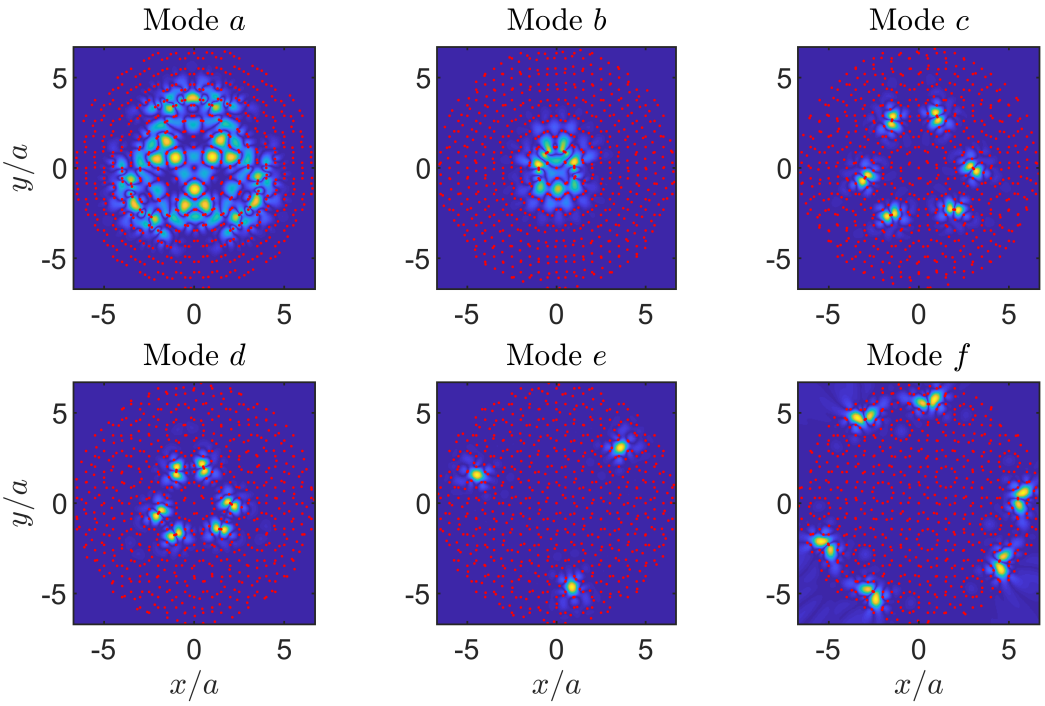

Figure 3.7: Eigenmodes corresponding to the red dots of the vertical line $\theta = 0.7012°$ of Fig. 3.6.

dashed line in panel **a**. Two kind of structures can be distinguished in this geometrical space map: the former structure is formed by the "lines", whose origin is the dimerized modes and that change their twisting angle when the anisotropy of the lattices changes. The latter ones are those ellipsoidal structures that appear all alone in the graph or at the intersection between linear structures. While eigenmodes belonging to the "linear" structures present very similar spatial shape between them, that has been previously analysed in section 3.3, eigenmodes belonging to the ellipses show a more sophisticated pattern.

Figure 3.9 shows the eigenmodes belonging to one of the ellipsoidal features of the anisotropy map. Panel **a** is an insight of one of these structures in the previous figure: one that can be found at the intersection between linear features. Panels **b** to **e** show the eigenmodes belonging to some of the geometrical configurations of the ellipse. It can be pointed out that all the modes are localized around the same pairs of scatterers. However, the dipoles radiate in different directions, depending on their position in the ellipse in the geometrical map. If more eigenmodes are observed, following the trajectory of the ellipse, it will be found that the radiation of the dipoles rotates with the trajectory of the ellipse. This phenomenon can be easily explained; one of the scatterers in the dimmer is either geometrically fixed or suffering from a vertical translation (the one that belongs to the original lattice), while the other is suffering from both vertical displacement and rotation. The relative distance between both resonators is always the same, but the one that rotates is describing a circle around the one belonging to the original lattices, producing this interesting phenomenon.

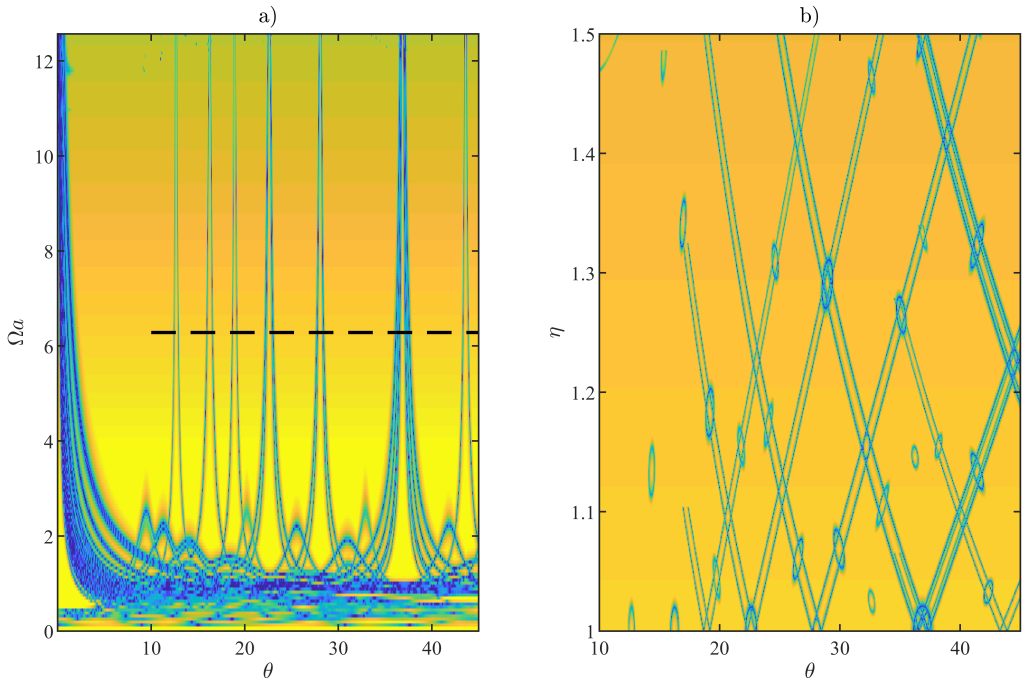

Figure 3.8: Anisotropy effect on the apparition of dimerized modes of the twisted bilayer. Panel **a** shows the evolution of the minimum eigenvalue of the M matrix as a function of the twisting angle and the frequency of the system for a square lattice twisted bilayer. Panel **b** shows the evolution of the same system but this time fixing the frequency at $\Omega a = 2\pi$ (black dashed line in panel **a**) and changing the anisotropy of the original lattice.

3.6 Quality factor

This section is devoted to the analysis and discussion of the quality factor of the resonances in a twisted bilayer crystal plate. Results shown here correspond to twisted bilayer clusters formed by the superposition of two triangular lattices, relatively twisted by an angle θ_0.

Figure 3.10 shows some results for clusters with "hard" (as in section 3.3) or clamped scatterers ($\gamma_\alpha = 200$). The left panel represents the minimum eigenvalue evolution we have been discussing before. The same features as in Fig. 3.3 can be retrieved. Nevertheless, whereas honeycomb lattice has two scatterers in its unit cell, triangular lattice only has one. This is the reason behind the clarity in the eigenvalue map with respect to the honeycomb one. Top right panel shows the eigenvalue evolution in frequency for two different geometrical arrangements ($\theta_0 = 9.1°$ and $\theta_0 = 9.3°$). The frequency axis in this graph stands for the real part of the frequency term, while the imaginary part is kept at zero. The green curve shows a sharp resonance with a high quality factor ($Q = 81.4$), while the orange curve has a broader resonance with low quality factor ($Q = 4.6$). These results can be compared with those obtained in the bottom right panels. In there, the evolution of the minimum eigenvalue is shown for the two geometrical arrangements selected before but in the complex frequency plane. Real frequency

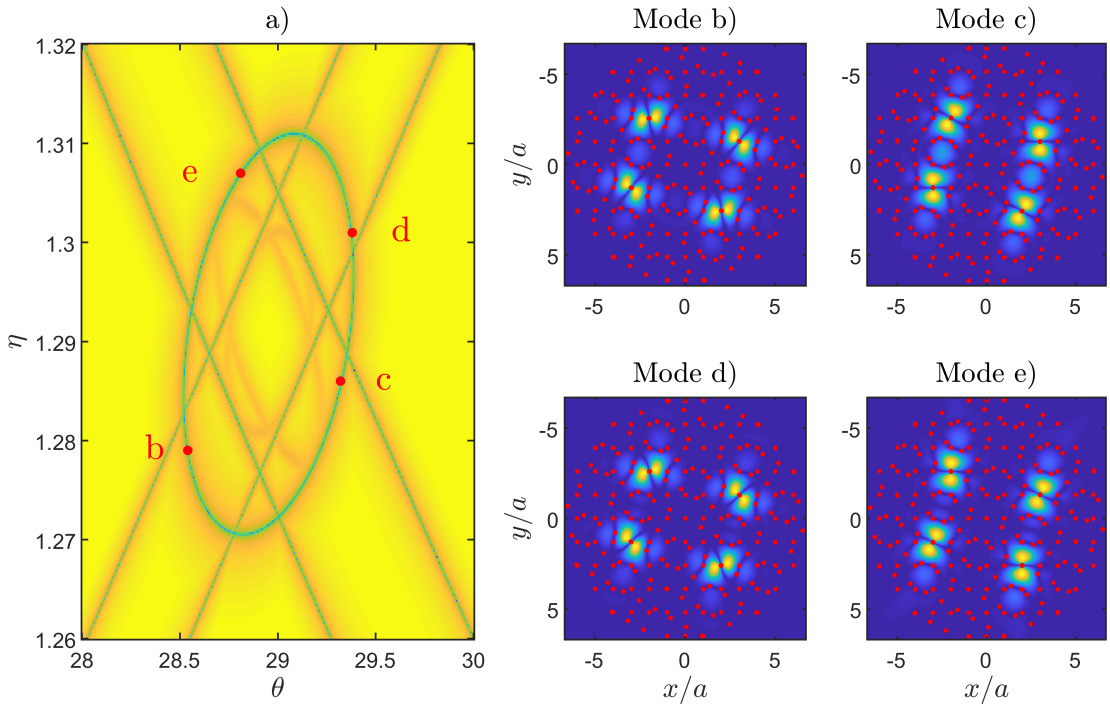

Figure 3.9: Panel **a** shows a insight of Fig. 3.8 panel **b**, around the ellipsoidal feature in the middle of the map. Panels **b** to **e** show four eigenmodes marked by red points in panel **a**, all of them belonging to that structure.

is kept near the minimum found for the top right panel (we assume that the real frequency component of the minimum in the complex frequency plane is very similar to the one obtained by just using real frequencies). Red points in the complex map indicate the position of the minimum in the real frequency axis, that is to say, in the left and the top right panels. One can appreciate that, while the first complex map shows the minimum of the eigenvalue function close to the centre of the map, the second complex map has a shift in the minimum value. As explained in Chapter 2 section 2.6, the shift is inversely proportional to the quality factor of the resonance; and thus we can conclude that the quality factor is higher in the first resonance than in the second one, which coincides with our analysis of the widths of the resonances in the real frequency line (Fig. 3.10 panel **b**)).

Figure 3.11 has the same structure as Fig. 3.10. This time, the normalized mass of the scatterers is $\gamma_\alpha = 20$; then, the scatterers are softer. As explained in section 3.4, the softer the scatterers in the cluster are, the more we get into the "spread dipolar localisation phase". Thus, the eigenvalue map looks more complex than in the case of hard scatterers. In order to have pure dipolar interaction, we have to increase the frequency of the system. Two different geometrical configuration have been chosen, and their resonances have been analysed. Top right panel has been split in two different graphs for the sake of clarity. The real frequency range did not allow to take a look at the width of both resonances at the same time. This time, we can clearly state that the first resonance (corresponding to a twisting angle of $\theta_0 = 8.86°$) is broader (and therefore its quality factor is smaller, $Q = 5.98$) than the second resonance

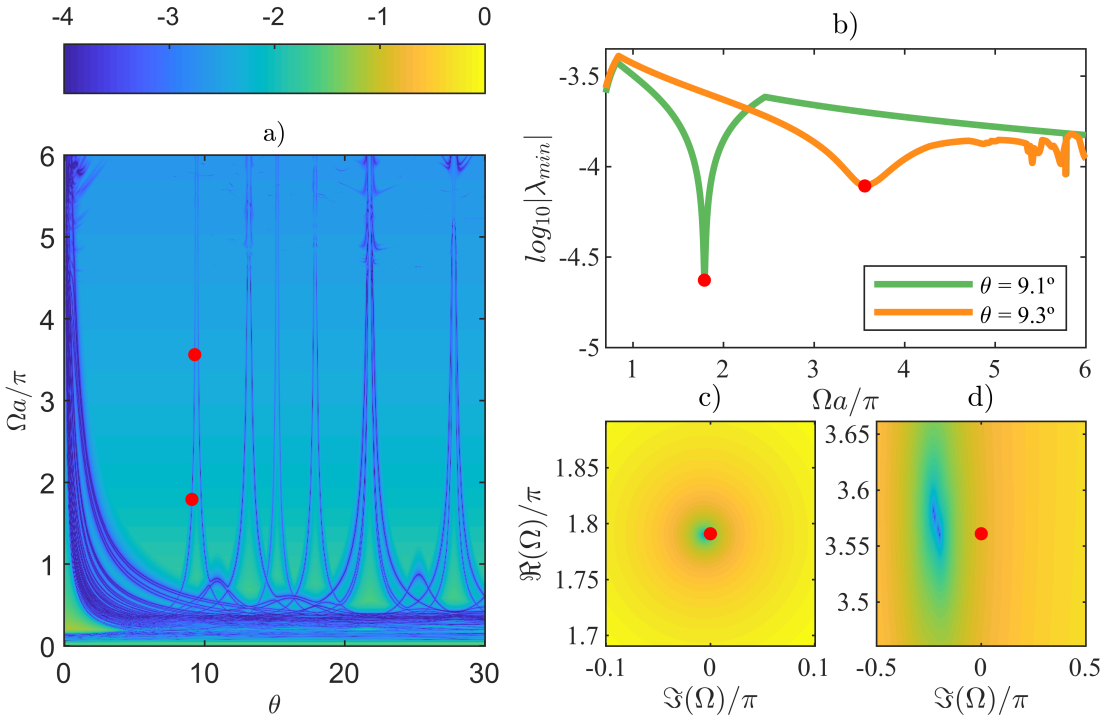

Figure 3.10: Panel **a** represents the modes of the system as a function of the twisting angle and the normalized frequency (real frequency). The structure is composed by two triangular lattices. Panel **b** depicts the evolution in frequency of two geometrical configurations at $\theta_0 = 9.1°$ and $\theta_0 = 9.3°$. Panels **b** and **c** show the modes at the geometrical configurations in panel **b** but evaluated in the complex frequency plane.

($\theta_0 = 14.17°$).

In addition, other resonances with more complicated behaviour can be found for the softer ($\gamma_\alpha = 20$) twisted bilayer. In figure 3.12, two different resonances are shown, both in real frequency and complex frequency representation. The upper one is found for $\theta_0 = 12.47°$ and $\Omega a/\pi = 3.62$. This point belongs to the dipolar resonances in Fig. 3.11. The resonance is split in four different minima, with the same quality factor (the distance from the central line of the complex map is the same). As for the second mode, found in $\theta_0 = 0.65°$ and $\Omega a/\pi = 2.47$, it belongs to the small angle zone in Fig. 3.11. The behaviour of the eigenvalue with real frequency shows a single minimum with a wide resonance and low quality factor ($Q = 20.58$). On the other hand, the complex frequency plane divides this wide resonance into three different modes with different quality factors and real frequencies.

3.7 Robustness

In this section, the robustness of these structures will be discussed, paying attention at the evolution of the dimerized eigenmodes when some noise is introduced in the system.

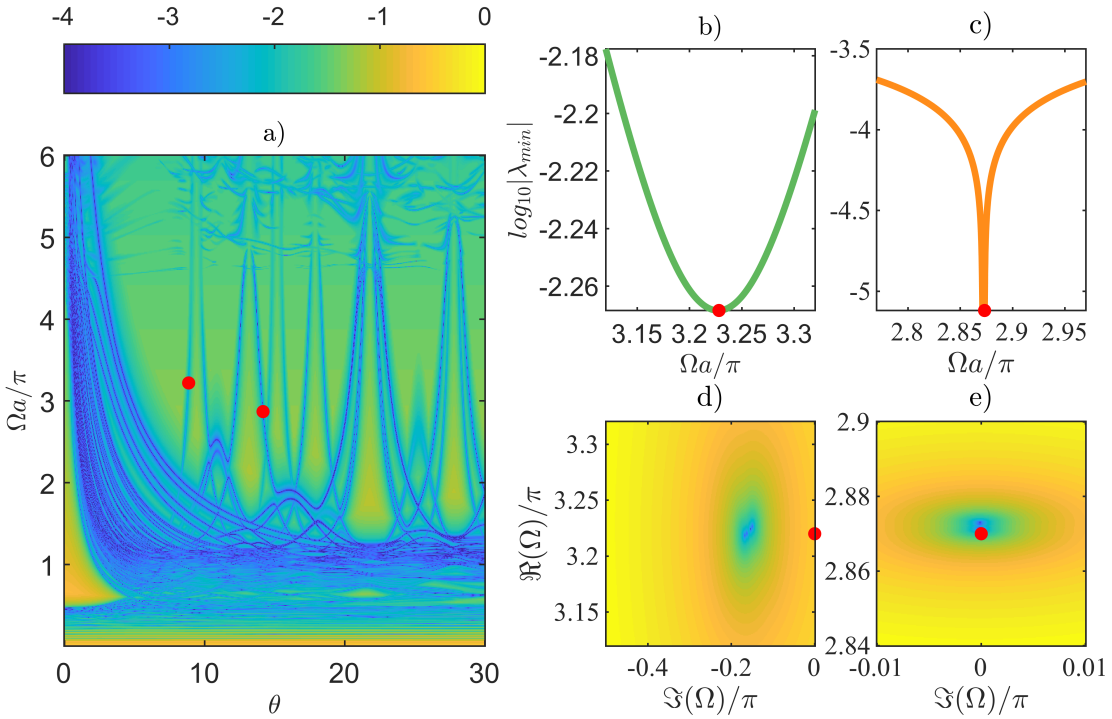

Figure 3.11: Panel **a** represents the modes of the system as a function of the twisting angle and the normalized frequency (real frequency). The structure is composed by two triangular lattices. Panel **b** depicts the evolution in frequency of two geometrical configurations at $\theta_0 = 8.86°$ and $\theta_0 = 14.17°$. Panels **b** and **c** show the modes at the geometrical configurations in panel **b** but evaluated in the complex frequency plane.

Figure 3.13 depicts the behavior of one dimerized resonance when adding positional noise to the twisted bilayer. The original structure is made by superimposing two honeycomb lattices with a twisting angle of $\theta = 12.8°$. Panel **a** shows the behavior of the minimum eigenvalue of the M matrix. Recall that the minimum value of this parameter indicates the presence of an eigenmode of the system. The blue line is for the unperturbed cluster. A resonance is found at $\Omega a = 7.33$. The eigenmode corresponding to this resonance is shown in panel **b**. As expected by the symmetry of the original lattices, the eigenmodes has three-fold symmetry. Then, the cluster is perturbed according to

$$\mathbf{R}_{nm} = (n + \sigma\mathcal{N}(0,1))\,\mathbf{a}_1 + (m + \sigma\mathcal{N}(0,1))\,\mathbf{a}_2 \pm \frac{1}{6}(\mathbf{a}_1 + \mathbf{a}_2)\,, \tag{3.10}$$

where $\mathcal{N}(0,1)$ is a Gaussian distribution with zero mean and unitary variance, and σ characterizes the amount of noise introduced to the system. Numerical results can be seen in Fig. 3.13: the eigenvalue is shifted from its original frequency, and more minima appear. Even if the amount of noise is barely appreciable (there is no noticeable difference in position for the four panels **b** to **e**, with noise levels equivalent to 0.1%, 0.2% and 0.3% with respect to the lattice parameter), the resonance gets easily destroyed. The minimum is kept for the first two simulations, but for $\sigma = 0.003$ it disappears or is largely

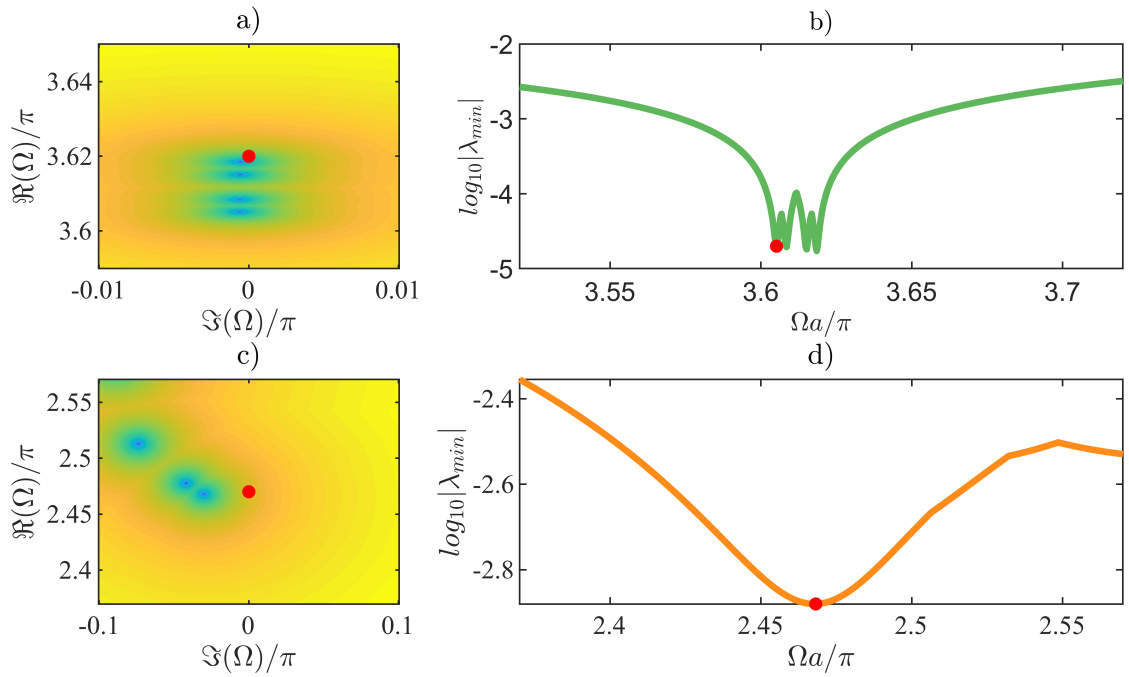

Figure 3.12: Two resonances appearing in a triangular lattice twisted bilayer with $\gamma_\alpha = 20$. The first resonance in panels **a** and **b** is evaluated at $\theta_0 = 12.47°$, presenting four different minima. The second resonance ($\theta_0 = 0.65°$), shown in **c** and **d**, is broader. However, the complex frequency map shows the presence of different minima in the region where the resonance is found.

shifted. When looking at the eigenmode, the symmetry is completely lost, and we can consider that the mode has been destroyed, even with the tiniest amount of disorder in the system.

As a consequence, we can state that dimerized modes in a twisted bilayer are very sensitive modes that are not robust against disorder.

3.8 Conclusion

This chapter has proven the versatility of twisted bilayers for having localisation of mechanical waves in thin elastic plates. When changing the twisting angle, or sweeping in a frequency range, a panoply of dimerized modes can be excited. This system is really interesting for wave manipulation, since the simplicity in the definition of its geometrical parameters, and therefore in the manufacturing of samples contrasts with the complexity of states that are obtained. The amount of geometrical dispositions that can be tuned is not reduced to the twisting angle, but many other can be used for producing localized states. In this chapter, anisotropy has also been explored, but the reader could thing of other mechanisms, like changing the lattice parameter between both layers, shifting both lattices by translation, or shrinking or stretching the distance between resonators in the case of the honeycomb lattice.

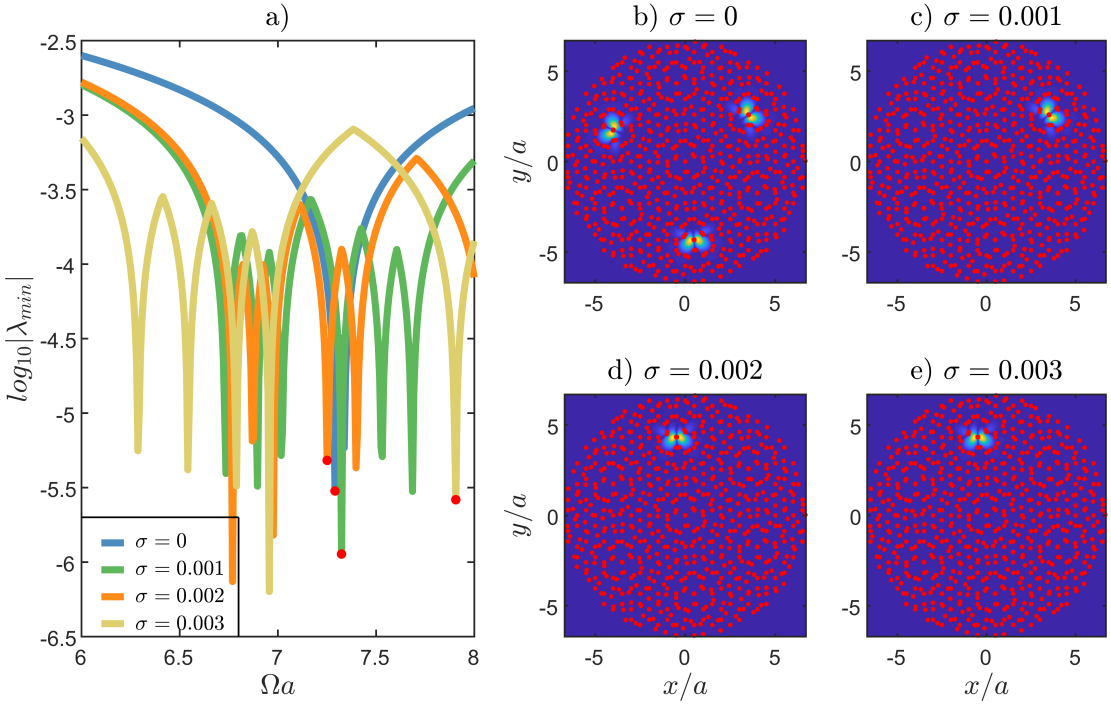

Figure 3.13: Disorder effect on the eigenmodes of the twisted bilayer. Panel **a** shows the evolution of the minimum eigenvalue of the M matrix as a function of the frequency and the noise induced in the position of the scatterers. Panels **b** to **e** show the eigenmode corresponding to the modes marked with red points in panel **a**.

Chapter 4

Quasi-periodic linear arrays of scatterers

4.1 Introduction

The advent of topological materials in condensed matter physics [71, 72] has lead to new and exciting phases of matter with remarkable properties. One of the key features of topological insulators is the existence of robust edge states that are immune to backscattering from disorder or interface variations. [73, 74] These modes have attracted the attention of the scientific community due to their capacity of manipulating waves propagating through the structures; therefore, classical analogues of these states have received increasing attention. [73, 75–78]

In acoustics and elasticity, topologically protected edge states have been studied in a wide variety of periodic and quasi-periodic materials. [30, 54, 79–88] If the structure exists in a N dimensional space, the interface of such a structure will have $N - 1$ dimensions, and will propagate without suffering backscattering. If N is equal to 1, the interface state is a topologically protected zero-dimensional bound mode. Other protected states have been recently found in two-dimensional domains by means of the classical analogue to the Majorana fermion. [32, 89, 90] Nevertheless, all these states are surrounded by the bulk material. Thus, their excitation might require propagation outside the domain of interest or penetration through a gaped material.

In this chapter, localized interface modes will be designed in mechanical systems, considering a quasi-periodic line of scatterers embedded in a two-dimensional elastic plate. MST has been applied to the study of these structures [91–93]. This method contrasts against the other methods used for analysing these structures, based on super-cells and Floquet-Bloch theory. [94] These techniques introduce some artifacts due to the additional periodicity that are not obvious on some occasions. In section 4.2 we study how bound modes appear in the line of scatterers when these are rigid enough and that the spectrum of these modes follows the well-known Hofstadter butterfly [95] in the appropriate space. Section 4.3 discusses the apparition of edge states in the gaps of the butterfly for finite clusters. Similar results were obtained for Rayleigh waves in resonators over a half-space substrates in [96], for beams over grounded springs in [97], beams with resonators on the top surface in [82], change of height in a beam in [98] or mechanical inerters in [99]. By adding the mirror symmetric version of the cluster and facing

them, the quality factor of these states is enhanced, and they change from edge states to interface states. Furthermore, section 4.4 shows some numerical simulations in which positional disordering is added to the cluster in order to study their robustness. Quality factor of such edge modes is discussed in section 4.5, and a brief discussion concerning methods for generated quasiperiodic arrays is done in section 4.6, with some remarks that lead the path for future work in the topic.

The modes discusses all along the chapter have the advantage of being zero-dimensional, confined within two one-dimensional "bulk" materials in a two-dimensional space. This offers significant practical benefits as the bound state is not completely encircled by bulk structures.

4.2 Matrix analysis and Hofstadter's butterfly

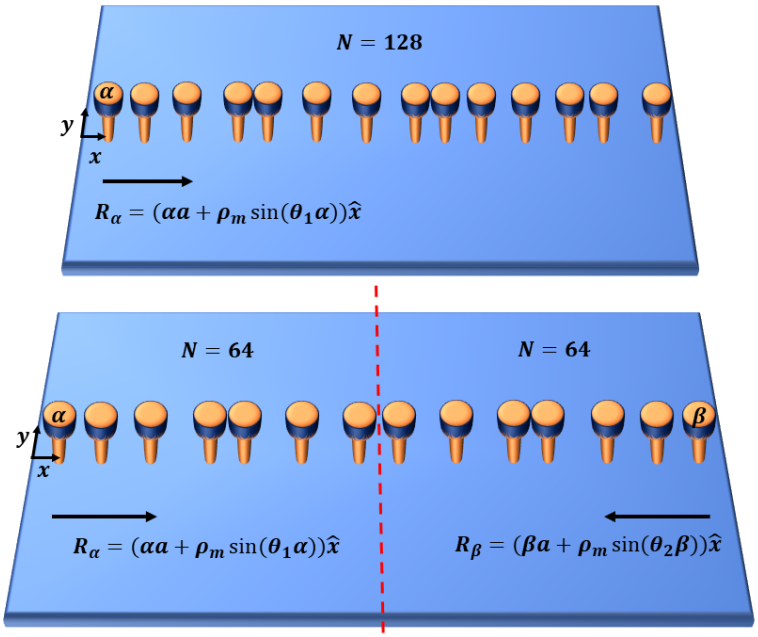

Figure 4.1: Geometry of the clusters analysed in the chapter. The upper drawing shows a quasi-periodic line of scatterers attached to the top surface of a thin elastic plate, while the lower one depicts the same configuration but merged with its mirror symmetric version.

Let us assume a cluster of N point scatterers attached to a thin elastic plate (as in Fig. 4.1) in positions $\boldsymbol{R}_\alpha$ for $\alpha = 1, 2, ..., N$. These resonators are arranged in a linear quasi-periodic distribution following a modulation rule given by

$$\boldsymbol{R}_\alpha = a\alpha + \rho_m \sin(\alpha\theta). \tag{4.1}$$

where a is the lattice constant, so the term $a\alpha$ defines a periodic arrangement. ρ_m is the radius of the modulation circle and θ is the angle rotated in the circle (as defined in Ref. [81]). If the cluster is infinite

($N = \infty$), then it is periodic as long as $\theta/2\pi \in \mathbb{Q}$. In the case of a periodic lattice, the number of scatterers forming a period is q, and it can be found by applying the condition $q\theta/2\pi \in \mathbb{Z}$. This modulation is equivalent to the almost Mathieu operator introduced by Peierls [100] to study the electron dynamics under magnetic fields. This operator is written

$$\left[H_{\omega}^{\lambda,\alpha}u\right](n) = u(n+1) + u(n-1) + 2\lambda\cos\left(2\pi(\omega + n\alpha)\right)u(n), \tag{4.2}$$

where α, ω and $\lambda > 0$ are parameters. This operator is also called Harper's equation for $\lambda = 1$. This equation is relevant because of its spectral behavior depending on the nature of the parameters in the model. If α is a rational number, then the operator is periodic, and by means of Floquet theory its spectrum is found, being purely absolutely continuous.

When α is irrational, the parameter ω is not relevant, and only λ plays a role on the spectrum. Depending on α, the spectrum can be:

- For $0 < \lambda < 1$, the operator has surely purely absolutely continuous spectrum.
- For $\lambda = 1$, the operator has surely purely singular continuous spectrum for any irrational α.
- For $\lambda > 1$, the operator has almost surely pure point spectrum and exhibits Anderson localisation.

The spectrum of the almost Mathieu operator is known to be a Cantor set for all irrational α and $\lambda > 0$. [1]. The Lebesgue measure of the spectrum is exactly zero for $\lambda = 1$, meaning that the spectrum has zero measure. The study of this specific case ($\lambda = 1$) leads to the Hofstadter's butterfly. This is the main feature that we are trying to recover with our spatial modulation on the scatterers in the thin elastic plate.

Eigenmodes of the finite plate will be studied by analysing the minimum eigenvalue of the M defined in equation (2.97), as it has been done with the twisted bilayer structures in Chapter 3.

Figure 4.2 shows what it is known as the phase space spectrum. It is not a real dispersion relation, in the sense that the x axis of the figure is not the wavenumber, but the value of the main modulation parameter. It is therefore a synthetic space where each column of the map represents a different geometrical configuration for the cluster of resonators. The fractal map that appears when evaluating the minimum eigenvalue as a function of both the modulation parameter and the frequency of the system is known as Hofstadter's butterfly [95]. Yellow zones in the graph represent regions in which it is not possible to have an eigenmode of the system, and blue regions are areas where it is likely to find one of them. Hence, the butterfly shape is mainly formed by yellow wide areas. Those regions cannot be directly called bandgaps as we are taking a look at a phase diagram, not at the dispersion relation of the system. Numerical results were obtained assuming $a = 1$, $\gamma_\alpha = 100$, $\Omega_\alpha a = 0.25$ and $\rho_m = 0.5$ in a cluster with $N = 128$ scatterers. If we take a look carefully at the interior of the butterfly wings, we will be able to see that certain thin blue lines (corresponding to eigenmodes of the system) cross the region from the upper band to the lower band of the butterfly wing. These resonances are called edge modes; their energy is localized in one end of the cluster. Figure 4.3 shows a zoom of one of the butterfly's wing, where the edge modes are clearly

[1] This result was proved by Avila and Jitomirskaya [101]

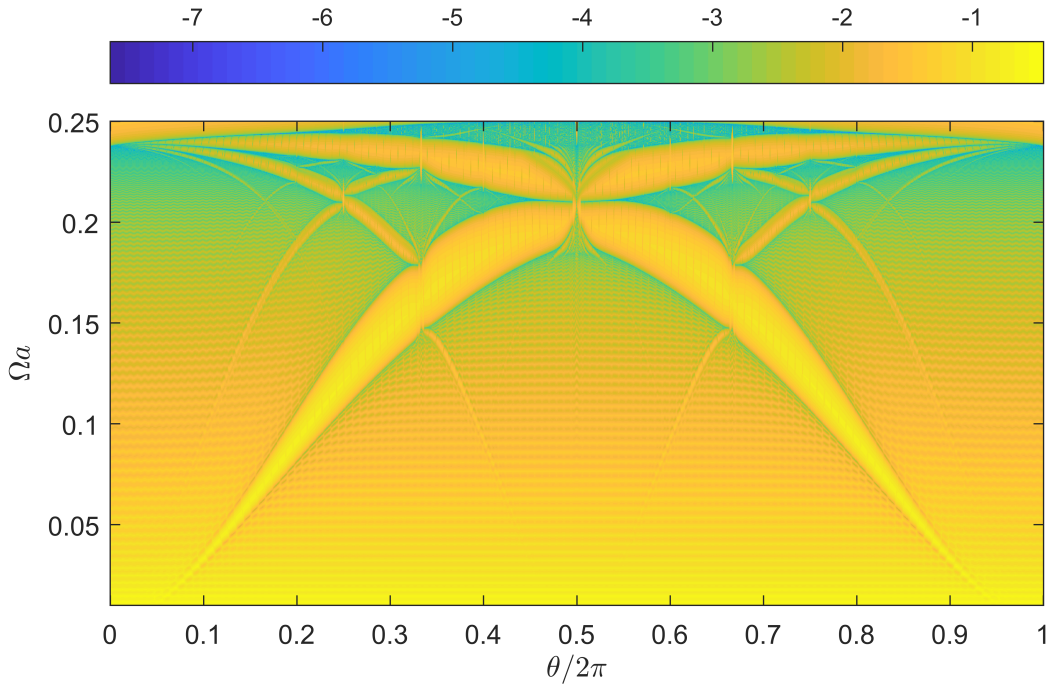

Figure 4.2: Evolution of the modes in the system as a function of the modulation parameter θ and the normalized frequency of the system Ω. The fractal feature that is seen in this map is the well-known Hofstadter's butterfly.

seen. In the case of an infinite system, those modes crossing the wings would not exist. However, as we are working with a finite system, the edge modes are related to the size of the cluster.

Considering that the modulation parameter θ is rational, we can say $\theta = p/q$, with p and q being coprime integers. If the plate is now infinite in the x axis (so that we have infinite number of resonators) and it is kept finite in the y axis, it will geometrically resemble an infinite hollow cylinder. Then, we can define periodic unit cell of q resonators in our infinite system. The motion of such a system will be described in terms of Bloch modes satisfying

$$w_b(x + qa) = e^{i\mu} w_b(x), \quad \mu \in [0, 2\pi], \tag{4.3}$$

where w_b is the vertical displacement field and μ is the Bloch's phase. Next, consider a finite plate with a large number S of resonators, with periodic boundary conditions at both ends of the x axis. These S resonators correspond to an integer number R of unit cells, $S = qR$. The modes when applying periodic boundary conditions in this case imply

$$w_r(x + aS) = w_r(x). \tag{4.4}$$

Then,

$$w_b(x + aS) = w_b(x + aqR) = e^{iR\mu} w_b(x). \tag{4.5}$$

The modes of the cylinders coincide with the Bloch modes ($w_b(x) = w_r(x)$ for $x \in [0, Sa]$) if $e^{iR\mu} = 1$, leading to the following condition:

$$\mu_r = \frac{2\pi r}{R}, \quad r = 0, 1, 2, ..., R. \tag{4.6}$$

The above range of r is chosen so that the wavenumber always belongs to the first Brillouin zone ($\mu \in [0, 2\pi]$). Thus, a finite cylinder discretizes the wavenumber into values μ_r. At these wavenumbers, the computed modes for the cylinder are a subset of the Bloch modes of the infinite periodic beam, and the eigenfrequencies of the cylinder are a discrete subset of the bulk spectrum.

The density of this subset increases with the number of unit cells R in the cluster, or equivalently, with the number of resonators $S = qR$ in the finite plate. If we want to analyse the bulk spectrum of the structure, the set of θ values that corresponds to commensurate cylinders must be obtained. The commensurability is satisfied for rational values of $\theta = p/q$, if the number of resonators satisfies $S = qR$, which gives

$$\theta = \frac{p}{q} = \frac{pR}{S}, \quad p, R \in \mathbb{Z} = \frac{s}{S}, \quad s = 0, 2, ..., S. \tag{4.7}$$

Therefore, the spectral properties of the infinite system can be investigated by discretizing the θ parameter range in steps $\Delta\theta = 1/S$, being S the number of resonators in the finite cluster. This will lead to an infinitely dense subset of $[0, 1]$ as $S \to \infty$.

Evaluation of the spectral properties of the structure at modulation angles θ others than the subset described before will result in the apparition of edge states in the wings of the butterfly. The position of those edge states in the phase diagram will depend on the number of resonators considered in the finite cluster; when the number of resonators is increased, the subset of angles that satisfy the commensurate condition also increases, densifying the bulk spectrum and making the slope of the edge states in the phase diagram steeper. The number of edge states between two commensurate angles in the phase diagram depends on the topology of the "bandgap" (butterfly wing) [73, 81, 85, 94].

4.3 Edge states and interface states

Figure 4.3 shows a region of the eigenvalue map inside one of the butterfly's wing for two different situations. On the one hand, left panel shows the computation of the eigenvalue map of a $N = 128$ resonators' cluster with a single modulation parameter θ. Edge states appear almost as vertical lines through the wing, but they are thin and their corresponding eigenvalue is not very small. This means, as will be discussed later, that the quality factor of this resonance is not very high. On the other hand, right panel shows the eigenvalue map of two $N = 64$ resonators' clusters. The main idea of this configuration is that each cluster is modulated with the same modulation parameter θ, but the origin of the modulation

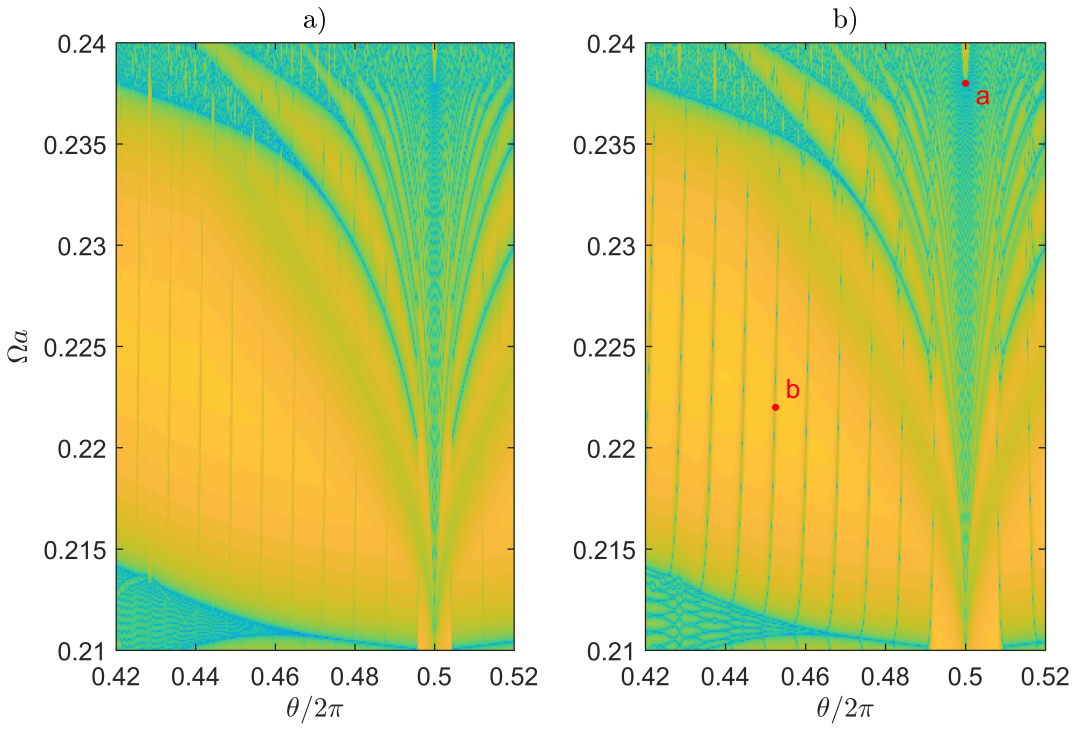

Figure 4.3: Panel **a** represents an insight of Fig. 4.2, where edge states appear inside the wings of the butterfly. Panel **b** shows the same region of the phase space but for the mirror symmetric cluster. Interface states can be seen more clearly in this second map.

is not the same; while the first cluster is modulated as in the previous case, the second cluster states its origin at the end of the finite cluster (as in Fig. 4.1). Therefore, the constructed cluster presents a mirror symmetry plane in the middle of the cluster. The idea beneath this configuration is to shift the energy of the edge states from the end of the cluster to the middle, thus becoming interface states. Furthermore, the modes crossing the butterfly wing have smaller eigenvalues than in the case of the single modulation, which stands for a quality factor enhancement.

Figure 4.4 depicts the eigenmodes for two different geometrical and frequency configurations in the mirror symmetric cluster. Both points are marked in red in Fig. 4.3 panel b. Mode ***a*** belongs to a periodic geometry ($\theta/2\pi = 0.5$), and it is not located inside the butterfly wing in the diagram. The eigenmode is not confined in a small region of the cluster; it propagates through the whole structure. The hotspots correspond to the classical profile of a standing wave trapped in a finite waveguide (the periodic array of scatterers). Besides, mode ***b*** is located in one of the vertical lines crossing the butterfly wing ($\theta/2\pi = 0.4525$); its eigenmode is clearly located in the centre of the cluster, where the mirror symmetry takes place.

It has been shown how the periodic finite line of scatterers supports bound states, as it is indeed a closed waveguide and, therefore, defines a resonant cavity. Introducing quasi-periodicity into the system increases the number of modes, and the phase spectrum maps Hofstadter's butterfly as a function of

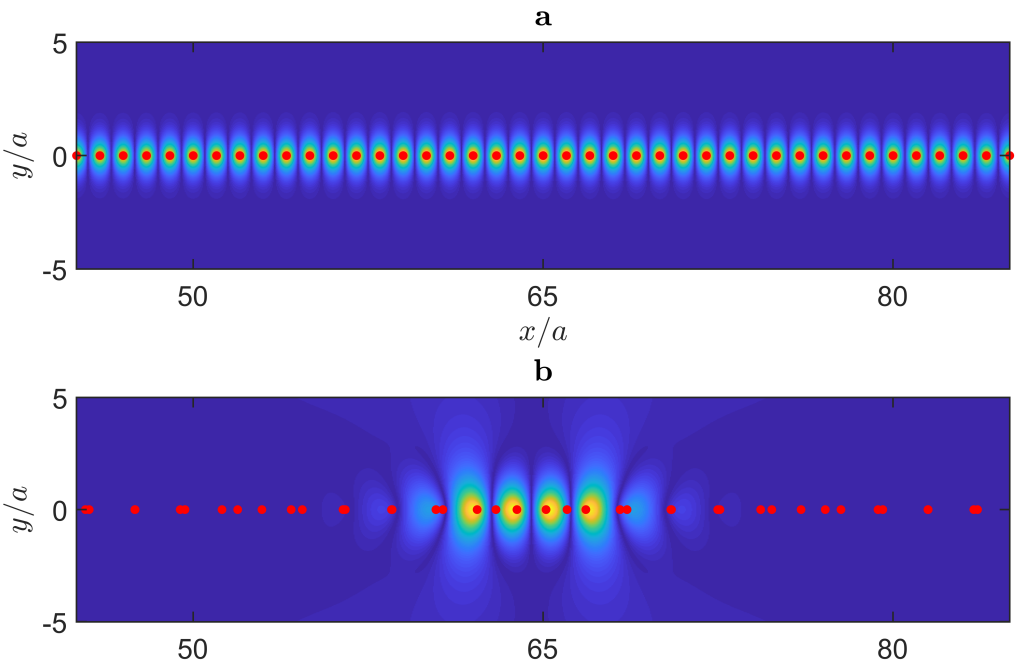

Figure 4.4: Eigenmodes pointed out in red in Fig. 4.3. Not all the cluster is shown, only the central part. **a** shows a propagating mode over the cluster with $\theta/2\pi = 0.5$. **b** exhibits a localised behavior, where the energy is confined in the centre of the cluster.

modulation defining the quasi-periodicity. Merging two clusters with faced modulations enhances the quality factor of the edge states.

4.4 Robustness

Edge states whose position in the phase space diagram reside inside the butterfly winds are well-known for their topological protection; that is to say, their robustness against small perturbations [73, 74]. In order to evaluate the robustness in the edge states found out in the previous section, we have performed numerical simulations with MST. The disorder method applied to test the robustness of the states is a perturbation to the x component of the position of each resonator in the cluster as follows

$$\boldsymbol{R}_{\alpha}^{\sigma} = \boldsymbol{R}_{\alpha} + \sigma a \mathcal{N}(0,1), \tag{4.8}$$

with $\mathcal{N}(0,1)$ being a normal distribution with unitary variance and zero mean. σ characterizes the amount of disorder applied to cluster by ensuring that all the scatterers are deviated from its initial position by a quantity that is normally distributed between $-3a\sigma$ and $3a\sigma$.

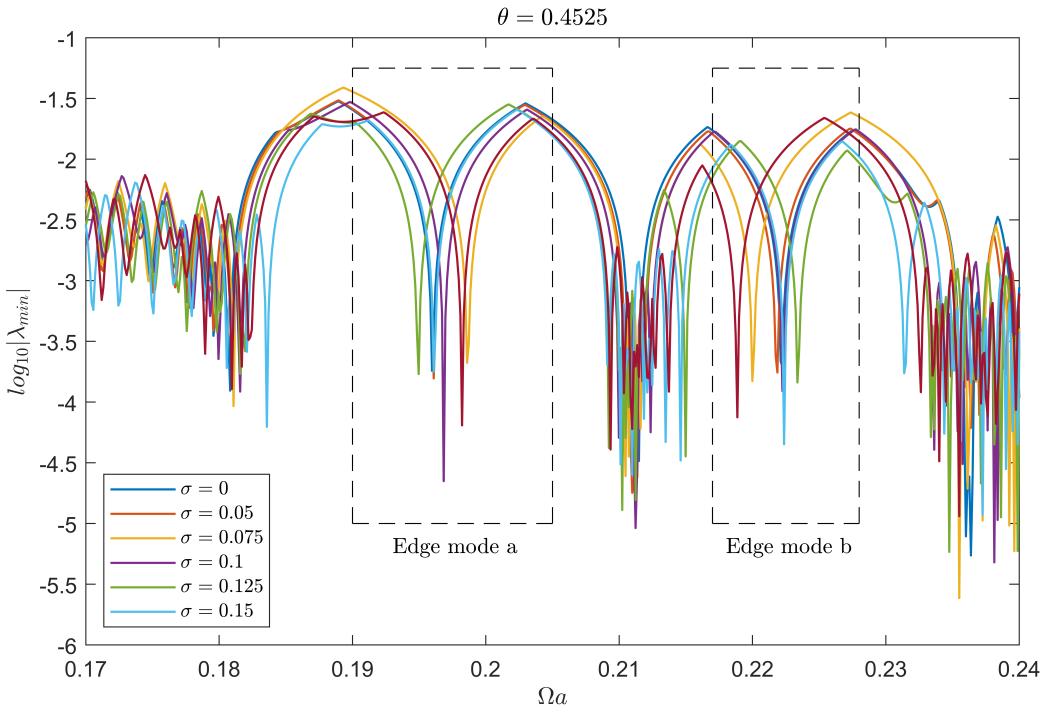

Figure 4.5: Evolution of the modes in the system for a faced cluster with $\theta/2\pi = 0.4525$ as a function of the normalized frequency of the system. Different degrees of disorder have been added to the cluster, each one represent by a different line. At both sides of $\Omega a = 0.21$, two localized modes are found.

Figure 4.5 shows the evolution of the minimum eigenvalue as a function of the normalized frequency of the system for a two-faced cluster configuration with $\theta/2\pi = 0.4525$ and for different amounts of disorder characterized by σ. There are two edge states; the two minima located at both sides of $\Omega a = 0.21$. It can be seen that, when adding disorder to the cluster, the edge state does not disappear; instead, it is slightly shifted in frequency, always remaining in the frequency range where the butterfly wing is. In Fig. 4.6 some of the eigenmodes for the edge states of Fig. 4.5 with frequency around $\Omega a = 0.19$ are shown. The amount of disorder applied for each eigenmode is indicated in the title of the map. The robustness and localisation of these modes is evident from these maps since the change in the shape of the field distribution is imperceptible.

4.5 Quality factor

Figure 4.7 panels a and b, show an insight of Hofstadter's butterfly. Left map corresponds to the linear array of scatterers without mirror symmetry, while right map corresponds to the two-faced cluster with mirror symmetry. The vertical lines appearing in the butterfly wing are edge states that exist due to the finite size of the studied cluster. One point has been chosen on each map. Their properties (modulation parameter and frequency) are not exactly the same for both modes. The reason is that the number of

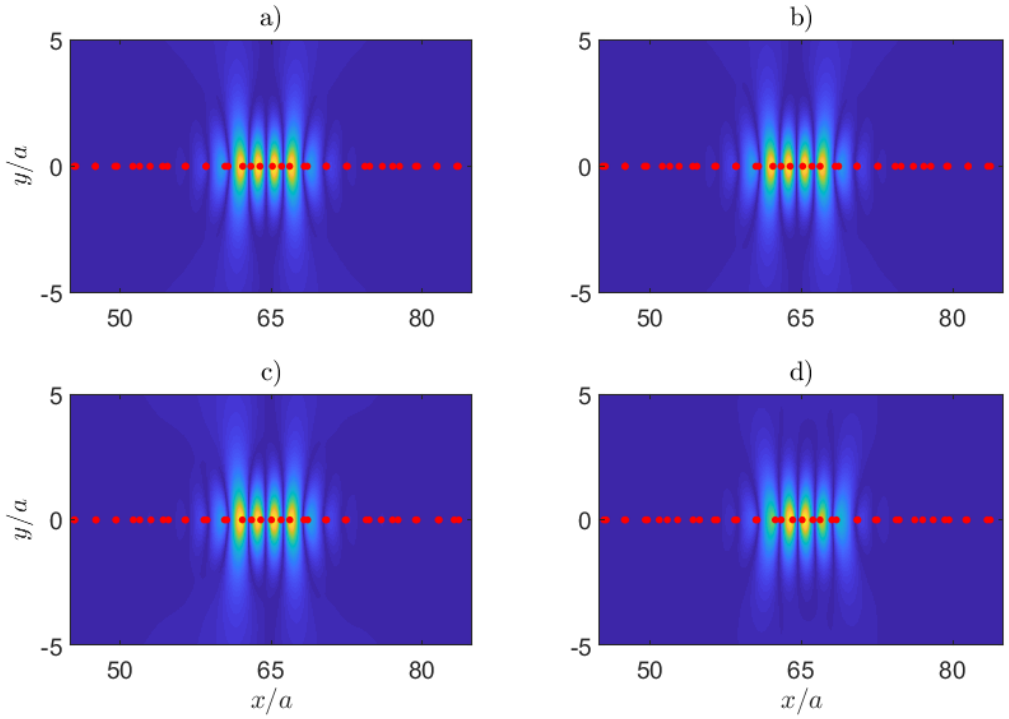

Figure 4.6: Eigenmodes corresponding to the modes in the wing of Fig. 4.5 around $\Omega a = 0.19$ for some clusters with different disorders applied over them.

scatterers is not the same: the left panel is computed with $N = 128$ resonators with the same modulation, therefore the commensurate conditions are found using this number. However, the mirror-symmetric cluster is made of $N = 64$ resonators, doubled with another $N = 64$ cluster. Thus, the commensurate conditions in this second case can be computed using 64 instead of 128 in the denominator of equation (4.7). Figure 4.7 panel c shows the evolution of the eigenvalue as a function of the normalized frequency for the spatial configuration of the red points in panels a and b. Whereas the simple structure shows a low quality factor resonance near $\Omega a = 0.239$, the mirror-symmetric structure presents a sharper resonance with high quality factor, and the minimum is two orders of magnitude smaller than the simpler case.

4.6 Cut-and-project vs circular projection

The modulation applied to the cluster of resonators all over the chapter does not belong to one of the classic algorithms for creating quasicrystals. Some of them (cut-and-project method, substitution sequences, circle map sequences) are explained in chapter 4 in [14]. However, the modulation applied here does not belong to the quasicrystal realm, but, according to Janot [102], it belongs to the so-called modulated crystals. Modulated crystals can also produce incommensurate systems. Nevertheless, there are subtle differences between these two types of structures: while quasicrystals might be seen as projections of finite atomic surfaces from a periodic arrangement in a higher dimensional space into a

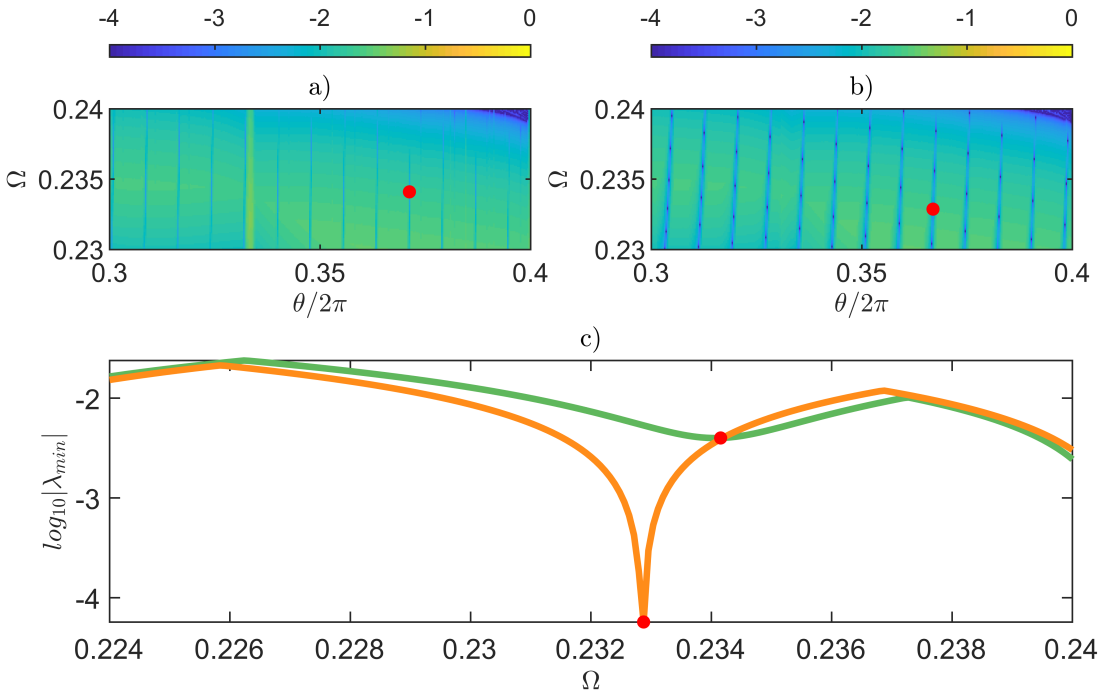

Figure 4.7: Two resonances found in one of the butterfly wings for a one-dimensional array of scatterers (**a**) and for a one-dimensional array of scatterers with mirror symmetry (**b**). Panel **c** depicts the evolution of the minimum eigenvalue as a function of the normalized frequency for both structures with a given spatial configuration.

lower one by means of an irrational slope hyperplane, modulated crystals can be imagined as cuts of infinite atomic surfaces in a synthetic phase space into the physical space by a hyperplane at any direction.

Figure 4.8 illustrates the two formation mechanisms and its differences. Modulated crystals present an underlying periodicity in the physical space, as they are formed by perturbation of a periodic lattice. Thus, their diffraction pattern is different: modulated crystals will preserve the "fundamental reflections" coming from the underneath periodic lattice. Recalling the definition of the spatial positions of our scatterers in equation (4.1), its diffraction pattern is expressed as

$$F(k) = \sum_q J_q(k\rho_m) \sum_p \delta(ka - q\theta + 2p\pi), \tag{4.9}$$

where $J_q(k\rho_m)$ is the weighting factor of the Bragg peaks in the spectrum, $2p\pi$ are the reciprocal modes of the underlying periodic lattice, or "fundamental reflections" of the distribution, and $q\theta$ are the reciprocal modes coming from the irrational modulation, also called "satellite reflections". In contrast, for a Fibonacci sequence, the position of the resonators can be written as

$$R_\alpha = a\alpha + \frac{a}{\tau}\lfloor(\alpha+1)/\tau\rfloor, \tag{4.10}$$

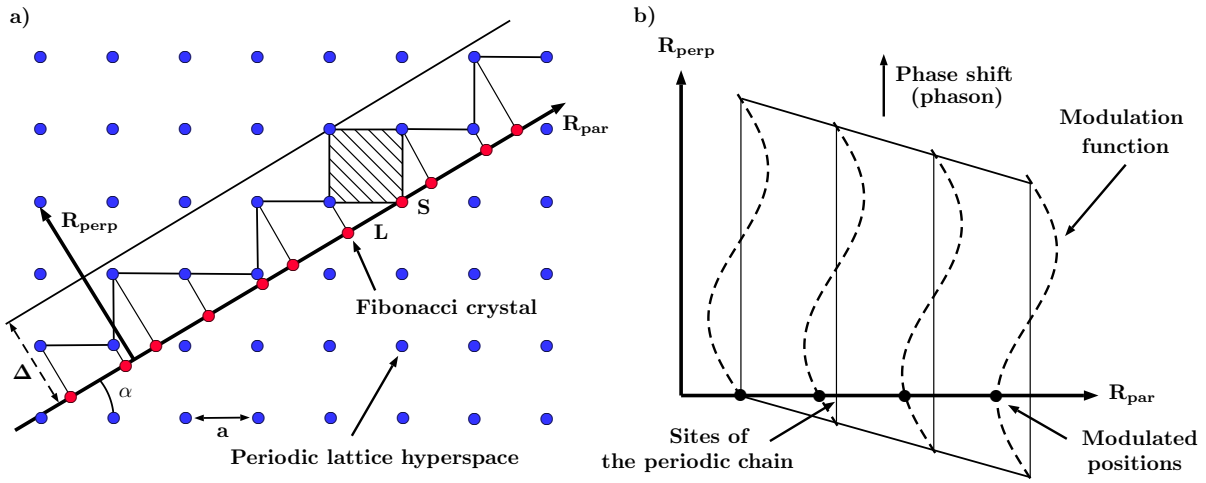

Figure 4.8: **a)** Cut-and-project method from a two-dimensional periodic crystal into a one-dimensional Fibonacci crystal. The slope of the R_{par} axis must be irrational with respect to the lattice directions in the higher dimension. **b)** Modulated crystal seen as a projection in a synthetic phase space.

being $\tau = (1 + \sqrt{5})/2)$ the golden ratio and $\lfloor x \rfloor$ the integer part of x. The diffraction pattern in this case is given by

$$F(k) = \sum_{h,h'} F_{hh'} \delta(k - Q_{hh'}) \tag{4.11}$$

where

$$F_{hh'} = \frac{\sin\left(\frac{\pi\tau}{\tau^2+1}\right)(\tau h' - h)}{\frac{\pi\tau}{\tau^2+1}(\tau h' - h)} e^{i\pi\frac{\tau-2}{\tau+2}(\tau h' - h)} \tag{4.12}$$

is the weighting factor of the Bragg peaks in the spectrum, and

$$Q_{h,h'} = \frac{2\pi\tau^2}{\tau^2+1}(h + h'/\tau) \tag{4.13}$$

are the reciprocal modes. It can be seen that in the case of the modulated crystal, the reciprocal modes are divided into two subsets, while in the case of the Fibonacci series these two subsets are indistinguishable. These two diffraction patterns cover uniformly and densely the spectrum. The dispersion relation of a quasicrystal is a hard problem to solve and yet the solution has not been found. However, all the differences between modulated crystals and quasicrystals are smeared out when working with one-dimensional models. The Fibonacci chain is equivalent to a periodic chain modulated by a function with period τ times as large as that of the basis chain [102].

4.7 Conclusion

This chapter has shown the localisation properties offered by quasi-periodic linear arrangement of scatterers in two dimensions (elastic thin plates). The methods used all along the chapter allow us to get

rid off the super-cell methods that artificially introduce artifacts into the results, and sometimes are not easy to identify. We have also shown how our system preserves the Hofstadter's butterfly feature when mapping its spectrum as a function of the modulation parameter.

Due to the fact that we are analysing a finite system and not and infinite crystal, some edge states appear inside the wings of the butterfly. Those edge states are the localized modes that, according to the theory beneath modulated crystals and almost Mathieu operators, are topologically protected. The quasi-periodic patterns supporting interface states might be enhanced when the clusters are merged with their mirror-symmetric version. Robustness of edge and interface states has been checked numerically, showing that the energy of the field remains localized and their frequency barely suffers from a slight shift when the structure gets distorted.

This structure offers a major advantage; the bound state is not surrounded by the bulk material. In fact, it is a zero-dimensional mode that has been induced by a one-dimensional material in a two-dimensional space. Thus, this geometry is suitable for applications in which these modes are expected to be excited, such as surface acoustic wave sensors. One may think that this structure does not offer complexity or versatility, as the confinement is always found at the edge of the system or at the centre. Nonetheless, taking a look at [94, 96] we can see that this platform offers a mechanism called phason or phase modulation that allows us to move the confined energy of the mode all along the cluster.

Chapter 5

Bound states in the continuum in circular clusters of scatterers

5.1 Introduction

Bound states in the Continuum (BICs) are waves whose energy lies in the radiation part of the spectrum, but its field distribution is localized in a finite part of the system with an infinite lifetime. Firstly proposed and theoretically predicted in 1929 by von Neumann and Wigner [23] as a solution for a single-particle Schrödinger equation, the concept transcended this field of knowledge and was also applied to classical waves, like acoustics [103–107], microwaves [108, 109] or optics [110–112].

The realization and measurement of BICs is still a challenging problem; systems designed to support BICs present sharp resonances with extremely high-quality factors. However, they cannot be directly measured without destroying its exceptional properties. Therefore, structures based on them have the advantage of being accessible from the outside with radiative fields and yet keeping a high quality factor resonance. Also named quasi-BICs (or QBICs), these modes have been widely used in sensing applications [113–115]. Latterly, different structures have been analyzed in order to get high-Q resonances, such as subwavelength gratings [116–119], coupled gratings [113, 120], or photonic crystal slabs [121–125], even in conjunction with more intricate configurations [126].

A myriad of geometries and structures have been explored in order to find BICs [35]. Specially, those based on finite structures are interesting for practical applications, as they get rid of the finite-size effects that appear when trying to implement periodic or waveguide BICs. This is the case of circular clusters of scatterers. This geometry has been studied recently [115, 127–129], showing its suitability for real experiments and applications. This chapter is devoted to the study of this kind of structures and their relation to BICs, proposing a method for designing QBICs in circular clusters of resonators for flexural waves in thin elastic plates.

The chapter is organized as follows: after this introduction, section 5.2 discusses on the formation of BICs in open systems by attaching a cluster of mass-spring resonators to a thin elastic plate. It is

found that when the scatterers in the cluster are arranged in the corners of a regular polygon, a mode with extremely high quality factor can be achieved, and a derivation in the limit when the number of attachments tends to infinite is done, proving that a BIC is obtained for an infinitely thin ring. Section 5.3 continues this last statement and derives an expression for the scattering field of a ring, finding indeed the conditions for the trapped modes. Section 5.4 studies the behavior of the resonance in the case of a finite amount of scatterers, showing that the quality factor gets quickly increased with the number of scatterers. After that, section 5.5 explains some numerical simulations in which the cluster of resonators have been perturbed, in order to check the robustness of these modes. Finally, 5.6 evaluates the possibility of exciting the resonances from the far field, which is in contradiction from what it is known about BICs.

5.2 Eigenmodes of a polygon cluster of scatterers

In this section the possibility of having a BIC for flexural waves in thin elastic plates when a set of resonators is attached to the top surface of the plane forming a circle is going to be analysed. The inhomogeneous Kirchhoff equation describing the motion of the plate for the out-of-plane displacement was established in equation (2.83). In section (2.5), the resonator's strength (t_α) was defined considering spring-mass properties, so this quantity presents a resonance, implying that depending both on frequency and on the spring-mass constants, its value can cover all the domain of real numbers. Taking this into account, in this chapter it will be assumed that the resonator's strength can take any real value ($t_\alpha \in \mathbb{R}$).

Eigenmodes of a system of scatterers attached to a thin elastic plate can be evaluated by means of the MST matrix $M_{\alpha\beta}$, as explained in chapter 2 section 2.6. They can be found by assuming that there is no incident field ($w_0(\boldsymbol{R}_\alpha) = 0$ in equation (2.91)) to the system, and even though a scattered field by all the particles is obtained ($w_e(\boldsymbol{R}_\alpha) \neq 0$). Under these conditions, equation (2.91) becomes a homogeneous system with non-trivial solutions for those frequencies satisfying

$$det(M(\omega)) = 0. \tag{5.1}$$

In the case of thin plates with a finite number of scatterers attached to them, this above condition is satisfied only when ω is a complex number. The imaginary frequency component is inversely related to the quality factor of the resonance achieved. Then, when the imaginary frequency term is extraordinarily small, the found state is called a quasi-BIC, and it is called BIC if this imaginary component is cancelled.

Let us imagine that we have a set N resonators attached to a thin plate such that they all have the same impedance t_0 and they are regularly arranged in a circle of radius R_0. The scatterer α can be located at a distance R_0 from the origin and an angular position $2\pi\alpha/N$. The Hamiltonian describing the system commutes with the rotation operator R_N. Indeed, the M matrix is a circulant matrix [1]. The eigenvalues of a circulant matrix are given by

$$\lambda_\ell = c_0 + c_{n-1}d^\ell + c_{n-2}d^{2\ell} + ... + c_1\omega^{(n-1)\ell},\ \ell = 1, 2, ..., N, \tag{5.2}$$

[1] A circulant matrix is a square matrix in which all row vectors are composed of the same elements and each row vector is rotated one element to the right relative to the preceding row vector.

where c_n are the different terms of the matrix, and $d = exp(2\pi i/N)$. In the case of our matrix, $c_0 = 1$, $c_n = t_\alpha G(\boldsymbol{R}_{\alpha\beta})$. By picking the first row,

$$\lambda_\ell = \left(1 - \sum_{\beta=1}^{N} G(\boldsymbol{R}_{0\beta}) e^{2\pi i \ell \beta/N}\right). \tag{5.3}$$

The determinant of the matrix is the product of its eigenvalues ($det(M) = \prod_{ell=1}^{N} \lambda_\ell$). Therefore, we will chose a given eigenvalue and we will try to make it zero. The eigenvector for a given eigenvalue is

$$v_\ell = \frac{1}{\sqrt{N}} \left(1, d^\ell, d^{2\ell}, \ldots, d^{(n-1)\ell}\right), \ \ell = 1, 2, \ldots, N, \tag{5.4}$$

thus implying a relationship between the coefficients of the form [127]

$$B_\alpha^\ell = e^{2i\pi\ell\alpha/N} B_0^\ell. \tag{5.5}$$

The superscript ℓ indicates that these scattering coefficients are obtained when the ℓ-th eigenvalue is cancelled. The Green's function is going to be redefined as

$$G(\boldsymbol{r}) \equiv i g_0 \xi(\boldsymbol{r}), \tag{5.6}$$

where

$$g_0 = \frac{1}{8k^2} \tag{5.7}$$

and

$$\xi(\boldsymbol{r}) = H_0(k_0 r) + \frac{2i}{\pi} K_0(k_0 r), \tag{5.8}$$

so that $\xi(\boldsymbol{0}) = 1$ and $\gamma_0 = t_0 g_0$ is a real quantity. Equation (5.3) is written now

$$1 - i\gamma_0 \sum_{\beta=1}^{N} \xi(\boldsymbol{R}_\beta) e^{2i\pi\ell\beta/N} = 0. \tag{5.9}$$

This is the necessary condition for achieving the cancellation of the determinant of the M matrix. From this equation, a complex free-space wavenumber k_0^n can be obtained, and the eigenfrequencies ω_n are retrieved by means of the plate's dispersion relation. The imaginary part of these eigenfrequencies is related with the quality factor of the mode. Then, a BIC will be found only when k_0^n is a real quantity. The summation term in the previous equation can be split in its real and imaginary part

$$S^\ell = \sum_{\beta=1}^{N} \xi(\boldsymbol{R}_\beta) e^{2i\pi\ell\beta/N} = S_R^\ell + i S_I^\ell, \tag{5.10}$$

dividing equation (5.9) in two different conditions

$$S_R^{\ell}(k_0) = 0 \tag{5.11}$$

$$1 + \gamma_0 S_I^{\ell}(k_0) = 0. \tag{5.12}$$

Remember that, as explained before, the resonators' strength (t_0) is considered here to be able to take any real value. Therefore, γ_0 can also take any real value, and thus condition (5.12) can always be accomplished. On the other hand, condition (5.11) has to be carefully analysed:

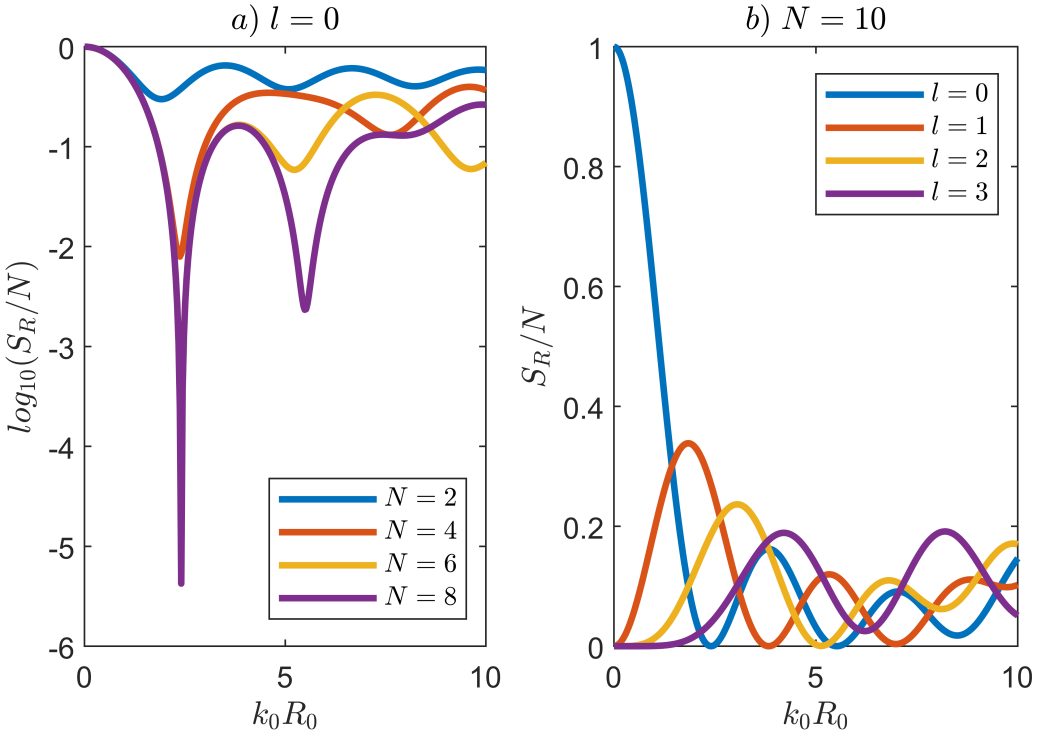

Figure 5.1: S_R under different scenarios. The BIC condition is fulfilled if equation (5.11) is satisfied, that is to say, when S_R is zero. Panel **a** shows the evolution of S_R in frequency for the same resonance $\ell = 0$ and different number of resonators in the cluster. In panel **b** the evolution with frequency of S_R is evaluated for different resonances keeping the number of scatterers in the system ($N = 10$).

Figure 5.1, panel a, shows the evolution of S_R^{ℓ} as a function of k_0R_0 for $\ell = 0$ and for different numbers of scatterers in the cluster. The S_R^{ℓ} is represented in logarithmic scale for the sake of reader's clarity. It can be seen that, when N is small, S_R^{ℓ} does not cancel out; implying that no BIC can be achieved. Despite this, whenever N increases (and not enormous clusters are necessary), the function quickly approaches its cancellation at some given points in the frequency axis. The closer this graph tends to $-\infty$ the higher is the quality factor of the designed resonance. In panel b, the number of scatterers is fixed ($N = 10$) and different resonant indexes are shown. Not logarithmic scale is needed this time to see the effect of changing ℓ: the position in frequency for the minima of the S_R^{ℓ} functions is shifted, that is to say, for the same cluster (same number of scatterers and same radius R_0), two resonances will never

share the same frequency. Furthermore, when ℓ increases keeping the number of scatterers, the minima of S_R^ℓ are higher than for low ℓ, i.e, the quality factor of the resonance will be lower for higher ℓ. This is the case for $\ell = 3$ in Fig. 5.1 panel b; the minimum of the function is actually far from zero. Even if the minima approach zero as the number of scatterers in the cluster is increased, the zero value is reached only in the limit $N \to \infty$ (see the demonstration in Appendix A)

$$\lim_{N\to\infty} \frac{1}{N} S_R^\ell = J_\ell^2(k_0 R_0). \tag{5.13}$$

As a consequence, the resonances are given by the zeros of the Bessel function $J_\ell(k_0 R_0)$ in this limit, reaching the BIC condition, although clusters with $N > 10$ already show high quality resonances, being then quasi-BIC modes. The frequency at which resonances occur is independent on the number of particles (except for cases with very low number of scatterers). Even though, the corresponding resonator impedance γ_0 has to be obtained from the second BIC condition in equation (5.12), which is dependent on the number of scatterers N.

5.3 Eigenmodes of an infinitely thin ring scatterer

Following chapter 2 in [130] on MST for flexural waves in thin elastic plates, a set of point-like scatterers might be seen as an effective material (inclusion) with the following T matrix:

$$T_{qs}^{HJ} = \frac{i}{8k_b^2} \sum_{\alpha\beta} J_q(k_b R_\alpha) e^{-iq\theta_\alpha} T_\alpha M_{\alpha\beta}^{-1} J_s(k_b R_\beta) e^{is\theta_\beta} \tag{5.14}$$

$$T_{qs}^{HI} = \frac{i}{8k_b^2} \sum_{\alpha\beta} J_q(k_b R_\alpha) e^{-iq\theta_\alpha} T_\alpha M_{\alpha\beta}^{-1} I_s(k_b R_\beta) e^{is\theta_\beta} \tag{5.15}$$

$$T_{qs}^{KJ} = \frac{i}{8k_b^2} \sum_{\alpha\beta} I_q(k_b R_\alpha) e^{-iq\theta_\alpha} T_\alpha M_{\alpha\beta}^{-1} J_s(k_b R_\beta) e^{is\theta_\beta} \tag{5.16}$$

$$T_{qs}^{KI} = \frac{i}{8k_b^2} \sum_{\alpha\beta} I_q(k_b R_\alpha) e^{-iq\theta_\alpha} T_\alpha M_{\alpha\beta}^{-1} I_s(k_b R_\beta) e^{is\theta_\beta}, \tag{5.17}$$

where the superscripts H, J, I, K make reference to the incident wave functions (Bessel and modified Bessel) and the scattered field (Hankel and modified Hankel functions). We apply here the geometrical conditions of our problem. First, the point-like scatterers are arranged in a circle, so that $|R_\alpha| = R_0$. From these equations, the terms in the summation get largely simplified

$$T_{qs}^{HJ} = \frac{i}{8k_b^2} \sum_{\alpha} J_q(k_b R_0) e^{-iq\theta_\alpha} \sum_{\beta} M_{\alpha\beta}^{-1} J_s(k_b R_0) e^{is\theta_\beta} \tag{5.18}$$

$$T_{qs}^{HI} = \frac{i}{8k_b^2} \sum_{\alpha} J_q(k_b R_0) e^{-iq\theta_\alpha} \sum_{\beta} M_{\alpha\beta}^{-1} I_s(k_b R_0) e^{is\theta_\beta} \tag{5.19}$$

$$T_{qs}^{KJ} = \frac{i}{8k_b^2} \sum_{\alpha} I_q(k_b R_0) e^{-iq\theta_\alpha} \sum_{\beta} M_{\alpha\beta}^{-1} J_s(k_b R_0) e^{is\theta_\beta} \tag{5.20}$$

$$T_{qs}^{KI} = \frac{i}{8k_b^2} \sum_{\alpha} I_q(k_b R_0) e^{-iq\theta_\alpha} \sum_{\beta} M_{\alpha\beta}^{-1} I_s(k_b R_0) e^{is\theta_\beta}. \tag{5.21}$$

What we actually need to solve is the term

$$B_{s\alpha}^{J} = \sum_{\beta} M_{\alpha\beta}^{-1} J_s(kR_\beta) e^{is\theta_\beta}, \tag{5.22}$$

which is the solution for the following system of equations

$$\sum_{\beta} M_{\alpha\beta} B_{s\beta}^{J} = J_s(kR_\alpha) e^{is\theta_\alpha} \tag{5.23}$$

$$M_{\alpha\beta} = \delta_{\alpha\beta} - t_\alpha G(R_\alpha - R_\beta) \tag{5.24}$$

Thus, we have

$$B_{s\alpha}^{J} - t_\alpha \sum_{\beta} G(R_\alpha - R_\beta) B_{s\beta}^{J} = J_s(kR_0) e^{is\theta_\alpha}. \tag{5.25}$$

The above expression shows that, as for the eigenmodes, all the scattering coefficients are related by a phase factor:

$$B_{s\alpha}^{J} = B_{s0}^{J} e^{is\theta_\alpha}, \tag{5.26}$$

then,

$$\left(1 - t_0 \sum_{\beta} G(R_0 - R_\beta) e^{is(\theta_\beta - \theta_0)}\right) B_{s0}^{J} = J_s(kR_0), \tag{5.27}$$

finally,

$$B_{s\alpha}^{J} = \frac{J_s(k_b R_0) e^{is\theta_\alpha}}{1 - \sum_\beta G(R_0 - R_\beta) e^{is(\theta_\beta - \theta_\alpha)}} = \frac{J_s(k_b R_0) e^{is\theta_s}}{\Sigma}. \tag{5.28}$$

The same argument is valid for $B^I_{s\alpha}$. In the limit when $N \to \infty$, the zeros of the denominator are related to the BICs. In this situation, we will call the function in the denominator $F_s(k_b, t_0)$,

$$F_s(k_b, t_0) = 1 - t_0 \int_0^{2\pi} e^{is\theta} G(2k_b R_0 \sin(\theta/2)) d\theta, \tag{5.29}$$

or

$$F_s(k_b, t_0) = 1 - t_0 \int_0^{\pi} \cos(s\theta) G(2k_b R_0 \sin(\theta/2)) d\theta. \tag{5.30}$$

This integral gives the following result (see details in [129]):

$$F_s(k_b, t_0) = 1 - \frac{t_0 \pi}{8k_b^2 R_0^2} \left(-iJ_s^2(k_b R_0) + J_s(k_b R_0) Y_s(k_b R_0) + \frac{2}{\pi} I_s(k_b R_0) K_s(k_b R_0) \right). \tag{5.31}$$

The T-matrix coefficients are

$$T^{HJ}_{qs} = \frac{i}{8k_b^2} \sum_\alpha J_q(k_b R_\alpha) e^{-iq\theta_\alpha} B^J_{s\alpha} \tag{5.32}$$

$$T^{HI}_{qs} = \frac{i}{8k_b^2} \sum_\alpha J_q(k_b R_\alpha) e^{-iq\theta_\alpha} B^I_{s\alpha} \tag{5.33}$$

$$T^{KJ}_{qs} = \frac{i}{8k_b^2} \sum_\alpha I_q(k_b R_\alpha) e^{-iq\theta_\alpha} B^J_{s\alpha} \tag{5.34}$$

$$T^{KI}_{qs} = \frac{i}{8k_b^2} \sum_\alpha I_q(k_b R_\alpha) e^{-iq\theta_\alpha} B^I_{s\alpha}. \tag{5.35}$$

We focus on the first coefficient, but the reasoning is similar for the rest of the coefficients

$$T^{HJ}_{qs} = \frac{i}{8k_b^2} \frac{J_q(k_b R_0) J_s(k_b R_0)}{F_q(k_b, t_0)} \int_0^{2\pi} e^{i(s-q)\theta} d\theta. \tag{5.36}$$

The coefficient is equal to 0 unless $q = s$ (the T-matrix will be diagonal).

$$T^{HJ}_q = \frac{i\pi}{4k_b^2} \frac{J_q^2(k_b R_0)}{F_q(k_b, t_0)} \tag{5.37}$$

The T-matrix coefficients can be written as

$$T^{HJ}_q = \frac{i\pi}{4k_b^2} \frac{J_q^2(k_b R_0)}{F_q(k_b, t_0)} \tag{5.38}$$

$$T^{HI}_q = \frac{i\pi}{4k_b^2} \frac{J_q(k_b R_0) I_q(k_b R_0)}{F_q(k_b, t_0)} \tag{5.39}$$

$$T^{KJ}_q = \frac{i\pi}{4k_b^2} \frac{I_q(k_b R_0) J_q(k_b R_0)}{F_q(k_b, t_0)} \tag{5.40}$$

$$T^{KI}_q = \frac{i\pi}{4k_b^2} \frac{I_q^2(k_b R_0)}{F_q(k_b, t_0)} \tag{5.41}$$

BICs in this system are represented here by the poles of the T-matrix coefficients. Therefore, the different resonances will correspond to the condition $F_q(k_b, t_0) = 0$. This condition is decoupled into two:

$$J_q(k_b R_0) = 0 \tag{5.42}$$

$$I_q(k_b R_0) K_q(k_b R_0) = -\frac{4k_b^2 R_0^2}{t_0} \tag{5.43}$$

We will use the first equation to stablish the frequency at which the resonance is located, and the second one to design the ring's impedance.

5.4 Quality factor

In this section, the quality factor of the design modes is going to be evaluated and discussed. As explained in previous chapters, the quality factor of a resonance can be measured in various ways, equivalent between them. In this work, two approaches are going to be used; the former is the fitting of the resonant shape in the eigenvalue evolution with a Lorentzian shape, or simply computing numerically the central frequency and its FWHM. The latter is by computing the evolution of the minimum eigenvalue in the complex frequency plane, and estimating the amount of imaginary frequency term needed for the complete cancellation of the eigenvalue.

Figure 5.2 panels a, b, c and d show the evolution of the minimum eigenvalue of the $M_{\alpha\beta}$ matrix for resonances going from $\ell = 0$ to $\ell = 3$. On each panel, each colour line represents a circular cluster with different number of resonators. From this graphs, it is seen that the quality factor increases with the number of scatterers. Vertical dashed lines in all panels indicate the predicted frequency at which the resonance should occur when the number of resonators tends to infinite (following the first zero of the Bessel function of the first kind, $j_{\ell,1}$). In the case of $\ell = 0$, all four different clusters show a dip in the eigenvalue function at the exact predicted frequency. However, this is no longer true for higher ℓ. It must be pointed out that the number of resonators in the cluster limits the highest ℓ resonance achievable. In fact, a cluster with N scatterers will present all resonances up to $\ell < N/2$, and then, for ℓ higher than this threshold, the symmetries of the eigenmodes will mimic those with $\ell < N/2$ with mirror symmetry at the threshold value.

Furthermore, when higher ℓ resonances are studied, some resonances start to disappear for smaller clusters. This is the case of $\ell = 2$ (Fig. 5.2 panel c), where only the clusters with $N = 8$ and $N = 10$ scatterers have a resonance at a desired frequency. A cluster with $N = 6$ scatterers should be able to show a $\ell = 2$ resonance, however, as seen in Fig. 5.1 panel b, for a given cluster, those resonances with lower ℓ will have higher quality factor than those with high ℓ. The quality factor of the resonance $\ell = 2$ in a $N = 6$ cluster is not high enough to appear as a dip in the minimum eigenvalue evolution.

Another remarkable feature appears in the $\ell = 3$ case; the resonance is present in the $N = 6$ cluster, while it does not appear for the rest of the clusters. In Fig. 5.4, an $\ell = 3$ mode is shown, with a $\pi/3$

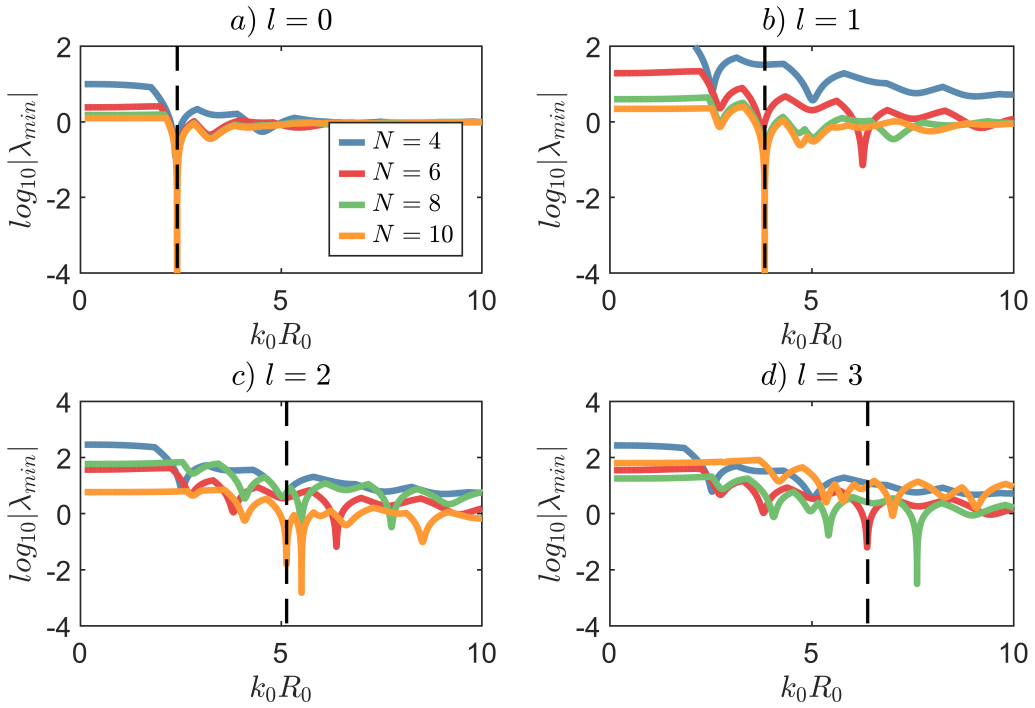

Figure 5.2: Resonance comparison. Panels **a** to **d** show different resonant indices (ℓ), and colour lines represent the evolution of the minimum eigenvalue for clusters with different amount of resonators. Black dashed lines indicate the frequency at which the trapped mode is predicted for the ring.

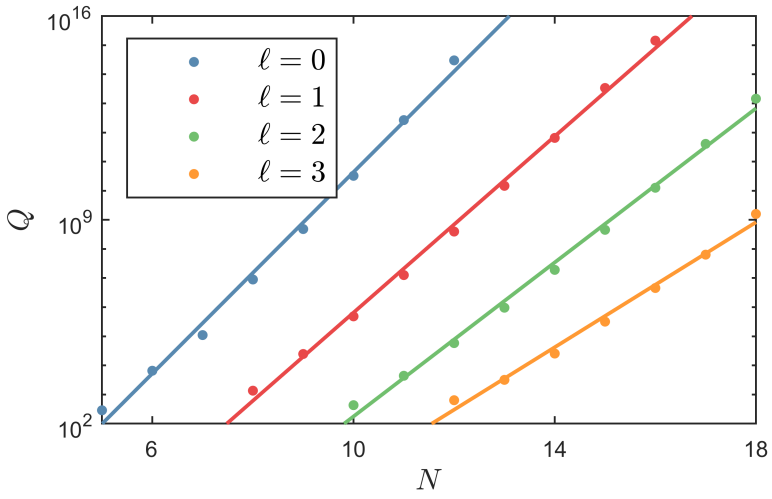

Figure 5.3: Evolution of the quality factor of the resonance with the number of resonators in the cluster for different mode symmetries.

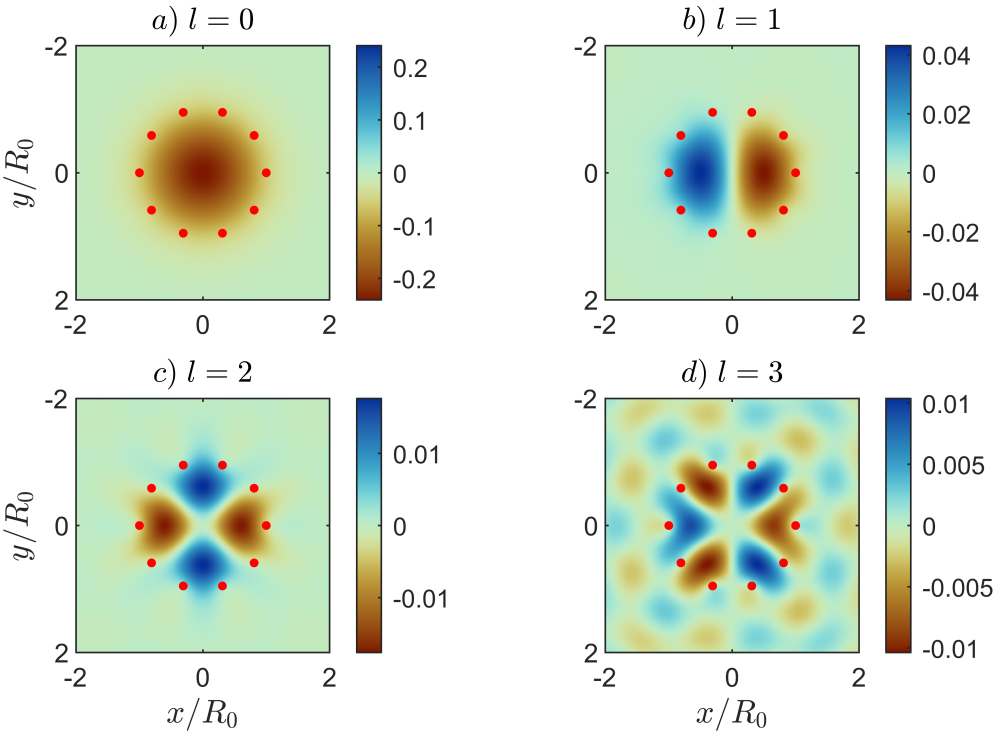

Figure 5.4: Eigenfunction's real part for a $N = 10$ scatterers' cluster. Each panel represents a different ℓ resonance.

symmetry in the inner field. The resonant index ℓ defines the symmetry of the eigenmode inside the circle of scatterers as π/ℓ. Therefore, it is easier for a $N = 6$ cluster to excite the $\ell = 3$ resonance than for a $N = 8$ or $N = 10$ cluster, as the number of scatterers is a multiple of the symmetry of the mode.

The eigenmodes for the cluster with $N = 10$ scatterers can be seen in Fig. 5.4, proving that each ℓ index defines a different symmetry for the field inside the circle of resonators. Moreover, the eigenfunction's distribution of energy is less confined inside the circle for higher ℓ index, restating what it was shown in Fig. 5.1 panel b; for the same amount of scatterers, the quality factor decreases when increasing ℓ. In the case of Fig. 5.4 panel d, the energy of the eigenfunction is leaked outside the cluster, and some field can be appreciated in the outer area.

The qualitative dependence of the quality factor Q of the resonance with the number of resonators N in the cluster and the multipolar order ℓ is summarized in Fig. 5.3. There is an exponential grow of Q with N, and the decrease of Q with the increase of ℓ in the same cluster is also appreciable.

Another interesting phenomena is seen in Fig. 5.5; high index ℓ modes tend to localize in the inner part of the cluster near the scatterers, resulting in the so-called whispering gallery modes. These modes are propagating modes through a curved surface that are commonly related to the radius of curvature of the structure. The approach described here allows therefore for the systematic design of high-quality whispering gallery modes. Figure 5.5 shows some examples of different ℓ modes for the same $N = 50$ cluster (the radius of the cluster is also the same for the four panels). As it can be seen, the localisation

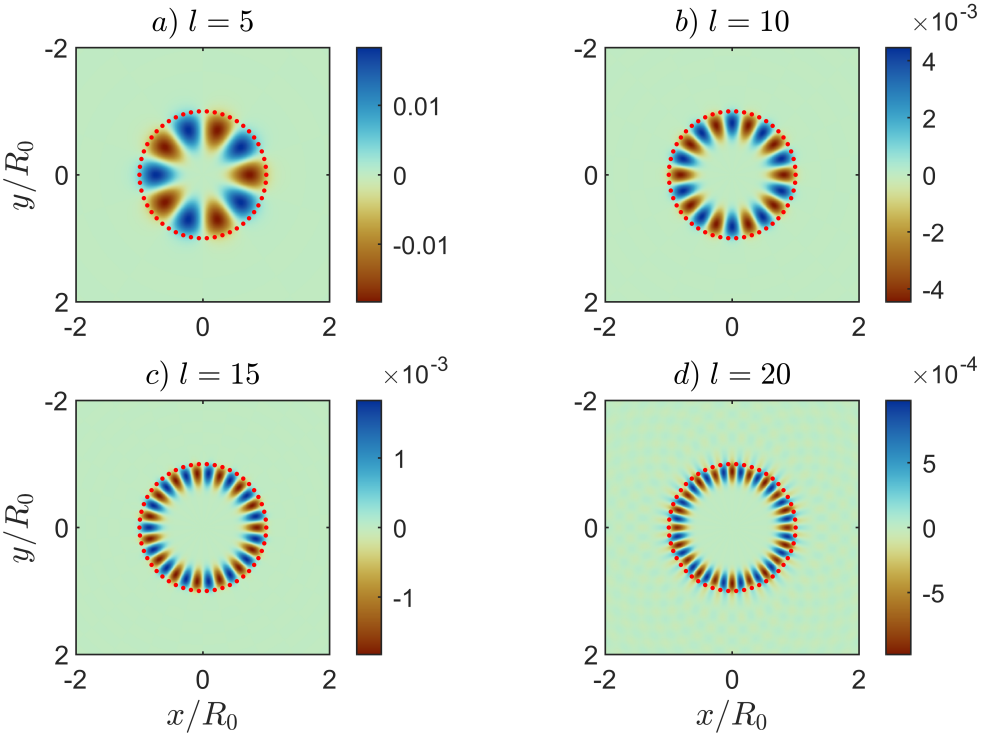

Figure 5.5: Eigenfunction's real part for a $N = 50$ scatterers' cluster. Each panel represents a different ℓ resonance.

of the field near the perimeter of the cluster as ℓ is increased is evident. The field in panel a covers more than half area of the inner circle, while the field in panel d is so confined near the scatterers that most of the area in the inner circle has null field. Furthermore, as explained before, if one takes a look carefully to panel d, he will be able to appreciate some leakage of energy outside the cluster, as happens in Fig. 5.4 panel d.

5.5 Robustness

This section focuses on whether the quasi-BICs designed in the previous sections are robust or they can be easily destroyed when adding some perturbations to the original design. First simulation considers that some resonators in the polygonal arrangement are missing.

Figure 5.6 illustrates this situation. Panel a evaluates the evolution of the minimum eigenvalue of the M matrix in frequency. The original cluster is a $N = 20$ resonators circular cluster and the impedance of the scatterers has been designed to maximize the $\ell = 2$ resonance. Then, one scatterer is removed from the cluster, opening a gap and destroying the symmetry of the structure. The original quality factor of this resonance is $Q = 2583$, remaining the same after removing the first resonator. Which scatterer is removed from the original cluster is seemingly irrelevant; all of them have the same physical properties and the symmetry of the system is broken the same way independently of the deleted resonator, as the

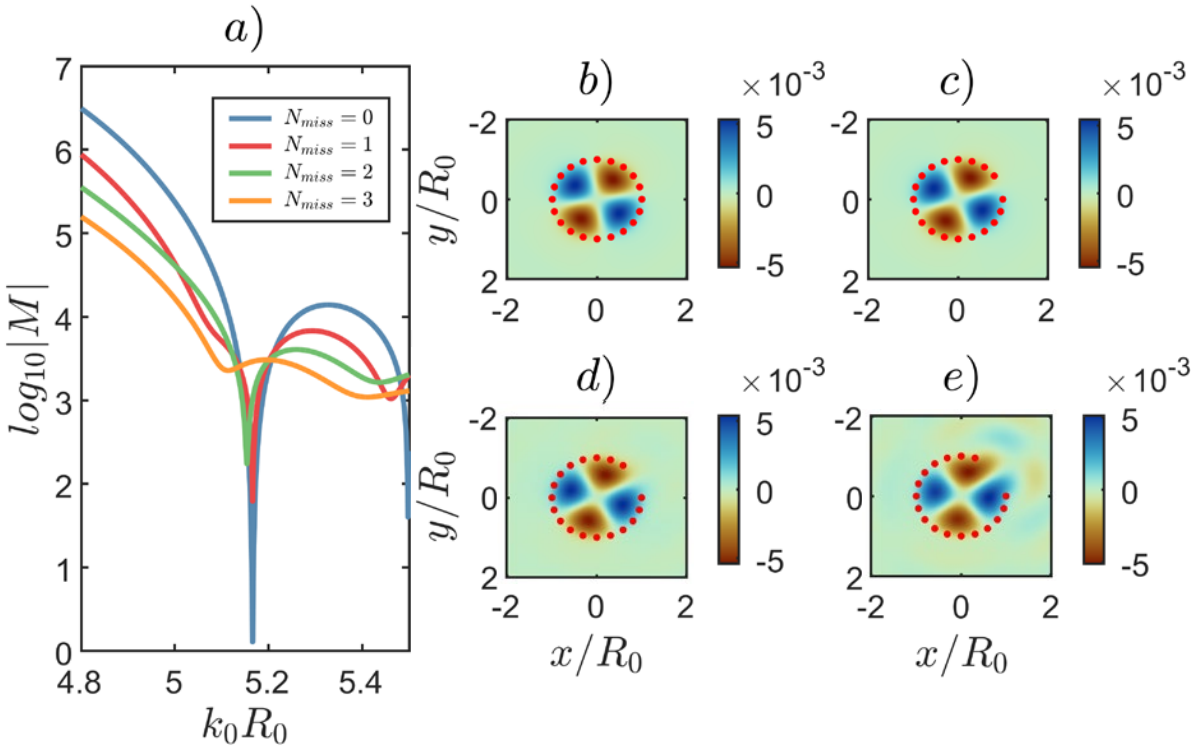

Figure 5.6: $\ell = 2$ resonance destruction as a function of missing resonators in the cluster. Panel **a** represents the evolution of the resonance with frequency for the initial cluster and the missing scatterers' cases. Panels *b* to *e* depict the eigenmodes for the four different scenarios.

propagation of flexural waves through the plate is homogeneous. If another scatterer is removed from the cluster, two different situations can be considered; depending on whether both resonators are adjacent or not. Here, only the second case has been considered, as the gap opened in the original structure is bigger and thus it can be considered that the leakage channel between the inner and the outer part of the cluster is reinforced. The other scenario has many possibilities, depending on the distance between both missing scatterers, their gaps might interfere, changing the shape of the eigenmodes. Green line in Fig. 5.6 panel *a* shows the case with two adjacent resonators missing, and the eigenmode is shown in panel *d*. The quality factor of this resonance is decreased with respect to the original system, being reduced to $Q = 736.3$. Finally, the orange line represents the case where another adjacent resonator has been removed (three in total). In this case, the eigenmode representation panel *e* clearly let us appreciate the leakage of energy from the inside to the outside through the open channel. This last case still has a quality factor of $Q = 60.8$. From those eigenmodes it is clear that the symmetry of the mode is generally preserved, and the field is still localized inside the cluster, but when several scatterers are removed, the leakage becomes stronger, which can also be understood by the broadening of the peak in panel *a*.

From a practical point of view, considering tolerances in manufacturing, it is also interesting to study the quality of the resonances with positional disorder of the scatterers. In the following case, only angular noise has been considered, in the sense that all the scatterers remain at a distance R_0 from the centre of the cluster, but their angular position is changed from the original one, so the scatterers are no longer

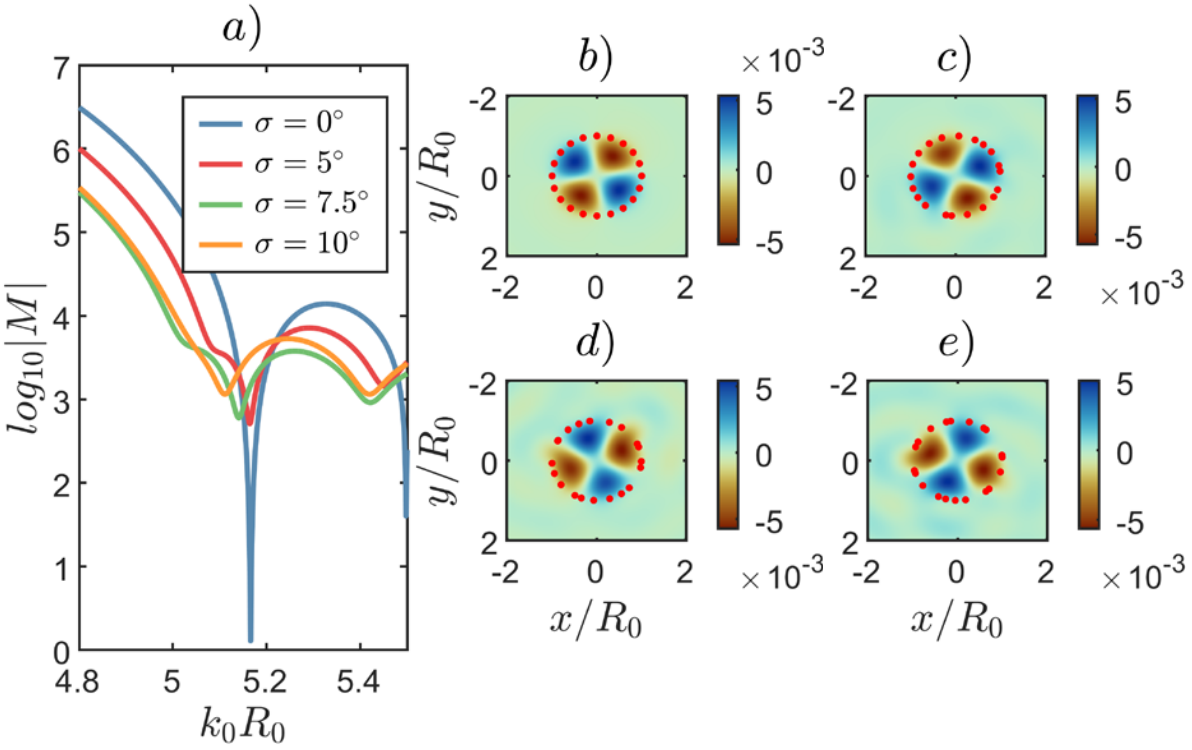

Figure 5.7: $\ell = 2$ resonance destruction as a function of angular noise in the cluster. Panel **a** represents the evolution of the resonance with frequency for the initial cluster and the noisy clusters. Panels *b* to *e* depict the eigenmodes for the four different scenarios.

forming a regular polygon. This angular noise can be described by

$$\theta_\beta = 2\pi\frac{\beta}{N} + \sigma\mathcal{N}(0,1), \tag{5.44}$$

where $\mathcal{N}(0,1)$ is a Gaussian distribution of zero mean and unitary variance, and σ is the variance of the disorder we aim to apply. Figure 5.7 shows the same results as Fig. 5.6 but this time the perturbance is some angular noise added to the original cluster, with variances going from 5° to 10°. As long as the angular noise variance increases, the quality factor of the resonance decreases drastically. Originally the quality factor is the same as in Fig. 5.6, $Q = 2583$. However, after adding a 5° variance angular noise, the quality factor becomes $Q = 258.2$, and it gets further reduced for 7.5° variance ($Q = 135.3$) and even more for 10° variance (77.4).

These results prove that, even if the quality factor of the resonances is strongly sensitive to the perturbation of the cluster, the symmetry of the mode is a robust parameter against disorder. The frequency of the resonance is weakly disturbed, but remains close to the original one.

5.6 Excitation

The excitation of BICs by means of incident plane waves is impossible, since by definition these states are confined in space and do not leak energy to the rest of the system. However, quasi-BICs are no longer limited by this constraint; they can be excited by external fields resulting in strong peaks in the scattering cross section of the cluster. Sensing applications can take advantage of this property. This section tries to explore the possibility of exciting and detecting the modes designed by the method described before.

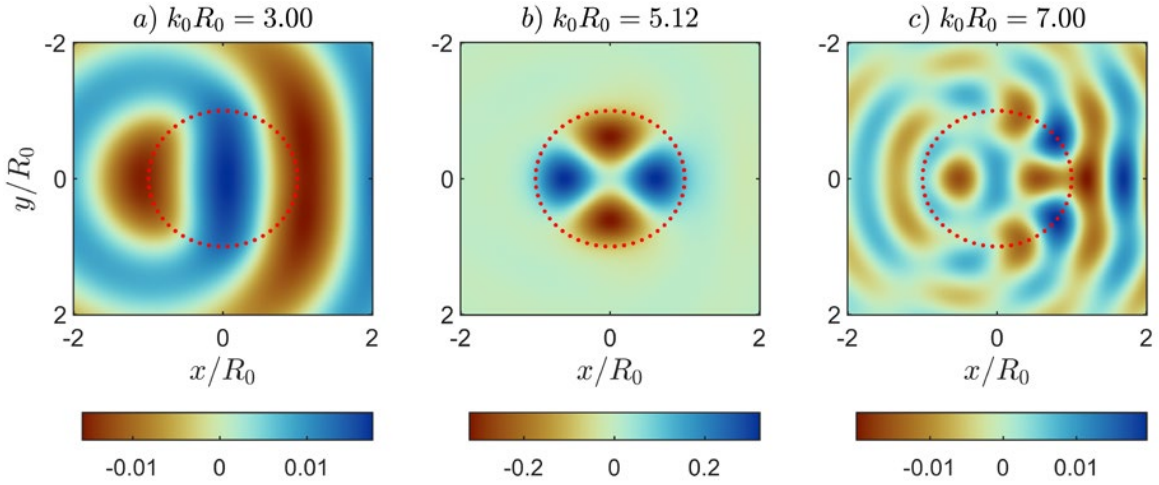

Figure 5.8: Real scattered field for three different frequencies of a $N = 50$ resonators' cluster.

Figure 5.8 shows some scattered fields by a cluster of $N = 50$ resonators under a plane wave incident field with propagation on the x axis. The field has been computed for three different wavenumbers; the designed quasi-BIC is a $\ell = 2$ mode at $k_0R_0 = 5.118$. Thus, while panel b shows the scattering pattern corresponding to the quasi-BIC distribution, the other two panels have completely different patterns, as the wavenumber is not close to the designed resonance. The scattering pattern in panel b shows that, even if there is some energy leakage to the outside of the cluster, most of the energy remains confined inside it.

The analysis of the external excitation of a resonance can be done by means of the far-field pattern radiated by the cluster upon plane wave incidence at frequencies near to the resonance. The far-field radiation pattern is a function of the polar angle θ,

$$f(\theta) = \sum_{\beta=1}^{N} B_\beta e^{-ik_0R_\beta \cos(\theta-\theta_\beta)}, \tag{5.45}$$

and the total scattering cross-section σ_{sca}, which is defined as the ratio of the scattered field flux to the incident field flux [29], is computed as [131]

$$\sigma_{sca} = \frac{1}{16\pi D k_0^2} \int_0^{2\pi} |f(\theta)|^2 d\theta, \tag{5.46}$$

which can be further simplified by using an energy conservation expression related to the optical theorem.

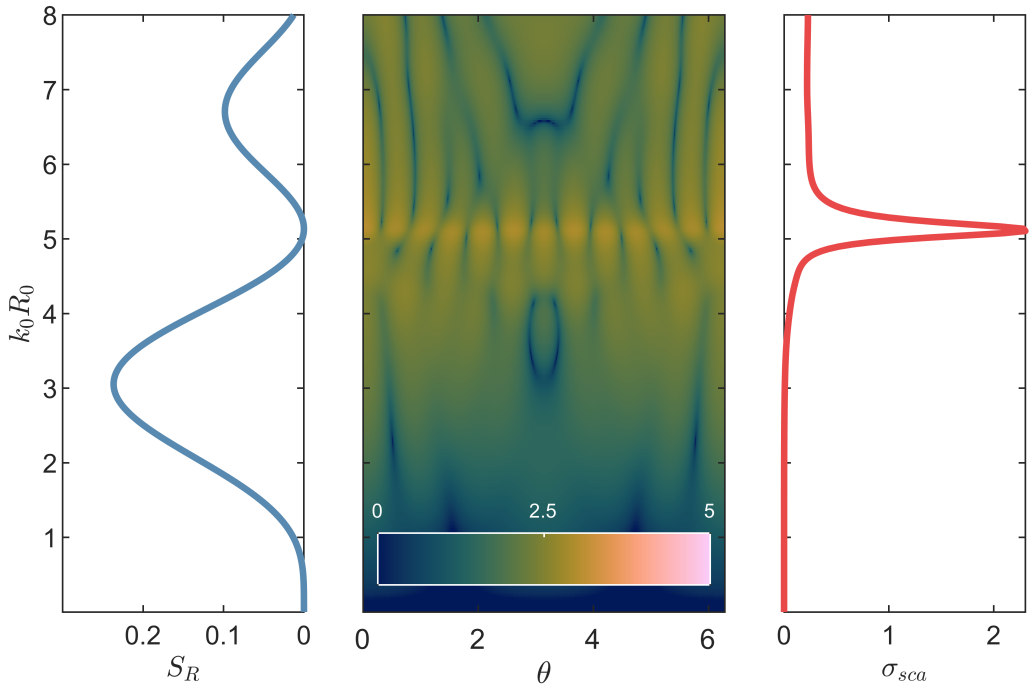

Figure 5.9: From left to right as a function of the frequency: S_R^2 function, far-field radiation pattern $f(\theta)$ and scattering cross-section σ_{sca}. The minimum of the S_R^2 function at $k_0R_0 = 5.118$ coincides with the maximum value of the scattering cross-section.

Figure 5.9 shows the scattered far-field of the cluster as a function of the frequency. Left panel represents the design function S_R^2. Its minimum at $k_0R_0 = 5.118$ indicates the frequency at which the quasi-BIC is supposed to happen. The central panel shows the far-field radiation pattern as a function of the frequency and the polar angle. The symmetry of the radiation pattern does not correspond to that of the quasi-BIC ($\ell = 2$), even at the designed frequency. The reason is that the quasi-BIC field is confined inside the cluster, so that the symmetry can only be observed in the near field, but this field, after interaction with the $N = 50$ scatterers of the cluster, excites some radiation far field with multipolar symmetry. Finally, the right panel shows the scattering cross-section, with an enhancement at the resonant condition, as expected.

5.7 Conclusion

This chapter has studied the possibility of having BICs in circular clusters of scatterers for flexural waves in thin plates. The complete solution for the total confinement of the field has been found to be

the infinitely thin ring. Nevertheless, regular polygons of point-like scatterers are a good platform for achieving high quality multipolar resonances, which might be called quasi-BICs. These modes can be easily designed and predicted via the analytical expression found for the thin ring. Furthermore, it has been proved that these systems are quite robust to positional disorder in the cluster, and, unlike BICs, these resonances can couple to the rest of the system, allowing for the excitation of the mode from the outside of the region where the field is confined.

Chapter 6

Acoustic BIC in a circular cluster of resonators

6.1 Introduction

Introduced and described in the previous chapter, Bound states in the Continuum (BICs) have been the object of study since their prediction in the 1920s. Throughout the 20th century, they have been designed and analyzed, finding different kinds and classifications for them, not only in quantum physics but also in photonics [35, 110–112, 132–134] and acoustics [103–105, 107, 135]. Their infinite Q-factor allows them for being promising candidates for designing filters and resonators for classical waves, as well as enhancing wave-matter interaction [136–139]. Their existence has been proved experimentally both in photonics [140–144] and acoustics [106, 145–148].

However, the main features of a BIC are hard to measure experimentally. They are confined and isolated from the rest of the system, implying that their excitation and measurement without opening an input/output channel and thus leaking some energy is not possible. Therefore, experimental measurements of BICs transform them into QBICs, limiting their quality factor (it will not reach an infinite value any more).

In this chapter we propose the design of an open resonator supporting BICs, and we show its experimental characterization for acoustic waves. The design is based on the geometry explored in Chapter 5; a circular cluster of resonators arranged in a regular polygon. Instead of considering point-like resonators, the theoretical model in this chapter is based on mode matching technique between an acoustic two-dimensional waveguide and the main resonances of blind holes. The theoretical model is completed with some numerical simulations using a Finite Element Method (FEM) software (COMSOL) and a real experiment, proving the existence of the designed resonances. Our design is suitable for the generation of many multipolar modes, that might be foreseen useful for a broad range of applications based on the control of classical waves. Section 6.2 develops the equations that describe the behavior of the BIC. Section 6.3 focuses on designing the parameters for the physical realization of the system. Simulations and experimental results are discussed in section 6.4, and more insight on the quality factor is given in section 6.5. Moreover, experimental results on the robustness of the system are shown in section 6.6.

6.2 BIC design

In this section, equations describing the behaviour of the system will be developed and discussed. Figure 6.1 shows the geometry of the system supporting a BIC, consisting of a cluster of N identical blind holes, with radius R_α and depth L_α. The holes are drilled on the upper surface of an acoustically rigid plate and they are regularly placed along the perimeter of a circumference of radius R_0. A second rigid plate is placed at a distance L from the upper surface of the bottom plate. Thus, the space between both plates can be considered a two-dimensional waveguide for acoustic waves.

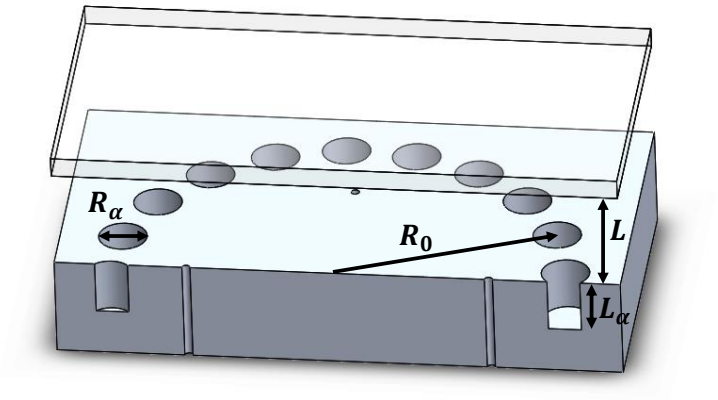

Figure 6.1: Illustration of a section of the plate, with the input channels used for the external excitation and the top plate. The four geometrical parameters that can be tuned in the design of the cluster are indicated in the illustration: the radius of the holes R_α, the radius of the cluster R_0, the depth of the holes L_α and the distance between both rigid plates L.

Let us first assume that we have an infinitely periodic waveguide with a bunch of holes on it. The acoustic field at any position of the unit cell of the waveguide is

$$P(\boldsymbol{r}) = \sum_{\boldsymbol{G}} \left(A_G e^{iq_G z} + B_G e^{-iq_G z} \right) e^{i\boldsymbol{k_G}\cdot\boldsymbol{r}}, \tag{6.1}$$

where $\boldsymbol{G}$ are the modes of the reciprocal lattice, $q_G = \sqrt{\omega^2/c^2 - |\boldsymbol{k_G}|^2}$. A_G and B_G are the incident and reflected coefficients of the wave for a given reciprocal mode. The wall at $z = L$ is considered rigid, so that $\partial P/\partial z = 0$:

$$B_G = A_G e^{i2q_G L}. \tag{6.2}$$

Then, both pressure field and velocity field can be written as

$$P(\boldsymbol{r}) = \sum_{\boldsymbol{G}} A_G \cos\left(q_G(z-L)\right) e^{iq_G L} e^{i\boldsymbol{k_G}\cdot\boldsymbol{r}} \tag{6.3}$$

$$v_n(\boldsymbol{r}) = \sum_{\boldsymbol{G}} \frac{-q_G}{k_b Z_b} 2A_G \sin\left(q_G(z-L)\right) e^{iq_G L} e^{i\boldsymbol{k_G}\cdot\boldsymbol{r}}, \tag{6.4}$$

where z_b is the acoustic impedance of the medium. Concerning the acoustic field inside the holes, only the main resonance of each hole will be considered, and the boundaries with the solid material are considered rigid. Therefore, the pressure field and the normal velocity field inside the hole can be approximated by

$$P_\alpha(\boldsymbol{r}) = e^{i\boldsymbol{k}\boldsymbol{R}_\alpha} B_\alpha \frac{\cos\left(k_b(z-L_\alpha)\right)}{\sin\left(k_b L_\alpha\right)} \tag{6.5}$$

$$v_{n\alpha}(\boldsymbol{r}) = \frac{-e^{-i\boldsymbol{k}\cdot\boldsymbol{R}_\alpha}}{z_b} B_\alpha \frac{\sin\left(k_b(z-L_\alpha)\right)}{\sin\left(k_b L_\alpha\right)}. \tag{6.6}$$

Once the fields in the cavities and the waveguide have been described, mode matching at the top surface of the rigid bottom plate ($z = 0$) is applied in order to match modes from both domains. The mode-matching method is a useful technique for formulation of boundary-value problems, specially for structures consisting of two or more separate regions. It is based on matching the fields at the boundaries of different regions [149]. Two continuity equations will be applied, following [150, 151]; continuity of the pressure field and continuity of the normal velocity field. Then, we will project the modes on both equations to an orthogonal basis of modes (tipically the same basis as the waveguide or the cavity), and finally we will integrate over the domain (the surface of contact in the case of the pressure equation and the whole unit cell in the case of the normal velocity field), allowing us to apply orthogonality of the functions and simplify our system of equations. Two equations are finally obtained:

$$\sum_{\boldsymbol{G}} 2A_G \cos\left(q_G L\right) e^{iq_G L} e^{i\boldsymbol{G}\cdot\boldsymbol{R}_\alpha} H_{\alpha G} = B_\alpha \cot\left(k_b L_\alpha\right) \tag{6.7}$$

and

$$\frac{2q_G}{k_b} A_G \sin\left(q_G L\right) e^{iq_G L} = \sum_{\beta} B_\beta f_\beta e^{-i\boldsymbol{G}\cdot\boldsymbol{R}_\beta} H_{\beta G}, \tag{6.8}$$

where $H_{\alpha G} = \frac{1}{\Omega_\alpha}\int_{\Omega_\alpha} e^{i\boldsymbol{k_G}(\boldsymbol{r}-\boldsymbol{R}_\alpha)} d\Omega_\alpha$ and $f_\alpha = \frac{\Omega_\alpha}{\Omega_C}$ is the cavity's filling fraction, with Ω_c and Ω_α being the areas of the unit cell and the cavity α. After substituting B_G coefficients from equation (6.8) into equation (6.7), we get a system of equations such that:

$$\sum_{\beta=1}^{N} \left[\delta_{\alpha\beta}\cot\left(k_b L_\alpha\right) - \chi_{\alpha\beta}\right] B_\beta = 0, \tag{6.9}$$

where $\chi_{\alpha\beta}$ is

$$\chi_{\alpha\beta} = \sum_{\boldsymbol{G}} \frac{k_b}{q_G} \cot\left(q_G L\right) f_\beta e^{i\boldsymbol{G}\cdot\boldsymbol{R}_{\alpha\beta}} H_{\alpha G} H_{\beta G}. \tag{6.10}$$

$H_{\alpha G}$ can be simplified by assuming that all the holes in the system have the same depth L_α and the same radius R_a. Details on the simplification of the expression can be found in the Appendix B. The final expression is

$$H_G = \frac{2}{R_a|\boldsymbol{k_G}|} J_1(R_a|\boldsymbol{k_G}|). \tag{6.11}$$

Applying equation (6.11) to equation (6.10),

$$\chi_{\alpha\beta} = \sum_{\boldsymbol{G}} \frac{k_b}{q_G} \cot(q_G L) f_\beta e^{i\boldsymbol{G}\cdot\boldsymbol{R}_{\alpha\beta}} \frac{4}{R_a^2|\boldsymbol{k_G}|^2} J_1^2(R_a|\boldsymbol{k_G}|). \tag{6.12}$$

The equation we have been deriving up to this point is valid for a periodic arrangement of circular clusters of holes. Nevertheless, we want to reduce our system to a single circular cluster of holes. Thus, we will extend the length of the unit cell to infinite in both dimensions of the plate. Let us assume that we have a lattice sum of the form

$$S = \frac{1}{\Omega_c} \sum_{\boldsymbol{G}} f(\boldsymbol{K} + \boldsymbol{G}). \tag{6.13}$$

We are interested in the limit in which the unit cell becomes infinite so that we study a finite structure in an open system. In this case, the unit cell is a square unit cell of lattice constant L, therefore the reciprocal lattice vectors are simply

$$\boldsymbol{G} = \frac{2\pi n}{L}\hat{\boldsymbol{x}} + \frac{2\pi m}{L}\hat{\boldsymbol{y}}, \tag{6.14}$$

and the area of the unit cell Ω_c is

$$\Omega_c = L^2. \tag{6.15}$$

Furthermore, the wavevector $\boldsymbol{K}$ can take values only within the Brillouin zone, so that

$$K_x \in [-\pi/L, \pi/L] \tag{6.16}$$

$$K_y \in [-\pi/L, \pi/L]. \tag{6.17}$$

Now we wonder what happens with the sum S in the limit of $L \to \infty$. The first consequence is that, according to the above equations, the Brillouin zone collapses, so that the original wavevector $\boldsymbol{K}$ can only take the value 0. It will disappear from the sum S. However, the sum runs over all possible n and m values in the definition of the reciprocal lattice vector $\boldsymbol{G}$, so that the ratio $2\pi n/L$ and $2\pi m/L$ in this limit becomes a continuous variable. Thus, we can write

$$\boldsymbol{K} + \boldsymbol{G} \to \frac{2\pi n}{L}\hat{\boldsymbol{x}} + \frac{2\pi m}{L}\hat{\boldsymbol{y}} \to k_x\hat{\boldsymbol{x}} + k_y\hat{\boldsymbol{y}} = \boldsymbol{k}. \tag{6.18}$$

This new vector $\boldsymbol{k}$ is not the previous Bloch's wavevector $\boldsymbol{K}$, since this last one has collapsed due to the cancellation of the Brillouin zone. In the lattice sum we have now a continuous variable, however this sum is divided by the area of the unit cell, which is infinite, then we can write

$$\frac{1}{\Omega_c} = \frac{1}{L^2} = \frac{1}{(2\pi)^2}\frac{2\pi}{L}\frac{2\pi}{L} = \frac{1}{(2\pi)^2}dk_x dk_y, \tag{6.19}$$

since, clearly, in the limit $L \to \infty$, $2\pi/L$ is the infinitesimal increment of both k_x and k_y. Then we have

$$\lim_{a\to\infty}\frac{1}{\Omega_c}\sum_{\boldsymbol{G}} f(\boldsymbol{k}+\boldsymbol{G}) = \frac{1}{(2\pi)^2}\int\int f(\boldsymbol{k})d\boldsymbol{k}. \tag{6.20}$$

The sum over the reciprocal modes $\boldsymbol{G}$ is now an integral over $\boldsymbol{k}$. After changing to cylindrical coordinates and applying Graf's addition theorem for Bessel functions J_n (theorem 2.11 in [25]), the following, the following expression is obtained for $\chi_{\alpha\beta}$

$$\chi_{\alpha\beta} = 2\sum_{n=-\infty}^{+\infty}(-1)^n e^{2\pi n i\alpha/N} e^{-2\pi n i\beta/N} I_{cov}(n), \tag{6.21}$$

where

$$I_{cov}(n) = \int_0^{+\infty}\frac{k_b}{q_k k}\cot(q_k L) J_n^2(kR_0) J_1^2(kR_a)dk. \tag{6.22}$$

$I_{cov}(n)$ is always real, as $\cot(ix) = -i\coth(x)$. Due to the symmetry of both the cluster and the operator, the following relation between scattering coefficients B_α can be applied [152, 153]:

$$B_\alpha = e^{2\pi i\ell\alpha/N}B_0, \tag{6.23}$$

with ℓ being the resonant index. One condition is obtained for the design of BICs.

$$\frac{1}{2}\cot(k_b L_\alpha) = \sum_{n=-\infty}^{+\infty}(-1)^n I_{cov}(n)\sum_{\beta=1}^{N} e^{2\pi i\beta(\ell-n)/N}, \tag{6.24}$$

where summation term $\sum_{\beta=1}^{N} e^{2\pi i\beta(\ell-n)/N}$ is equal to N if and only if $n = \ell$, and 0 otherwise. Finally,

$$\cot(k_b L_\alpha) = 2N(-1)^\ell I_{cov}(\ell). \tag{6.25}$$

As $\cot(x)$'s domain is $\mathbb{R}$ and the result of the integral term is a real number, a solution for the equation can always be found, proving that a BIC can be designed. Again, all geometrical dimensions are involved in the solution for the BIC. The resonant index ℓ is also the parameter responsible for the symmetry of the mode. The condition for the existence of a BIC in our system involves all the geometrical parameters (L_α, R_α, L and R_0). Nevertheless, at low frequency, the behaviour of the function inside the integral is governed by the term $J_\ell^2(kR_0)$. Function $J_1^2(kR_\alpha)$ has stronger effect in the high frequency regime. Therefore, R_0 is the main geometrical parameter defining the resonant frequency of the BIC.

6.3 Plate's design

Equation (6.25) is a transcendental equation for the eigenfrequency $\omega = c_b k_b$. Therefore, it is not efficient to first design the geometry of the waveguide and then try to find the frequency at which the BIC appears. Alternately, we can first select the frequency for our BIC, then fix L, R_0 and R_α and, finally obtain L_α by computing $I_\ell(k_b)$ and introducing it into equation (6.25).

There are many variables in this design; we have more degrees of freedom than needed. However, if we want to obtain attainable dimensions for the structure (so that they fit our experimental constraints), a systematic approach for the design of the plate must be followed.

Our chosen approach enabled us to achieve significant control voer the dimensions of the cluster. To begin, we carefully selected the desired frequency for the existence of the BIC, setting it to $f_0 = 5$ kHz for practical experimental considerations. Subsequently, by selecting a symmetry value of $\ell = 2$ for the field, we determined the radius R_0 of the cluster. The radius is chosen such that $k_b R_0$ corresponds to the first zero of the second-order Bessel function, specifically $j_{2,1} = 5.1356$. This choice was motivated by the intention to minimize the field at the cluster's boundary, which in turn would lead to a small value of $I_\ell(k_b)$, and $k_b L_\alpha$ would be close to $\pi/2$, providing a reasonable size for the length L_α. Finally, we get $R_0 = 5.61cm$.

Once the cluster radius has been determined, the selection of the hole radius is established based on certain constraints. The first constraint relates to the maximum allowable size of the hole radius. Considering that the distance between adjacent holes in a circular cluster is $2R_0 \sin(\pi/N)$ [152], it is essential to ensure that the hole radii do not lead to overlapping. Hence, the hole radius is limited to $R_\alpha < R_0 \sin(\pi/N)$. It is worth noting that excessively large hole radii can potentially invalidate the theoretical model employed in this study. The mono-mode approximation used in our equations may not hold for holes with significantly large radii.

The second constraint concerns the minimum allowable size of the hole radius. If the radius is too small, the resulting narrow channels would lead to strong dissipation of the sound wave, resulting in a poor quality of the experimentally observed mode. To address this, we have chosen a hole radius of $R_\alpha = 2/3 R_0 \sin(\pi/N)$, which ensures the desired effect is achieved. By selecting $N = 20$, the calculated value for R_α is 5.9 mm.

For practical reasons, we have selected $L = 2.5cm$, and utilizing equation (6.25), we find $L_\alpha = 1.36$ cm. It is important to mention that the mode-matching method employed here does not fully account for evanescent fields near the hole surfaces. In order to compensate for this limitation, COMSOL simulations have been used to find the exact values for the existence of the BIC.

The BIC condition in equation (6.25) not only reveals that the frequency of the mode can be modified by altering the waveguide's heigh for a given cluster geometry, but also encompasses the scenario where the top of the waveguide is removed, resulting in an open system. In this open configuration, the BIC condition cannot be satisfied, as elaborated upon in Appendix C. Nonetheless, we experimentally characterized this mode to evaluate its quality factor. Both numerical simulations and experimental measurements are provided in the appendix, confirming the presence of the resonance.

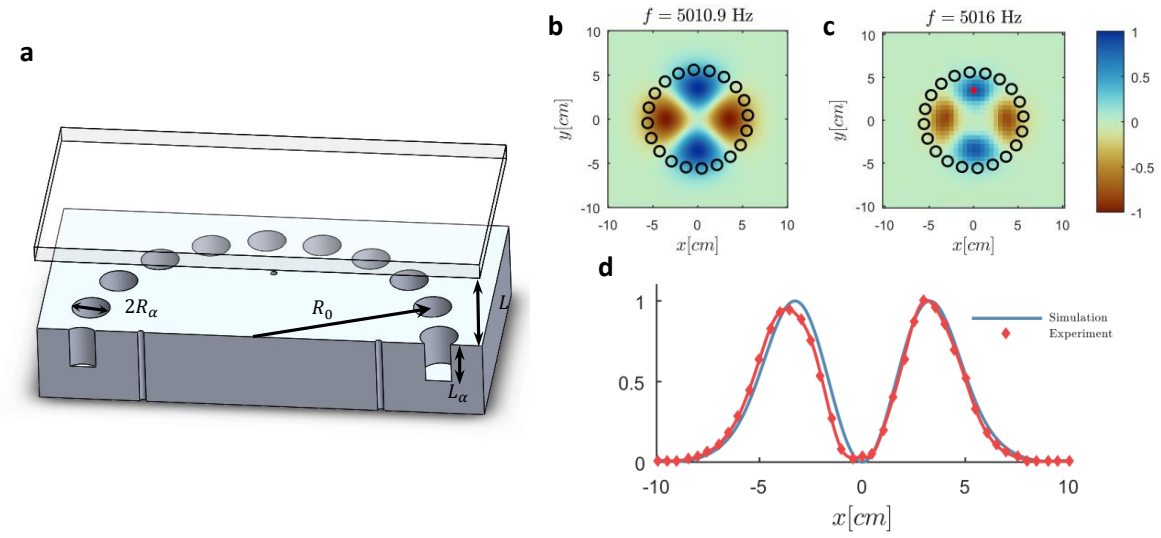

Figure 6.2: Designed BIC and corresponding performance. Panel **a** provides an illustrative depiction of a plate section, featuring its glass cover and input channels. The BIC's normalized real pressure field is displayed in panels **b** and **c**, representing simulation and experiment, respectively. Furthermore, panel **d** exhibits the normalized absolute pressure field along the line $y = 0$, demonstrating a satisfactory level of agreement between the simulation and experimental data.

Regarding the covered case, through meticulous adjustment of the plate's height (L), numerical simulations exhibit agreement with the analytical design, as depicted in panel **b** of Fig. 6.2. As anticipated, the field remains confined within the inner region of the hole cluster, exhibiting the desired symmetry corresponding to the selected multipolar index ℓ.

6.4 Simulation and experiment

Experimental measurements were conducted to characterize the designed structure and validate the existence of a BIC, even if in practice dissipation will influence the measurement and we have created an inlet/outlet channel from the near field. Thus, we acknowledge that the quality factor of the measured mode cannot be infinite. Notably, the experimental results exhibit favorable agreement with the predicted and simulated characteristics. As evidenced in Fig. 6.2, specifically panels **b**, **c**, and **d**, the scattering field at 5016 Hz closely resembles the anticipated BIC distribution obtained from simulations. The excited field remains entirely confined within the circle of radius R_0, with any energy leakage to the exterior being evanescent in nature, implying that these waves outside the circle do not transport energy to the far field. The experimental field displayed in panel **c** is obtained from the real part of the Fourier transform of the field, by selecting the Fourier component which highest amplitude.

Four speakers are oriented upwards and placed under the bottom surface of the aluminum plate. Just on top of them, four 2 mm diameter passing holes are drilled, connecting the upper and lower surfaces of the aluminum plate, thus letting the energy from the speakers enter the cavity. The speakers are driven

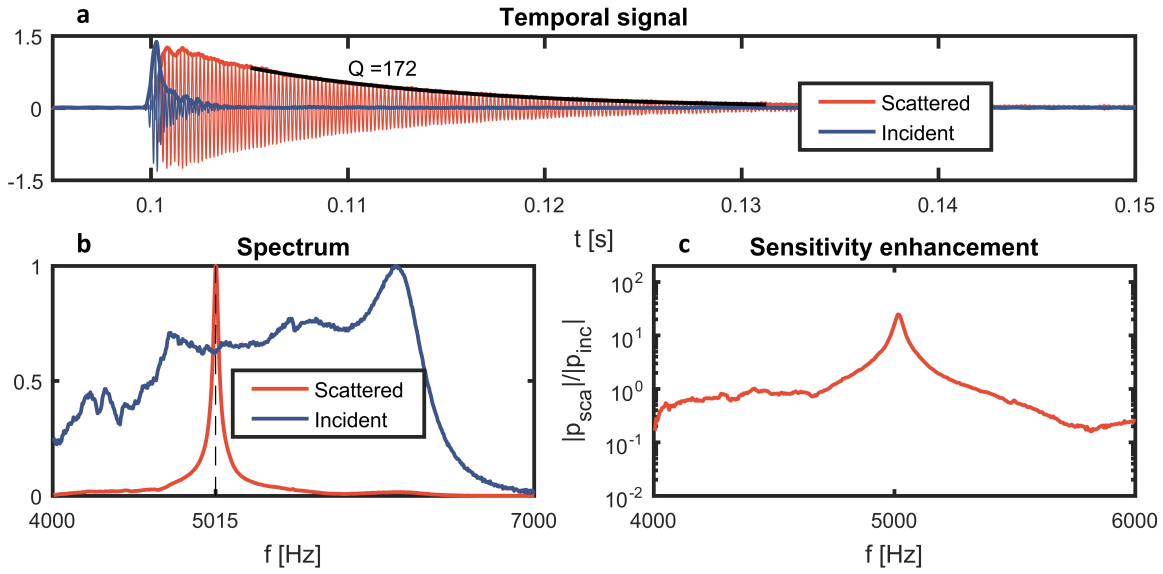

Figure 6.3: Experimental results obtained for the designed plate with $\ell = 2$. Panel **a** showcases the incident and the scattered signals with its envelope at a specific point ($x = 0$, $y = 35$ mm, $z = 22$ mm). The fitting of a decaying exponential curve (represented by the black line) is performed to estimate the quality factor of the resonance. In panel **b**, the spectra of both signals are displayed in normalized units. Panel **c** illustrates the ratio between the scattered spectrum and the input spectrum.

by a Gaussian pulse input signal centered at 5 kHz and spanning a frequency range from 4 kHz to 6 kHz. To measure the incident field, the holes are covered, creating a flat and empty waveguide configuration. Figure 6.3 panel **b** illustrates the incident spectrum at the source point ($x = 0$, $y = 35$ mm, $z = 22$ mm) indicated by a red dot in Fig. 6.2 panel **c**. The spectrum exhibits deviations from a Gaussian shape due to the non-uniform frequency response of the acoustic source caused by the presence of holes in the plate, the speakers, and the cavities behind them.

However, the introduction of the cluster of holes results in a distinct behavior of the scattered field, exhibiting a pronounced resonance at 5016 Hz. Figure 6.3 panel **b** presents the normalized spectra, illustrating the spectral characteristics of the incident and scattered fields. The spectrum of the excited field (blue line) reveals the generation of frequencies other than the central excitation frequency of 5 kHz, although their amplitudes are considerably lower compared to the resonance peak. This interpretation is further supported by the temporal signal depicted in panel **a**. The incident pulse has a duration of less than 5 ms at the measurement position, while the scattered field exhibits a prolonged ringing time of at least 50 ms. The temporal envelope, combined with the narrow spectral content, indicates that the 5 kHz mode is excited and confined within the inner region of the cluster for an extended duration.

The extended ringing time of the scattered field allows for a direct measurement of the quality factor, instead of computing the FWHM. By fitting the temporal curve with a decaying exponential function ($x(t) = Ae^{-\omega_i t}$), the quality factor can be estimated as $Q = \omega_0/2\omega_i$, where ω_0 represents the resonant frequency and ω_i denotes the imaginary frequency term. In the illustrated example shown in Fig. 6.3 panel **a**, the measured quality factor is determined to be 172. It is important to note that the quality

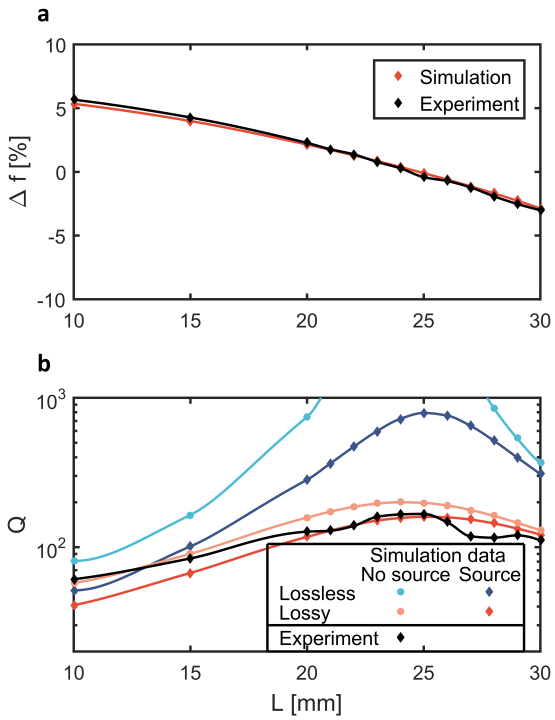

Figure 6.4: **a** Resonant frequency dependence on cavity height. **b** Quality factor variation with covered plate distance. Experimental data are indicated by black rhombus markers, while simulations considering lossy and lossless materials, as well as the presence of the input channels are depicted with another markers.

factor is expected to remain consistent regardless of the measurement position. To verify this, multiple measurements were conducted at various points, confirming the reliability and consistency of the quality factor estimation.

The ratio between the scattered and incident spectrum is presented in Fig. 6.3 panel **c**. A sharp peak is observed around 5 kHz, indicating a significant enhancement in sensitivity, approximately twenty-five times greater than the incident field alone. This distinct characteristic makes our BIC highly attractive for sensing applications. Furthermore, the measured acoustic field at the peak frequency, as depicted in Fig. 6.2 panel **c**, denotes a remarkable level of agreement with the corresponding theoretical prediction, validating the accuracy and effectiveness of our design.

6.5 Quality factor

The structure studied in this chapter possesses is easy to reconfigure. The quality factor of the resonance can be controlled by adjusting the geometry, particularly the height of the cavity (L). Figure 6.4, panel **a**, illustrates the slight variation in the resonant frequency with cavity height, although the quality factor is dependent on that parameter.

Figure 6.4, panel **b**, provides insight into the evolution of the quality factor with respect to the height of the waveguide (L) for the $\ell = 2$ mode. Experimental results are shown in black, showing that the quality factor does not diverge as predicted for a perfect BIC, mainly due to dissipation in the real system. Nonetheless, these experimental findings align with simulations that account for material losses and losses in the excitation system. Simulation results (blue dots) obtained for eigenfrequency simulations without losses in the material or the excitation system reveal that the quality factor exceeds 1000 within the range of $L = 21$ mm to $L = 26$ mm. The range in the figure is limited to 1000 in order to appreciate the shape of the curves once noise is considered in the system. A real eigenvalue, indicating an infinite quality factor, is observed at $L = 24$ mm. On the other hand, simulations considering losses only in the excitation system (blue diamonds) demonstrate that the quality factor remains below 1000 even when there are no losses in the material. The maximum quality factor occurs at $L = 25$ mm ($Q = 792$), which aligns with the behavior expected for BICs, where energy confinement without leakage into the bulk is maintained. In our reciprocal system, energy cannot leak into or out of the BIC, necessitating the creation of input/output channels. In this experiment, the four holes connecting the upper and lower surfaces of the aluminum plate where the speakers are positioned play the role of input/output channels. They enable energy flow from the speakers into the waveguide, exciting the BIC mode. Consequently, there is slight energy leakage from the cluster to the outside through these channels.

In Fig. 6.4 panel **b**, red dots correspond to eigenfrequency simulations considering material loss (introducing an imaginary component to the speed of sound), while neglecting leakage from the excitation system. The maximum observed quality factor in this scenario is lower than in the previous cases, indicating the importance of this loss mechanism, despite the fact that the percentage of losses in air is estimated to be quite low ($0.25\% c_0 = 0.86 m/s$). Moreover, red diamonds represent eigenfrequency simulations accounting for both loss mechanisms. Remarkably, the experimental results align closely with these latter simulations. The measurements were conducted under specific environmental conditions: temperature $T = 21.5°\text{C}$ and relative humidity $RH = 10\%$. According to [154], further reduction in air losses can be achieved by lowering the temperature or increasing the humidity. To explore this, a humidifier was employed near the waveguide, resulting in a measured quality factor of $Q = 182$ at $T = 21.5°\text{C}$ and $RH = 40\%$.

6.6 Robustness

Some tests measuring the robustness of the designed BIC have been performed experimentally. One of the holes in the cluster has been removed by adding a piece of material that covers the whole hole. This material (polylactic acid, PLA) has been considered stiff enough, so that no acoustic field propagates inside the material.

Figure 6.5 panel **a** shows the field distribution of the experimentally measured $\ell = 2$ mode for the original structure (all the holes are present in the cluster). However, the illustration shows one missing hole in the structure. This is the default considered in panel **b**, where different spectra have been depcited. Instead of measuring all the field positions, the effect of the default in the mode has been characterized by measuring the response at the four points indicated in panel **a** by four colour points (orange, red,

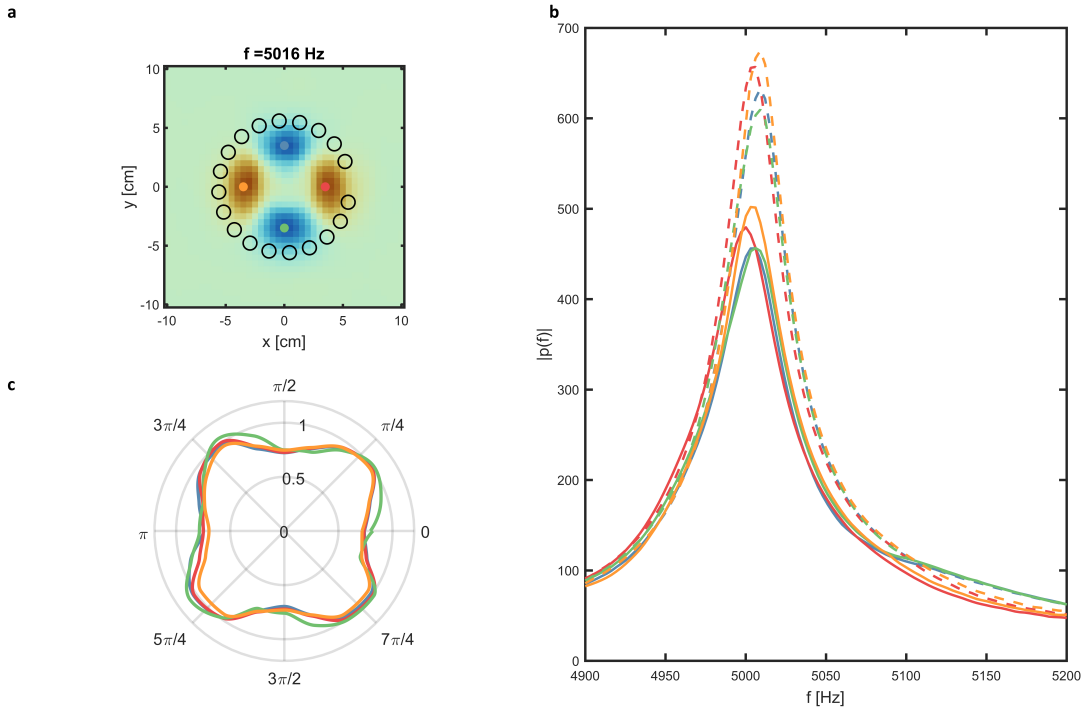

Figure 6.5: Distortion of the BIC when there is a missing hole in the cluster. Panel **a** shows the energy distribution for a $\ell = 2$ mode for the original cluster. There is one missing hole in the picture, indicating its position for results in panel **b**. Colour points (orange, green, blue and red) indicate the position of the measured points for the other panels. Panel **b** represents the spectra of the measured points, both for the original cluster (dotted lines) and for the missing hole scenario (straight lines). Panel **c** shows the ratio between the spectrum coefficient at 5016 Hz (which corresponds to the mode) for the missing hole scenario and the original one. The angle in this graph indicates the position of the missing hole.

green and blue). Dotted lines in panel **b** correspond to the whole structure scenario, where all the holes are present. The spectral response is almost the same for the four measured points. Straight lines show the behaviour of the system when there is a missing hole. The shape of the spectra is almost the same, but there is a clear reduction in the frequency peak. This peak reduction is the chosen parameter for panel **c**; it shows the frequency peak reduction as a function of the position of the missing hole of the cluster. As it can be seen, the peak reduction also presents an $\ell = 2$ symmetry; when the missing hole is placed near a zero pressure point of the original mode, the influence of the default is negligible (so the parameter $|p_{default}|/|p_{original}|$ tends to one). Nevertheless, when the missing hole is near one maximum or minimum of the mode, its influence is higher, and a peak reduction is appreciated. The four colours in the graph represent the four measured positions, having all of them the same behaviour.

Another experiment has been conducted in order to test the robustness of the BIC. In this case, more than one hole has been covered in the structure. The holes are nor removed randomly; instead, it is always deleted one hole adjacent to the last hole removed, such that the opening of the cluster to the rest of the plate increases, as can be seen in Fig. 6.6 panel **a**. Panel **b** shows the temporal evolution of the envelope

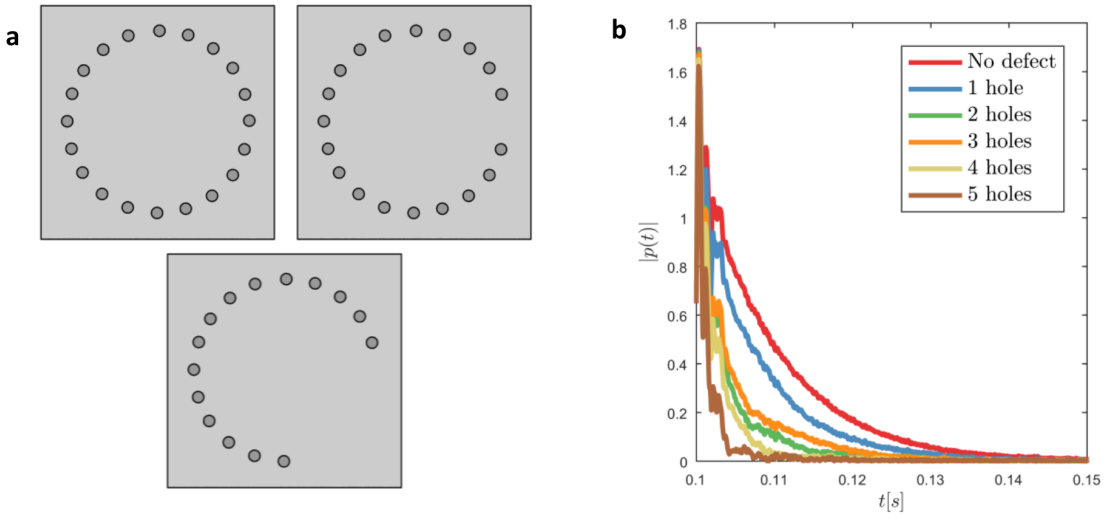

Figure 6.6: Distortion of the BIC when more than one missing hole is missing in the cluster. Illustration **a** shows the picture of the plate for three different cases; the original 20 hole structure, the structure with one missing hole and the cluster with five missing holes. Panel **b** shows the temporal envelope of the signal measured at the point $x = 3.5$ cm, $y = 0$ cm, $z = 2.2$ cm for different scenarios, going from the original design to a 5 hole missing cluster.

of the signal, measured at the same point as for the rest of experimental measurements ($x = 3.5$ cm,$y = 0$ cm,$z = 2..2$ cm). The temporal response becomes shorter when the holes are removed from the structure, indicating a decrease in the quality factor of the mode. The quality factor for the original structure is $Q = 172$. When the first hole is removed, the quality factor gets reduced to $Q = 126$. Recall from Fig. 6.5 panel **c** that the position of the first missing hole is of paramount importance. In this case, the first hole removed is placed at the most critical position, that is to say, the one that presents a bigger reduction of the frequency peak, and thus, of the quality factor. For the rest of scenarios, the quality factors are $Q = 44$, $Q = 61$, $Q = 39$ and $Q = 12$. The quality factor decreases with the number of holes removes (with the exemption of cases 2 and 3).

6.7 Conclusion

In this chapter, we have presented the design and experimental characterization of an acoustic two-dimensional open resonator, proving the existence of a family of BICs within circular arrays of scatterers. Its performance strongly relies on its geometric parameters, allowing it to be tuned numerically. Our approach enables effective confinement of the acoustic field within the circle of scatterers in a two-dimensional waveguide, while also permitting direct measurement of the field inside the waveguide without disrupting the resonance. The experimental measurements align closely with the simulations.

Moreover, out BIC exhibits a significant enhancement of the field amplitude at the resonant frequency. This observed feature reaches magnitudes exceeding one order of magnitude at the BIC frequency.

Notably, the maximum measured quality factor is 182, consistent with the simulation results and in accordance with the inherent loss mechanisms within the system.

The unique properties of our design hold promise for various applications, including enhanced acoustic emissions and the development of acoustic filters and sensors. Additionally, these results extend the previous theoretical demonstrations of BICs in elastic and optical wave systems. Consequently, a properly engineered system based on our design could be used to simultaneously control different wave fields or enhance their interactions, opening new paths for advanced wave manipulation and interdisciplinary studies.

Chapter 7

Concluding remarks

7.1 Conclusions

As suggested by the title *Trapping flexural waves in thin elastic plates by complex engineered surfaces*, the aim of this PhD thesis was to explore the localisation properties of different deterministic arrangements of scatterers on the surface of a thin elastic plate. Three main structures have been developed and analysed over the document: one-dimensional quasicrystals or aperiodic linear arrangements of scatterers, twisted bilayers and BICs.

Twisted bilayer materials exhibit a high density of states due to the abundance of resonators within the structure and their close proximity. They are intricate structures that have lead to many research, offering numerous properties to study. In this thesis, We have tried to elucidate the system's behavior within a specific frequency range, in which the primary driving mechanism is the localisation of states in pairs of resonators (dimerized interaction). The frequency range is determined by the resonator's strength, and our study employs a resonant mass-spring model. Consequently, we always encounter a frequency at which the impedance is sufficiently large for localisation to occur. Localised states manifest in two different scenarios: when the twisting angle is close to zero, resulting in a high concentration of adjacent resonators, and when the twisting angle approximates a commensurate phase of the twisted bilayer, causing certain pairs of scatterers to resonate as dipoles. Additionally, other system parameters have been explored, such as the impedance of the scatterers and the anisotropy of the original lattices.

Quasi-periodic linear arrangements of scatterers in a two-dimensional setting provide localised states of zero dimensionality induced by a one-dimensional configuration. These modulated structures, in which the main properties vary with the modulation parameter, exhibit a distinctive feature known as Hofstadter's butterfly when their spectrum is plotted as a function of the modulation parameter. Through the introduction of a mirror-symmetric variant of the crystal, we have demonstrated a transformation of edge states appearing as a consequence of the finite size of the structure into interface states. This transformation is accompanied by an enhancement in the quality factor of the resonance.

As for the third structure, this PhD thesis delved into the examination of BICs within circular clusters of scatterers, specifically focusing on flexural waves in thin plates. An analytical solution was

successfully derived for the case of a thin ring. Subsequently, the same geometric configuration was adapted to airborne acoustics, leading to the design, fabrication, and experimental measurement of a BIC, yielding outstanding outcomes. Notably, our design possesses a remarkable attribute in its robust resonance, allowing for the incorporation of a measuring device (microphone) without causing complete disruption of the mode. Tipically, BICs are renowned for their high sensitivity and their susceptibility to destruction. However, in our two-dimensional acoustic open resonator, the measured quality factor is at an impressive value of 182 for a 5 kHz mode.

All three structures proposed in this PhD thesis exhibit compelling behaviors that allow them for being promising candidates for applications in wave control. Nevertheless, their different characteristics make them well-suited for distinct purposes. In light of the questions posed in the introductory section of this thesis, let us procede to compare these three structures.

Twisted bilayer's localisation of states arises from the proximity of resonators. Through our investigation, we have proved that the system's behavior within a specific frequency range can be adequately described by the interaction between neighboring pairs of scatterers, while the influence from the remaining resonators is negligible. Consequently, we are observing modes whose wavelength is close to the small distances between resonators, resulting in an overall cluster size much larger than the targeted wavelength (high frequency regime). In contrast, localisation in quasi-periodic linear arrangements of scatterers emerges due to the finite size of the cluster. In infinite quasicrystals, the Hofstadter's butterfly exhibits regions where wave propagation through the crystal is forbidden. However, when the cluster is finite, localised states appear, claimed to possess topological protection. Regarding BICs, the identification of the specific localisation mechanism can be more challenging. These states are achieved through a combination of symmetrical arrangements and/or accidental parametric tuning, effectively suppressing radiation and confining the field in a certain region of space.

Concerning the feasibility of the proposed structures through this document, numerical simulations conducted on twisted bilayers have revealed a lack of robustness against disorder. In fact, even the slightest distortion in the system has the potential to eliminate the localised eigenstates. This poses significant challenges for real-world implementation, given manufacturing tolerances and the precision achievable at nanoscale. Furthermore, when working with finite-sized pillars, it is crutial to consider the limitations arising from overlapping between pillars, which renders certain angles unattainable. One solution to address this issue might involve building one lattice of pillars on the top face of the plate and the other lattice on the bottom face. Withal, this approach would necessitate the formulation of new equations, as the boundary conditions would be different. Quasi-periodic linear arrangements of scatterers show a more favourable response to perturbation. When positional noise is introduced to the cluster, the displacement field remains confined at the edge/interface of the crystal, with only a slight shift observed in the resonance. It is worth noting that, as it happened with twisted bilayer structures, limitations arising from overlapping must be taken into account. BICs within circular arrays of scatterers have also demonstrated resilience against distortion. Not only numerical tests on elastic wave arrangements preserve both the mode shape and the quality factor, but experimental results in acoustics have also confirmed that the resonance remains robust even in the event of the disappearance of holes (resonators) within the system.

Finally, let us comment on the versatility and/or complexity inherent in these structures. Twisted bilayer structures are the most complex among the three systems under investigation. They offer many

different modes that can be tuned and attained, not only by manipulating certain geometrical parameters (which may pose challenges from a manufacturing point of view), but also due to the capacity of a single geometric configuration to hold a high density of localised states (small twisting angles), which is particularly desirable for optical field phase modulation. In the case of quasi-periodic linear arrangement of resonators, the complexity of the field is not the main advantage of this structure. As discussed in the the conclusion of chapter 3, there exists a mechanism for translating confined energy throughout the structure. Nevertheless, this mechanism relies on geometric modulation, and thus lacks the desired level of tunability. On the other hand, BICs within circular arrays of resonators can support a whole family of modes with different symmetries. This structure presents an opportunity for implementing active mechanisms to manipulate the impedances of the resonators, optimizing various symmetries and obtaining different mode shapes. Such an approach holds significant potential for tailored applications.

7.2 Perspectives and future work

Throughout this doctoral thesis, theoretical discussions and numerical simulations have been presented, while no experimental investigations have been conducted thus far (except for the proof of concept in Chapter 6). Structures conceived in this work have been envisioned for utilization as spatial light modulators, enabling precise manipulation of the phase of incident beams and facilitating image recovery through computational imaging techniques. Therefore, the mass-spring resonators would be pillars at the nanoscale attached to the upper surface of the thin elastic plate. To proceed with practical applications, it becomes imperative to characterize the samples. Among the common methods for characterizing mechanical wave propagation at the micro and nanoscale, the pump and probe technique is frequently employed. This is an optical detection technique in which an ultrashort pulsed light beam is split into two parts; one serving as a source for exciting mechanical waves (pump) and the other utilized for scanning the sample (probe). By experimentally confirming the localised wave phenomena demonstrated in simulations, we can progress to the next stage and explore the application of these phenomena.

Future work is not limited to experimental demonstration of the physical phenomena explored here. As discussed in the present document, the resonator model employed in the simulations is an approximation and does not accurately represent real-world structures. Thus, it is necessary to develop a more refined model of the behavior of the pillar, specially for those cases in which Euler-Bernouilli theory is not valid. Moreover,there are further opportunities for investigating the physics of quasicrystals. Even the simplest one-dimensional structures have not been fully comprehended, and a consistent method for obtaining the dispersion relation of a given quasicrystal remains elusive.

Lastly, it is worth considering additional applications for the structures examined in this study. One potential avenue is the utilization of circular arrays of scatterers in microfluidic chambers to generate BICs. By harnessing the sensitivity-enhancing characteristic of these modes, it becomes possible to decrease the power consumption required to induce nonlinear phenomena, such as acoustic radiation force or acoustic streaming. This approach holds promise for optimizing and expanding the functionality of microfluidic systems while capitalizing on the unique properties of BICs.

Finally, it is worth considering additional applications for the structures examined in this study. One potential application is the utilization of BICs within circular arrays of scatterers in microfluidic

chambers. By harnessing the sensitivity enhancement property of these modes, it becomes possible to decrease the power consumption required to induce nonlinear phenomena, such as acoustic radiation force or acoustic streaming. This approach would facilitate the implementation of systems for controlling micro and nanoparticles in microfluidic chambers.

Bibliography

[1] Mihnea Dulea, Magnus Johansson, and Rolf Riklund. Localization of electrons and electromagnetic waves in a deterministic aperiodic system. *Phys. Rev. B*, 45:105–114, Jan 1992.

[2] Kashif Ammar Yasir, Muhammad Ayub, and Farhan Saif. Exponential localization of moving end mirror in optomechanics. *Journal of Modern Optics*, 61(16):1318–1323, 2014.

[3] Matteo Carlesso, Mauro Paternostro, Hendrik Ulbricht, Andrea Vinante, and Angelo Bassi. Non-interferometric test of the continuous spontaneous localization model based on rotational optomechanics. *New Journal of Physics*, 20(8):083022, aug 2018.

[4] T. P. Purdy, D. W. C. Brooks, T. Botter, N. Brahms, Z.-Y. Ma, and D. M. Stamper-Kurn. Tunable cavity optomechanics with ultracold atoms. *Phys. Rev. Lett.*, 105:133602, Sep 2010.

[5] Muhammad Ayub, Kashif Ammar Yasir, and Farhan Saif. Dynamical localization of matter waves in optomechanics. *Laser Physics*, 24(11):115503, oct 2014.

[6] Per Delsing, Andrew N Cleland, Martin J A Schuetz, Johannes Knörzer, Géza Giedke, J Ignacio Cirac, Kartik Srinivasan, Marcelo Wu, Krishna Coimbatore Balram, Christopher Bäuerle, Tristan Meunier, Christopher J B Ford, Paulo V Santos, Edgar Cerda-Méndez, Hailin Wang, Hubert J Krenner, Emeline D S Nysten, Matthias Weiß, Geoff R Nash, Laura Thevenard, Catherine Gourdon, Pauline Rovillain, Max Marangolo, Jean-Yves Duquesne, Gerhard Fischerauer, Werner Ruile, Alexander Reiner, Ben Paschke, Dmytro Denysenko, Dirk Volkmer, Achim Wixforth, Henrik Bruus, Martin Wiklund, Julien Reboud, Jonathan M Cooper, YongQing Fu, Manuel S Brugger, Florian Rehfeldt, and Christoph Westerhausen. The 2019 surface acoustic waves roadmap. *Journal of Physics D: Applied Physics*, 52(35):353001, jul 2019.

[7] Charles M. Reinke and Ihab El-Kady. Phonon-based scalable platform for chip-scale quantum computing. *AIP Advances*, 6(12), 12 2016. 122002.

[8] Alexandru Macridin, Panagiotis Spentzouris, James Amundson, and Roni Harnik. Electron-phonon systems on a universal quantum computer. *Phys. Rev. Lett.*, 121:110504, Sep 2018.

[9] Shi-Liang Zhu, C. Monroe, and L.-M. Duan. Trapped ion quantum computation with transverse phonon modes. *Phys. Rev. Lett.*, 97:050505, Aug 2006.

[10] Nevill F Mott. Metal-insulator transition. *Reviews of Modern Physics*, 40(4):677, 1968.

[11] P. W. Anderson. Absence of diffusion in certain random lattices. *Phys. Rev.*, 109:1492–1505, Mar 1958.

[12] Jean-Pierre Fouque. Diffuse waves in complex media. 2012.

[13] D. Shechtman, I. Blech, D. Gratias, and J. W. Cahn. Metallic phase with long-range orientational order and no translational symmetry. *Phys. Rev. Lett.*, 53:1951–1953, Nov 1984.

[14] Marjorie Senechal. *Quasicrystals and geometry*. CUP Archive, 1996.

[15] Serge Aubry and Gilles André. Analyticity breaking and anderson localization in incommensurate lattices. *Ann. Israel Phys. Soc*, 3(133):18, 1980.

[16] Viktor G Veselago. Electrodynamics of substances with simultaneously negative and. *Usp. fiz. nauk*, 92(7):517, 1967.

[17] J.B. Pendry, A.J. Holden, D.J. Robbins, and W.J. Stewart. Magnetism from conductors and enhanced nonlinear phenomena. *IEEE Transactions on Microwave Theory and Techniques*, 47(11):2075–2084, 1999.

[18] J. B. Pendry. Negative refraction makes a perfect lens. *Phys. Rev. Lett.*, 85:3966–3969, Oct 2000.

[19] Sergei A Tretyakov. A personal view on the origins and developments of the metamaterial concept. *Journal of Optics*, 19(1):013002, dec 2016.

[20] K. S. Novoselov, A. K. Geim, S. V. Morozov, D. Jiang, Y. Zhang, S. V. Dubonos, I. V. Grigorieva, and A. A. Firsov. Electric field effect in atomically thin carbon films. *Science*, 306(5696):666–669, 2004.

[21] Yuan Cao, Valla Fatemi, Shiang Fang, Kenji Watanabe, Takashi Taniguchi, Efthimios Kaxiras, and Pablo Jarillo-Herrero. Unconventional superconductivity in magic-angle graphene superlattices. *Nature*, 556(7699):43–50, 2018.

[22] Yuan Cao, Debanjan Chowdhury, Daniel Rodan-Legrain, Oriol Rubies-Bigorda, Kenji Watanabe, Takashi Taniguchi, T. Senthil, and Pablo Jarillo-Herrero. Strange metal in magic-angle graphene with near planckian dissipation. *Phys. Rev. Lett.*, 124:076801, Feb 2020.

[23] J von Neumann and Eugene P Wigner. Über merkwürdige diskrete eigenwerte. *Phys. Z.*, 30(465), 1929.

[24] Daniel Royer and Eugene Dieulesaint. *Elastic waves in solids I: Free and guided propagation*. Springer Science & Business Media, 1999.

[25] Paul A Martin. *Multiple scattering: interaction of time-harmonic waves with N obstacles*. Number 107. Cambridge University Press, 2006.

[26] AN Norris and C Vemula. Scattering of flexural waves on thin plates. *Journal of sound and vibration*, 181(1):115–125, 1995.

[27] Milton Abramowitz and Irene A Stegun. *Handbook of mathematical functions with formulas, graphs, and mathematical tables*, volume 55. US Government printing office, 1964.

[28] P.A. Martin and Andrew J. Hull. Dynamic response of an infinite thin plate loaded with concentrated masses. *Wave Motion*, 98:102643, 2020.

[29] A.N. Norris and C. Vemula. Scattering of flexural waves on thin plates. *Journal of Sound and Vibration*, 181(1):115–125, 1995.

[30] Yabin Jin, Daniel Torrent, and Bahram Djafari-Rouhani. Robustness of conventional and topologically protected edge states in phononic crystal plates. *Phys. Rev. B*, 98:054307, Aug 2018.

[31] Chun-Wei Chen, Rajesh Chaunsali, Johan Christensen, Georgios Theocharis, and Jinkyu Yang. Corner states in a second-order mechanical topological insulator. *Communications Materials*, 2(1):62, 2021.

[32] Chun-Wei Chen, Natalia Lera, Rajesh Chaunsali, Daniel Torrent, Jose Vicente Alvarez, Jinkyu Yang, Pablo San-Jose, and Johan Christensen. Mechanical analogue of a majorana bound state. *Advanced Materials*, 31(51):1904386, 2019.

[33] Rajesh Chaunsali, Chun-Wei Chen, and Jinkyu Yang. Experimental demonstration of topological waveguiding in elastic plates with local resonators. *New Journal of Physics*, 20(11):113036, nov 2018.

[34] Daniel Torrent, Didier Mayou, and José Sánchez-Dehesa. Elastic analog of graphene: Dirac cones and edge states for flexural waves in thin plates. *Phys. Rev. B*, 87:115143, Mar 2013.

[35] Chia Wei Hsu, Bo Zhen, A Douglas Stone, John D Joannopoulos, and Marin Soljačić. Bound states in the continuum. *Nature Reviews Materials*, 1(9):1–13, 2016.

[36] E. Suárez Morell, J. D. Correa, P. Vargas, M. Pacheco, and Z. Barticevic. Flat bands in slightly twisted bilayer graphene: Tight-binding calculations. *Phys. Rev. B*, 82:121407, Sep 2010.

[37] Rafi Bistritzer and Allan H MacDonald. Moiré bands in twisted double-layer graphene. *Proceedings of the National Academy of Sciences*, 108(30):12233–12237, 2011.

[38] P. San-Jose, J. González, and F. Guinea. Non-abelian gauge potentials in graphene bilayers. *Phys. Rev. Lett.*, 108:216802, May 2012.

[39] J. M. B. Lopes dos Santos, N. M. R. Peres, and A. H. Castro Neto. Graphene bilayer with a twist: Electronic structure. *Phys. Rev. Lett.*, 99:256802, Dec 2007.

[40] JMB Lopes Dos Santos, NMR Peres, and AH Castro Neto. Continuum model of the twisted graphene bilayer. *Physical Review B*, 86(15):155449, 2012.

[41] CR Woods, Liam Britnell, Axel Eckmann, RS Ma, JC Lu, HM Guo, X Lin, GL Yu, Y Cao, Roman V Gorbachev, et al. Commensurate–incommensurate transition in graphene on hexagonal boron nitride. *Nature physics*, 10(6):451–456, 2014.

[42] Yuan Cao, Valla Fatemi, Ahmet Demir, Shiang Fang, Spencer L Tomarken, Jason Y Luo, Javier D Sanchez-Yamagishi, Kenji Watanabe, Takashi Taniguchi, Efthimios Kaxiras, et al. Correlated insulator behaviour at half-filling in magic-angle graphene superlattices. *Nature*, 556(7699):80–84, 2018.

[43] Sung Joon Ahn, Pilkyung Moon, Tae-Hoon Kim, Hyun-Woo Kim, Ha-Chul Shin, Eun Hye Kim, Hyun Woo Cha, Se-Jong Kahng, Philip Kim, Mikito Koshino, Young-Woo Son, Cheol-Woong Yang, and Joung Real Ahn. Dirac electrons in a dodecagonal graphene quasicrystal. *Science*, 361(6404):782–786, 2018.

[44] Ying-Ming Xie, Dmitri K. Efetov, and K. T. Law. φ_0-josephson junction in twisted bilayer graphene induced by a valley-polarized state. *Phys. Rev. Res.*, 5:023029, Apr 2023.

[45] Stephen Carr, Daniel Massatt, Shiang Fang, Paul Cazeaux, Mitchell Luskin, and Efthimios Kaxiras. Twistronics: Manipulating the electronic properties of two-dimensional layered structures through their twist angle. *Phys. Rev. B*, 95:075420, Feb 2017.

[46] Changming Huang, Fangwei Ye, Xianfeng Chen, Yaroslav V Kartashov, Vladimir V Konotop, and Lluis Torner. Localization-delocalization wavepacket transition in pythagorean aperiodic potentials. *Scientific reports*, 6(1):1–8, 2016.

[47] Peng Wang, Yuanlin Zheng, Xianfeng Chen, Changming Huang, Yaroslav V Kartashov, Lluis Torner, Vladimir V Konotop, and Fangwei Ye. Localization and delocalization of light in photonic moiré lattices. *Nature*, 577(7788):42–46, 2020.

[48] Guangwei Hu, Qingdong Ou, Guangyuan Si, Yingjie Wu, Jing Wu, Zhigao Dai, Alex Krasnok, Yarden Mazor, Qing Zhang, Qiaoliang Bao, et al. Topological polaritons and photonic magic angles in twisted α-moo3 bilayers. *Nature*, 582(7811):209–213, 2020.

[49] Haoning Tang, Fan Du, Stephen Carr, Clayton DeVault, Olivia Mello, and Eric Mazur. Modeling the optical properties of twisted bilayer photonic crystals. *Light: Science & Applications*, 10(1):157, 2021.

[50] Jiongchao Zeng, Yanwen Hu, Xin Zhang, Shenhe Fu, Hao Yin, Zhen Li, and Zhenqiang Chen. Localization-to-delocalization transition of light in frequency-tuned photonic moiré lattices. *Opt. Express*, 29(16):25388–25398, Aug 2021.

[51] Ibrahim Nasidi, Ran Hao, Jun Chen, Erping Li, and ShangZhong Jin. Photonic moiré lattice waveguide with a large slow light bandwidth and delay-bandwidth product. *Appl. Opt.*, 61(19):5776–5781, Jul 2022.

[52] Chang-Hwan Yi, Hee Chul Park, and Moon Jip Park. Strong interlayer coupling and stable topological flat bands in twisted bilayer photonic moiré superlattices. *Light: Science & Applications*, 11(1):289, 2022.

[53] Natalia S. Salakhova, Ilia M. Fradkin, Sergey A. Dyakov, and Nikolay A. Gippius. Twist-tunable moiré optical resonances. *Phys. Rev. B*, 107:155402, Apr 2023.

[54] Yabin Jin, Wan Wang, Zhihui Wen, Daniel Torrent, and Bahram Djafari-Rouhani. Topological states in twisted pillared phononic plates. *Extreme Mechanics Letters*, 39:100777, 2020.

[55] María Rosendo López, Fernando Peñaranda, Johan Christensen, and Pablo San-Jose. Flat bands in magic-angle vibrating plates. *Phys. Rev. Lett.*, 125:214301, Nov 2020.

[56] Yuanchen Deng, Mourad Oudich, Nikhil JRK Gerard, Jun Ji, Minghui Lu, and Yun Jing. Magic-angle bilayer phononic graphene. *Phys. Rev. B*, 102:180304, Nov 2020.

[57] Mourad Oudich, Yuanchen Deng, and Yun Jing. Twisted pillared phononic crystal plates. *Applied Physics Letters*, 120(23):232202, 2022.

[58] Danilo Beli, Matheus Inguaggiato Nora Rosa, Carlos De Marqui, and Massimo Ruzzene. Wave beaming and diffraction in quasicrystalline elastic metamaterial plates. *Phys. Rev. Res.*, 4:043030, Oct 2022.

[59] Jenny Hoffman. Simulating twistronics in acoustic metamaterials. In *APS March Meeting Abstracts*, volume 2022 of *APS Meeting Abstracts*, page A44.001, January 2022.

[60] S Minhal Gardezi, Harris Pirie, Stephen Carr, William Dorrell, and Jennifer E Hoffman. Simulating twistronics in acoustic metamaterials. *2D Materials*, 8(3):031002, apr 2021.

[61] María Rosendo López, Zhiwang Zhang, Daniel Torrent, and Johan Christensen. Theory of holey twistsonic media. *Communications Materials*, 3(1):99, 2022.

[62] Shi-Qiao Wu, Zhi-Kang Lin, Bin Jiang, Xiaoxi Zhou, Zhi Hong Hang, Bo Hou, and Jian-Hua Jiang. Higher-order topological states in acoustic twisted moiré superlattices. *Phys. Rev. Appl.*, 17:034061, Mar 2022.

[63] Simon Yves, Yu-Gui Peng, and Andrea Alù. Topological lifshitz transition in twisted hyperbolic acoustic metasurfaces. *Applied Physics Letters*, 121(12):122201, 2022.

[64] Patrick Zeller and Sebastian Günther. What are the possible moiré patterns of graphene on hexagonally packed surfaces? universal solution for hexagonal coincidence lattices, derived by a geometric construction. *New Journal of Physics*, 16(8):083028, aug 2014.

[65] José L. Aragón, Gerardo G. Naumis, and Alfredo Gómez-Rodríguez. Twisted graphene bilayers and quasicrystals: A cut and projection approach. *Crystals*, 9(10), 2019.

[66] Guy Bouchitté, Sébastien Guenneau, and Frédéric Zolla. Homogenization of dielectric photonic quasi crystals. *Multiscale Modeling & Simulation*, 8(5):1862–1881, 2010.

[67] Grigory Tarnopolsky, Alex Jura Kruchkov, and Ashvin Vishwanath. Origin of magic angles in twisted bilayer graphene. *Phys. Rev. Lett.*, 122:106405, Mar 2019.

[68] Niklas Wellander, Sebastién Guenneau, and Elena Cherkaev. Two-scale cut-and-projection convergence; homogenization of quasiperiodic structures. *Mathematical Methods in the Applied Sciences*, 41(3):1101–1106, 2018.

[69] Yi Chen, Muamer Kadic, Sébastien Guenneau, and Martin Wegener. Isotropic chiral acoustic phonons in 3d quasicrystalline metamaterials. *Phys. Rev. Lett.*, 124:235502, Jun 2020.

[70] S Shallcross, S Sharma, E Kandelaki, and OA Pankratov. Electronic structure of turbostratic graphene. *Physical Review B*, 81(16):165105, 2010.

[71] Xiao-Liang Qi, Taylor L. Hughes, and Shou-Cheng Zhang. Topological field theory of time-reversal invariant insulators. *Phys. Rev. B*, 78:195424, Nov 2008.

[72] Andreas P. Schnyder, Shinsei Ryu, Akira Furusaki, and Andreas W. W. Ludwig. Classification of topological insulators and superconductors in three spatial dimensions. *Phys. Rev. B*, 78:195125, Nov 2008.

[73] Xiang Ni, Matthew Weiner, Andrea Alu, and Alexander B Khanikaev. Observation of higher-order topological acoustic states protected by generalized chiral symmetry. *Nature materials*, 18(2):113–120, 2019.

[74] Karmela Padavić, Suraj S. Hegde, Wade DeGottardi, and Smitha Vishveshwara. Topological phases, edge modes, and the hofstadter butterfly in coupled su-schrieffer-heeger systems. *Phys. Rev. B*, 98:024205, Jul 2018.

[75] F. D. M. Haldane and S. Raghu. Possible realization of directional optical waveguides in photonic crystals with broken time-reversal symmetry. *Phys. Rev. Lett.*, 100:013904, Jan 2008.

[76] Emil Prodan and Camelia Prodan. Topological phonon modes and their role in dynamic instability of microtubules. *Phys. Rev. Lett.*, 103:248101, Dec 2009.

[77] Zheng Wang, Yidong Chong, John D Joannopoulos, and Marin Soljačić. Observation of unidirectional backscattering-immune topological electromagnetic states. *Nature*, 461(7265):772–775, 2009.

[78] Long-Hua Wu and Xiao Hu. Scheme for achieving a topological photonic crystal by using dielectric material. *Phys. Rev. Lett.*, 114:223901, Jun 2015.

[79] Zhaoju Yang, Fei Gao, Xihang Shi, Xiao Lin, Zhen Gao, Yidong Chong, and Baile Zhang. Topological acoustics. *Phys. Rev. Lett.*, 114:114301, Mar 2015.

[80] Cheng He, Xu Ni, Hao Ge, Xiao-Chen Sun, Yan-Bin Chen, Ming-Hui Lu, Xiao-Ping Liu, and Yan-Feng Chen. Acoustic topological insulator and robust one-way sound transport. *Nature physics*, 12(12):1124–1129, 2016.

[81] David J Apigo, Wenting Cheng, Kyle F Dobiszewski, Emil Prodan, and Camelia Prodan. Observation of topological edge modes in a quasiperiodic acoustic waveguide. *Physical review letters*, 122(9):095501, 2019.

[82] Matheus I. N. Rosa, Yuning Guo, and Massimo Ruzzene. Exploring topology of 1d quasiperiodic metastructures through modulated lego resonators. *Applied Physics Letters*, 118(13):131901, 2021.

[83] Antonio Acín, Immanuel Bloch, Harry Buhrman, Tommaso Calarco, Christopher Eichler, Jens Eisert, Daniel Esteve, Nicolas Gisin, Steffen J Glaser, Fedor Jelezko, et al. The quantum technologies roadmap: a european community view. *New Journal of Physics*, 20(8):080201, 2018.

[84] B. Van Damme, L. Matar, G. Hannema, D. Tallarico, A. Zemp, and A. Bergamini. Bending-wave localization and interaction band gaps in quasiperiodic beams. *Phys. Rev. B*, 103:094301, Mar 2021.

[85] David J Apigo, Kai Qian, Camelia Prodan, and Emil Prodan. Topological edge modes by smart patterning. *Physical Review Materials*, 2(12):124203, 2018.

[86] Noah P Mitchell, Lisa M Nash, Daniel Hexner, Ari M Turner, and William TM Irvine. Amorphous topological insulators constructed from random point sets. *Nature Physics*, 14(4):380–385, 2018.

[87] Bogdan Ungureanu, Mehul P. Makwana, Richard V. Craster, and Sébastien Guenneau. Localizing elastic edge waves via the topological rainbow effect. *Phys. Rev. Appl.*, 15:014057, Jan 2021.

[88] SM Kuznetsova, Jean-Philippe Groby, LM García-Raffi, and Vicente Romero-García. Localized interface modes in one-dimensional hyperuniform acoustic materials. *Journal of Physics D: Applied Physics*, 54(31):315303, 2021.

[89] Penglin Gao, Daniel Torrent, Francisco Cervera, Pablo San-Jose, José Sánchez-Dehesa, and Johan Christensen. Majorana-like zero modes in kekulé distorted sonic lattices. *Phys. Rev. Lett.*, 123:196601, Nov 2019.

[90] Zhihui Wen, Yabin Jin, Penglin Gao, Xiaoying Zhuang, Timon Rabczuk, and Bahram Djafari-Rouhani. Topological cavities in phononic plates for robust energy harvesting. *Mechanical Systems and Signal Processing*, 162:108047, 2022.

[91] Pawel Packo, Andrew N. Norris, and Daniel Torrent. Inverse grating problem: Efficient design of anomalous flexural wave reflectors and refractors. *Phys. Rev. Appl.*, 11:014023, Jan 2019.

[92] Marc Martí-Sabaté and Dani Torrent. Dipolar localization of waves in twisted phononic crystal plates. *Phys. Rev. Appl.*, 15:L011001, Jan 2021.

[93] Pawel Packo, Andrew N. Norris, and Dani Torrent. Metaclusters for the full control of mechanical waves. *Phys. Rev. Appl.*, 15:014051, Jan 2021.

[94] Raj Kumar Pal, Matheus IN Rosa, and Massimo Ruzzene. Topological bands and localized vibration modes in quasiperiodic beams. *New Journal of Physics*, 21(9):093017, 2019.

[95] Douglas R Hofstadter. Energy levels and wave functions of bloch electrons in rational and irrational magnetic fields. *Physical review B*, 14(6):2239, 1976.

[96] Xingbo Pu, Antonio Palermo, and Alessandro Marzani. Topological edge states of quasiperiodic elastic metasurfaces. *Mechanical Systems and Signal Processing*, 181:109478, 2022.

[97] Yiwei Xia, Alper Erturk, and Massimo Ruzzene. Topological edge states in quasiperiodic locally resonant metastructures. *Phys. Rev. Appl.*, 13:014023, Jan 2020.

[98] Mohit Gupta and Massimo Ruzzene. Dynamics of quasiperiodic beams. *Crystals*, 10(12), 2020.

[99] Tanmoy Chatterjee, Danilo Karličić, Milan Cajić, Sondipon Adhikari, and Michael I. Friswell. Uncertainty quantification in inerter-based quasiperiodic lattices. *International Journal of Mechanical Sciences*, 249:108258, 2023.

[100] Rudolph Peierls. Zur theorie des diamagnetismus von leitungselektronen. *Zeitschrift für Physik*, 80(11-12):763–791, 1933.

[101] Artur Avila and Svetlana Jitomirskaya. The ten martini problem. *Annals of mathematics*, pages 303–342, 2009.

[102] C. Janot. *Quasicrystals*, pages 197–211. Springer Berlin Heidelberg, Berlin, Heidelberg, 1994.

[103] Ilyasse Quotane, El Houssaine El Boudouti, and Bahram Djafari-Rouhani. Trapped-mode-induced fano resonance and acoustical transparency in a one-dimensional solid-fluid phononic crystal. *Phys. Rev. B*, 97:024304, Jan 2018.

[104] Yabin Jin, EI Houssaine EI Boudouti, Yan Pennec, and Bahram Djafari-Rouhani. Tunable fano resonances of lamb modes in a pillared metasurface. *Journal of Physics D: Applied Physics*, 50(42):425304, sep 2017.

[105] Seiji Mizuno. Fano resonances and bound states in the continuum in a simple phononic system. *Applied Physics Express*, 12(3):035504, feb 2019.

[106] Madiha Amrani, Ilyasse Quotane, Cecile Ghouila-Houri, El Houssaine El Boudouti, Leonid Krutyansky, Bogdan Piwakowski, Philippe Pernod, Abdelkrim Talbi, and Bahram Djafari-Rouhani. Experimental evidence of the existence of bound states in the continuum and fano resonances in solid-liquid layered media. *Phys. Rev. Appl.*, 15:054046, May 2021.

[107] Lujun Huang, Bin Jia, Artem S. Pilipchuk, Yankei Chiang, Sibo Huang, Junfei Li, Chen Shen, Evgeny N. Bulgakov, Fu Deng, David A. Powell, Steven A. Cummer, Yong Li, Almas F. Sadreev, and Andrey E. Miroshnichenko. General framework of bound states in the continuum in an open acoustic resonator. *Phys. Rev. Appl.*, 18:054021, Nov 2022.

[108] T. Mrabti, Z. Labdouti, A. Mouadili, E.H. El Boudouti, and B. Djafari-Rouhani. Aharonov-bohm-effect induced transparency and reflection in mesoscopic rings side coupled to a quantum wire. *Physica E: Low-dimensional Systems and Nanostructures*, 116:113770, 2020.

[109] T. Mrabti, Z. Labdouti, O. El Abouti, E.H. El Boudouti, F. Fethi, and B. Djafari-Rouhani. Transmission gaps, trapped modes and fano resonances in aharonov–bohm connected mesoscopic loops. *Physics Letters A*, 382(9):613–620, 2018.

[110] Chia Wei Hsu, Bo Zhen, Song-Liang Chua, Steven G Johnson, John D Joannopoulos, and Marin Soljačić. Bloch surface eigenstates within the radiation continuum. *Light: Science & Applications*, 2(7):e84–e84, 2013.

[111] Almas F Sadreev. Interference traps waves in an open system: bound states in the continuum. *Reports on Progress in Physics*, 84(5):055901, apr 2021.

[112] Evgeny N. Bulgakov and Almas F. Sadreev. Bound states in the continuum in photonic waveguides inspired by defects. *Phys. Rev. B*, 78:075105, Aug 2008.

[113] Feng Wu, Jiaju Wu, Zhiwei Guo, Haitao Jiang, Yong Sun, Yunhui Li, Jie Ren, and Hong Chen. Giant enhancement of the goos-hänchen shift assisted by quasibound states in the continuum. *Phys. Rev. Appl.*, 12:014028, Jul 2019.

[114] Filiz Yesilkoy, Eduardo R Arvelo, Yasaman Jahani, Mingkai Liu, Andreas Tittl, Volkan Cevher, Yuri Kivshar, and Hatice Altug. Ultrasensitive hyperspectral imaging and biodetection enabled by dielectric metasurfaces. *Nature Photonics*, 13(6):390–396, 2019.

[115] Lucca Kühner, Luca Sortino, Rodrigo Berté, Juan Wang, Haoran Ren, Stefan A Maier, Yuri Kivshar, and Andreas Tittl. Radial bound states in the continuum for polarization-invariant nanophotonics. *Nature communications*, 13(1):4992, 2022.

[116] Alireza Taghizadeh, Jesper Mørk, and Il-Sug Chung. Ultracompact resonator with high quality-factor based on a hybrid grating structure. *Opt. Express*, 23(11):14913–14921, Jun 2015.

[117] Haoran Zhang, Tao Wang, Jingyi Tian, Jiacheng Sun, Shaoxian Li, Israel De Leon, Remo Proietti Zaccaria, Liang Peng, Fei Gao, Xiao Lin, Hongsheng Chen, and Gaofeng Wang. Quasi-bic laser enabled by high-contrast grating resonator for gas detection. *Nanophotonics*, 11(2):297–304, 2022.

[118] Gunjan Yadav, Subrat Sahu, Ritesh Kumar, and Rajan Jha. Bound states in the continuum empower subwavelength gratings for refractometers in visible. *Photonics*, 9(5), 2022.

[119] A. S. Lal Krishna, Sruti Menon, Asish Prosad, and Varun Raghunathan. Mid-infrared quasi-bic resonances with sub-wavelength slot mode profiles in germanium-based coupled guided-mode resonance structures. *Photon. Res.*, 10(1):68–75, Jan 2022.

[120] Feng Wu, Ma Luo, Jiaju Wu, Caifu Fan, Xin Qi, Yiran Jian, Dejun Liu, Shuyuan Xiao, Gengyan Chen, Haitao Jiang, Yong Sun, and Hong Chen. Dual quasibound states in the continuum in compound grating waveguide structures for large positive and negative goos-hänchen shifts with perfect reflection. *Phys. Rev. A*, 104:023518, Aug 2021.

[121] Ivan V. Timofeev, Dmitrii N. Maksimov, and Almas F. Sadreev. Optical defect mode with tunable q factor in a one-dimensional anisotropic photonic crystal. *Phys. Rev. B*, 97:024306, Jan 2018.

[122] Jicheng Jin, Xuefan Yin, Liangfu Ni, Marin Soljačić, Bo Zhen, and Chao Peng. Topologically enabled ultrahigh-q guided resonances robust to out-of-plane scattering. *Nature*, 574(7779):501–504, 2019.

[123] Zhaojian Zhang, Junbo Yang, Te Du, Hansi Ma, and Xinpeng Jiang. Tailoring bound states in the continuum in symmetric photonic crystal slabs by coupling strengths. *Opt. Express*, 30(5):8049–8062, Feb 2022.

[124] Shengyan Liu, Hao Tong, and Kejie Fang. Optomechanical crystal with bound states in the continuum. *nature communications*, 13(1):3187, 2022.

[125] Alireza Taghizadeh and Il-Sug Chung. Quasi bound states in the continuum with few unit cells of photonic crystal slab. *Applied Physics Letters*, 111(3), 07 2017. 031114.

[126] Lei Huang, Weixuan Zhang, and Xiangdong Zhang. Moiré quasibound states in the continuum. *Phys. Rev. Lett.*, 128:253901, Jun 2022.

[127] H.J. Putley, G.J. Chaplain, H. Rakotoarimanga-Andrianjaka, B. Maling, and R.V. Craster. Whispering-bloch elastic circuits. *Wave Motion*, 105:102755, 2021.

[128] Alexander B. Movchan, Ross C. McPhedran, and Giorgio Carta. Scattering reduction and resonant trapping of flexural waves: Two rings to rule them. *Applied Sciences*, 11(10), 2021.

[129] AB Movchan, RC McPhedran, G Carta, and RV Craster. Platonic localisation: one ring to bind them. *Archive of Applied Mechanics*, 89:521–533, 2019.

[130] Noé Jiménez, Olga Umnova, and Jean-Philippe Groby. Acoustic waves in periodic structures, metamaterials, and porous media. *Ch. the Transfer Matrix Method in Acoustics, Springer International Publishing, Cham*, pages 103–164, 2021.

[131] Pawel Packo, Andrew N Norris, and Dani Torrent. Metaclusters for the full control of mechanical waves. *Physical Review Applied*, 15(1):014051, 2021.

[132] Mario I. Molina, Andrey E. Miroshnichenko, and Yuri S. Kivshar. Surface bound states in the continuum. *Phys. Rev. Lett.*, 108:070401, Feb 2012.

[133] Andrey E. Miroshnichenko, Sergej Flach, and Yuri S. Kivshar. Fano resonances in nanoscale structures. *Rev. Mod. Phys.*, 82:2257–2298, Aug 2010.

[134] Bo Zhen, Chia Wei Hsu, Ling Lu, A. Douglas Stone, and Marin Soljačić. Topological nature of optical bound states in the continuum. *Phys. Rev. Lett.*, 113:257401, Dec 2014.

[135] H. Friedrich and D. Wintgen. Interfering resonances and bound states in the continuum. *Phys. Rev. A*, 32:3231–3242, Dec 1985.

[136] Ashok Kodigala, Thomas Lepetit, Qing Gu, Babak Bahari, Yeshaiahu Fainman, and Boubacar Kanté. Lasing action from photonic bound states in continuum. *Nature*, 541(7636):196–199, 2017.

[137] Kirill Koshelev, Andrey Bogdanov, and Yuri Kivshar. Meta-optics and bound states in the continuum. *Science Bulletin*, 64(12):836–842, 2019. SPECIAL TOPIC: Electromagnetic Metasurfaces: from Concept to Applications.

[138] Mengfei Wu, Son Tung Ha, Sushant Shendre, Emek G Durmusoglu, Weon-Kyu Koh, Diego R Abujetas, José A Sánchez-Gil, Ramón Paniagua-Domínguez, Hilmi Volkan Demir, and Arseniy I Kuznetsov. Room-temperature lasing in colloidal nanoplatelets via mie-resonant bound states in the continuum. *Nano Letters*, 20(8):6005–6011, 2020.

[139] Kirill Koshelev, Sergey Kruk, Elizaveta Melik-Gaykazyan, Jae-Hyuck Choi, Andrey Bogdanov, Hong-Gyu Park, and Yuri Kivshar. Subwavelength dielectric resonators for nonlinear nanophotonics. *Science*, 367(6475):288–292, 2020.

[140] Roman Gansch, Stefan Kalchmair, Patrice Genevet, Tobias Zederbauer, Hermann Detz, Aaron M Andrews, Werner Schrenk, Federico Capasso, Marko Lončar, and Gottfried Strasser. Measurement of bound states in the continuum by a detector embedded in a photonic crystal. *Light: Science & Applications*, 5(9):e16147–e16147, 2016.

[141] Federico Capasso, Carlo Sirtori, Jerome Faist, Deborah L Sivco, Sung-Nee G Chu, and Alfred Y Cho. Observation of an electronic bound state above a potential well. *Nature*, 358(6387):565–567, 1992.

[142] Yonatan Plotnik, Or Peleg, Felix Dreisow, Matthias Heinrich, Stefan Nolte, Alexander Szameit, and Mordechai Segev. Experimental observation of optical bound states in the continuum. *Phys. Rev. Lett.*, 107:183901, Oct 2011.

[143] Tan Shi, Zi-Lan Deng, Guangzhou Geng, Xianzhi Zeng, Yixuan Zeng, Guangwei Hu, Adam Overvig, Junjie Li, Cheng-Wei Qiu, Andrea Alù, et al. Planar chiral metasurfaces with maximal and tunable chiroptical response driven by bound states in the continuum. *Nature Communications*, 13(1):4111, 2022.

[144] Yang Chen, Huachun Deng, Xinbo Sha, Weijin Chen, Ruize Wang, Yu-Hang Chen, Dong Wu, Jiaru Chu, Yuri S Kivshar, Shumin Xiao, et al. Observation of intrinsic chiral bound states in the continuum. *Nature*, 613(7944):474–478, 2023.

[145] P. J. Cobelli, V. Pagneux, A. Maurel, and P. Petitjeans. Experimental observation of trapped modes in a water wave channel. *Europhysics Letters*, 88(2):20006, nov 2009.

[146] Sibo Huang, Tuo Liu, Zhiling Zhou, Xu Wang, Jie Zhu, and Yong Li. Extreme sound confinement from quasibound states in the continuum. *Phys. Rev. Appl.*, 14:021001, Aug 2020.

[147] Lujun Huang, Bin Jia, Yan Kei Chiang, Sibo Huang, Chen Shen, Fu Deng, Tianzhi Yang, David A Powell, Yong Li, and Andrey E Miroshnichenko. Topological supercavity resonances in the finite system. *Advanced Science*, 9(20):2200257, 2022.

[148] Lujun Huang, Yan Kei Chiang, Sibo Huang, Chen Shen, Fu Deng, Yi Cheng, Bin Jia, Yong Li, David A Powell, and Andrey E Miroshnichenko. Sound trapping in an open resonator. *Nature communications*, 12(1):4819, 2021.

[149] *Mode-Matching Method*, chapter 8, pages 191–235. John Wiley and Sons, Ltd.

[150] Daniel Torrent. Acoustic anomalous reflectors based on diffraction grating engineering. *Physical Review B*, 98(6):060101, 2018.

[151] Daniel Torrent and José Sánchez-Dehesa. Acoustic analogue of graphene: Observation of dirac cones in acoustic surface waves. *Phys. Rev. Lett.*, 108:174301, Apr 2012.

[152] Marc Martí-Sabaté, Bahram Djafari-Rouhani, and Dani Torrent. Bound states in the continuum in circular clusters of scatterers. *Phys. Rev. Res.*, 5:013131, Feb 2023.

[153] HJ Putley, GJ Chaplain, H Rakotoarimanga-Andrianjaka, B Maling, and RV Craster. Whispering-bloch elastic circuits. *Wave Motion*, 105:102755, 2021.

[154] Cyril M Harris. Absorption of sound in air versus humidity and temperature. *The Journal of the Acoustical Society of America*, 40(1):148–159, 1966.

[155] Izrail Solomonovich Gradshteyn and Iosif Moiseevich Ryzhik. *Table of integrals, series, and products*. Academic press, 2014.

Appendix A

Continuous limit of the cluster's Green's function

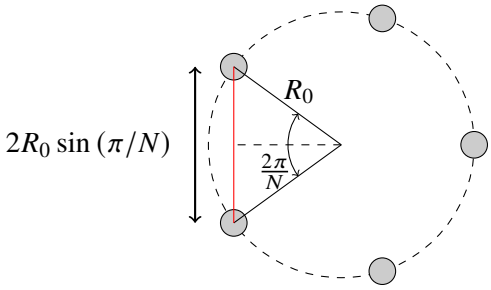

Figure A.1: Cluster's geometry.

In this appendix we will derive an analytical expression for the sum S_R^ℓ when the number of scatterers in the circular array tends to infinite. According to Fig. A.1, the scatterers in the cluster are placed in the vertices of a regular polygon of N sides, thus the position of the α scatterer is given by

$$\boldsymbol{R}_\alpha = R_0 \cos\left(\frac{2\pi\alpha}{N}\right)\hat{\boldsymbol{x}} + R_0 \sin\left(\frac{2\pi\alpha}{N}\right)\hat{\boldsymbol{y}} \tag{A.1}$$

In the limit of $N \longrightarrow \infty$, the variable $\theta_\alpha = 2\pi\alpha/N$ can be substituted by a continuous variable $\theta \in [0, 2\pi]$, such that $d\theta = 2\pi/N$. Also, the distance $R_{0\alpha}$ between the scatterer of reference and any scatterer in the cluster is, according to Fig. A.1,

$$R_{0\alpha} = 2R_0 \sin\frac{\pi}{N} \tag{A.2}$$

which, in the limit $N \longrightarrow \infty$ becomes

$$R(\theta) = 2R_0 \sin\frac{\theta}{2} \tag{A.3}$$

Thus, we can write

$$\lim_{N\to\infty}\frac{1}{N}S_R^\ell = \frac{1}{2\pi}\mathrm{Re}\int_0^{2\pi}\xi(\theta)e^{i\ell\theta}d\theta. \tag{A.4}$$

with

$$\xi(\theta) = H_0(k_0R(\theta)) + \frac{2i}{\pi}K_0(k_0R(\theta)), \tag{A.5}$$

For $\ell = 0$ we have

$$\begin{aligned}\lim_{N\to\infty}\frac{1}{N}S_R^0 &= \frac{1}{2\pi}\int_0^{2\pi}J_0(2k_0R_0\sin(\theta/2))d\theta \\ &= \frac{2}{\pi}\int_0^{\pi/2}J_0(2k_0R_0\sin\theta)d\theta.\end{aligned} \tag{A.6}$$

By using the following identity [155]

$$\int_0^{\pi/2}J_{2\nu}(2z\sin x)dx = \frac{\pi}{2}J_\nu^2(z), \tag{A.7}$$

where ν is the order of the Bessel function. For $\nu = 0$, we arrive to

$$\boxed{\lim_{N\to\infty}\frac{1}{N}S_R^0 = J_0^2(k_0R_0)} \tag{A.8}$$

Similarly, for $\ell \neq 0$, we have now

$$\lim_{N\to\infty}\frac{1}{N}S_R^\ell = \frac{1}{2\pi}\mathrm{Re}\int_0^{2\pi}\chi_\theta e^{il\theta}d\theta \tag{A.9}$$

thus

$$\begin{aligned}&\frac{1}{2\pi}\int_0^{2\pi}J_0(2k_0R_0\sin\theta/2)e^{il\theta}d\theta \\ &= \frac{1}{(2\pi)^2}\int_0^{2\pi}\int_{-\pi}^{\pi}e^{-i2k_0R_0\sin(\theta/2)\sin\tau}e^{il\theta}d\tau d\theta \\ &= \frac{1}{2\pi^2}\int_0^{\pi}\int_{-\pi}^{\pi}e^{-i2k_0R_0\sin(\theta)\sin\tau}e^{2il\theta}d\tau d\theta \\ &= \frac{(-1)^{2l}}{2\pi}\int_{-\pi}^{\pi}J_{2l}(2k_0R_0\sin\tau)d\tau \\ &= \frac{2(-1)^{2l}}{\pi}\int_0^{\pi/2}J_{2l}(2k_0R_0\sin\tau)d\tau\end{aligned} \tag{A.10}$$

so that we have

$$\boxed{\lim_{N\to\infty}\frac{1}{N}S_R^\ell = J_\ell^2(k_0R)} \tag{A.11}$$

Appendix B

$H_{\alpha G}$ simplification

Simplification of the $H_{\alpha G}$ function considering that all the holes have the same geometry: $|\boldsymbol{R}_\alpha| = R_a$, $L_\alpha = L_a$.

$$H_{\alpha G} = \frac{1}{\Omega_\alpha} \int_{\Omega_\alpha} e^{i\boldsymbol{k_G}(\boldsymbol{r}-\boldsymbol{R}_\alpha)} d\Omega_\alpha. \tag{B.1}$$

We expand the plane with by means of Jacobi-Anger expansion:

$$H_{\alpha G} = \frac{1}{\Omega_\alpha} \int_{\Omega_\alpha} \sum_{n=-\infty}^{+\infty} i^n J_n(|\boldsymbol{k_G}||\boldsymbol{r}-\boldsymbol{R}_\alpha|) e^{in(\theta_{k_G}-\theta_{r-R_\alpha})} d\Omega_\alpha. \tag{B.2}$$

We change the origin of coordinates to the centre of the scatterer, such that $\boldsymbol{r'} = \boldsymbol{r} - \boldsymbol{R}_\alpha$ and $\theta = \theta_{r-R_\alpha}$,

$$H_{\alpha G} = \frac{1}{\Omega_\alpha} \int_{\Omega_\alpha} \sum_{n=-\infty}^{+\infty} i^n J_n(|\boldsymbol{k_G}||\boldsymbol{r'}|) e^{in(\theta_{k_G}-\theta)} d\Omega_\alpha. \tag{B.3}$$

Now we change to cylindrical coordinates

$$H_{\alpha G} = \frac{1}{\pi R_a^2} \int_0^{R_a} \int_0^{2\pi} r' \sum_{n=-\infty}^{+\infty} i^n J_n(|\boldsymbol{k_G}|r') e^{in(\theta_{k_G}-\theta)} d\theta dr'. \tag{B.4}$$

The integral over the angular coordinate is trivial. It is zero unless $n = 0$, which gives 2π.

$$H_{\alpha G} = \frac{2}{R_a^2} \int_0^{R_a} r' J_0(|\boldsymbol{k_G}|r') dr'. \tag{B.5}$$

For this second integral, we will make a change of variable, such that $x = |\boldsymbol{k_G}|r'$

$$H_{\alpha G} = \frac{2}{R_a^2 |\boldsymbol{k_G}|^2} \int_0^{|\boldsymbol{k_G}|R_a} x J_0(x) dx, \tag{B.6}$$

and the solution for this integral is well known (5.56 in [155]),

$$H_{\alpha G} = \frac{2}{R_a^2} \frac{|\boldsymbol{k_G}| R_a J_1(|\boldsymbol{k_G}| R_a)}{|\boldsymbol{k_G}|^2}, \tag{B.7}$$

which in the end gives

$$\boxed{H_G = \frac{2}{|\boldsymbol{k_G}| R_a} J_1(|\boldsymbol{k_G}| R_a)} \tag{B.8}$$

Appendix C

Uncovered plate

C.1 BIC's design

In this section, the main equations describing the behaviour of the system will be developed and discussed, as well as the design procedure for a later realization and experimental test of the sample.

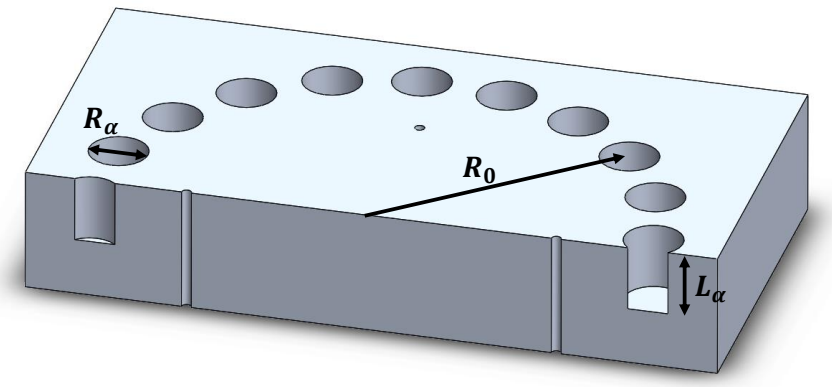

Figure C.1: Illustration of a section of the plate, with the input channels used for the external excitation.

Since we are interested in the proper modes of the system, we are going to consider that there is no incident field, i.e., $A_G = 0$. Then, the acoustic pressure field and the normal velocity field can be written

$$P(\boldsymbol{r}) = \sum_{\boldsymbol{G}} B_G e^{-iq_G z} e^{i\boldsymbol{k_G}\cdot\boldsymbol{r}} \tag{C.1}$$

$$v_n(\boldsymbol{r}) = \sum_{\boldsymbol{G}} \frac{-iq_G}{k_b z_b} B_G e^{-iq_G z} e^{i\boldsymbol{k_G}\cdot\boldsymbol{r}}, \tag{C.2}$$

being z_b the acoustic impedance of the medium. Concerning the acoustic field inside the holes, only the main resonance of each hole will be considered, and the boundaries with the solid material are considered rigid. Therefore, the pressure field and the normal velocity field inside the hole can be approximated by

Once the fields in the cavities and the waveguide have been described, mode matching at the top surface of the rigid plate ($z = 0$) is applied in order to match modes from both domains. Applying continuity to the integral of the pressure field in the area of a hole and continuity of the velocity field in the unit cell [150, 151], two equations are obtained:

$$\sum_{\boldsymbol{G}} B_G e^{i\boldsymbol{G}\cdot\boldsymbol{R}_\alpha} H_{\alpha G} = B_\alpha \cot(k_b L_\alpha) \tag{C.3}$$

and

$$\frac{-iq_G}{k_b} B_G = \sum_{\beta} f_\beta e^{-i\boldsymbol{G}\cdot\boldsymbol{R}_\beta} H_{\beta G} B_\beta, \tag{C.4}$$

where $H_{\alpha G} = \frac{1}{\Omega_\alpha}\int_{\Omega_\alpha} e^{i\boldsymbol{k_G}(\boldsymbol{r}-\boldsymbol{R}_\alpha)} d\Omega_\alpha$ and $f_\alpha = \frac{\Omega_\alpha}{\Omega_C}$ is the cavity's filling fraction, with Ω_c and Ω_α being the areas of the unit cell and the cavity α. After substituting B_G coefficients from equation (C.4) into equation (C.3), we get a system of equations such that:

$$\sum_{\beta} \left[\delta_{\alpha\beta}\cot(k_b L_\alpha) - i\chi_{\alpha\beta}\right] B_\beta = 0, \tag{C.5}$$

Therefore,

$$\chi_{\alpha\beta} = \sum_{G} \frac{4\pi k_b}{|\boldsymbol{k_G}|^2 q_G \Omega_c} J_1^2(|\boldsymbol{k_G}|R_a) e^{i\boldsymbol{G}\cdot\boldsymbol{R}_{\alpha\beta}}. \tag{C.6}$$

$$\chi_{\alpha\beta} = 2\sum_{n=-\infty}^{+\infty} (-1)^n e^{-2\pi i\beta n/N} e^{2\pi i\alpha n/N} I_{uncov}(n), \tag{C.7}$$

where

$$I_{uncov}(n) = \int_0^{+\infty} \frac{k_b}{q_k k} J_1^2(kR_a) J_n^2(kR_0) dk. \tag{C.8}$$

The integral term $I_{uncov}(n)$ has both real and imaginary part. The system of equations (C.5) gets reduced to a single equation, decoupled in two different conditions

$$\cot(k_b L_\alpha) = 2N(-1)^\ell \int_{k_b}^{\infty} \frac{k_b}{k|q_k|} J_1^2(kR_a) J_\ell^2(kR_0) dk \tag{C.9}$$

$$0 = \int_0^{k_b} \frac{k_b}{k|q_k|} J_1^2(kR_a) J_\ell^2(kR_0) dk. \tag{C.10}$$

Equation (C.10) can not be satisfied, avoiding the possibility of having a real BIC for the uncovered plate. A mode with good quality factor can be designed by properly matching the frequency and the radius of the cluster to coincide with one of the zeros of $J_\ell^2(kR_0)$. Then, evaluating the integral term in equation (C.9), a value for the depth of the holes can be obtained.

By numerically analysing equation (C.10) we will be able to properly tune the resonant mode.

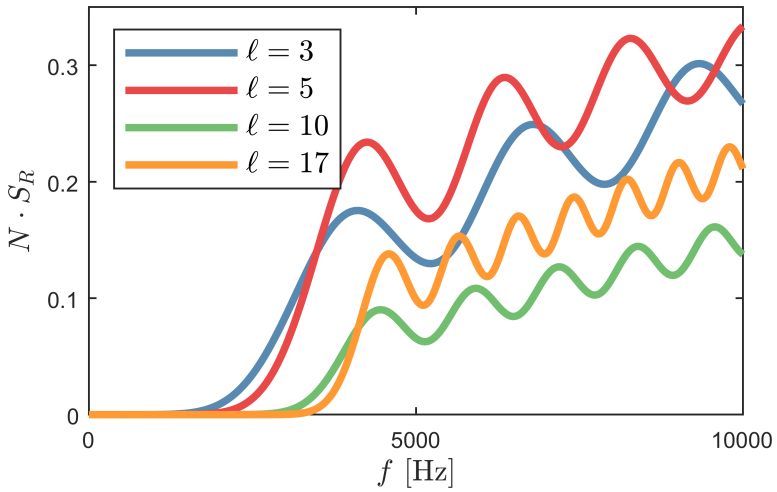

Figure C.2: S_R integral defined in equation (C.10) for four different resonant index ℓ.

Figure C.2 panel **a** shows the evolution of S_R as a function of the frequency. As mentioned before, this function cannot be cancelled, avoiding any possible solution for a BIC. Notwithstanding, the S_R function has a modulation with a series of minima; these minima are given by the zeros of the Bessel term $J_\ell^2(kR_0)$ (remember that this is the function in the integrand that controls the behaviour at low frequency, while $J_1^2(kR_a)$ controls the high frequency behaviour). One of this minima will be selected for the resonance of the mode. The minima of the function are the points closer to 0; therefore, they are supposed to give higher quality factors than other points for the uncovered structure.

C.2 Simulation and experiment

A $\ell = 2$ mode has been designed for the uncovered system. The geometrical parameters resulting from the design are: $R_0 = 5.6$ cm, $R_\alpha = 5.9$ mm, $L_\alpha = 1.35$ cm and the frequency is $f = 5$ kHz. In the following, FEM simulations with COMSOL Multiphysics Pressure Acoustic module and experimental results of this mode will be shown.

The simulated domain is a cylinder with radius $R_{cyl} = 3R_0$. A perfectly matched layer is adopted as the top boundary in order to reduce reflections, while plane wave radiation boundary conditions are applied on the sides to simulate the propagation to an infinite system. Speed of sound is $344m/s$ (after measurement in the laboratory). Losses have been simulated by adding an imaginary component to the speed of sound. Furthermore, losses in the input channel have been simulated by applying cylindrical wave radiation boundary conditions in the bottom surface of the throughout holes connecting the bottom and top surface of the bottom plate. All boundaries between air and solid (glass or aluminium) have been considered rigid.

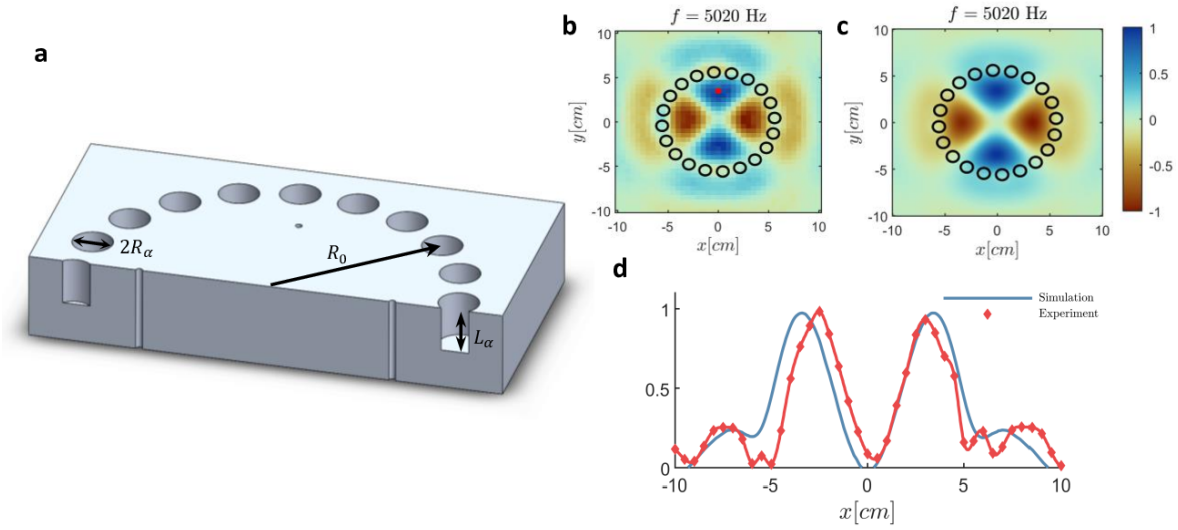

Figure C.3: Designed resonance and corresponding performance. Panel **a** provides an illustrative depiction of a plate section. The mode's normalized real pressure field is displayed in panels **b** and **c**, representing simulation and experiment, respectively. Furthermore, panel **d** exhibits the normalized absolute pressure field along the line $y = 0$, demonstrating a good level of agreement between the simulation and experimental data.

Figure C.3 panel **c** shows the normalized real pressure field for the designed $\ell = 2$ mode. As it can be seen from the pressure distribution, the field has the symmetry predicted by the resonant index, and the totality of the pressure field is confined inside the circle of holes. The quality factor of the structure found in simulation is not high: it is, in fact, below 10 without considering material loss. Panel **b** shows the real pressure field found in the real experiment. Panel **d** presents the comparison between simulation and experiment for the $y = 0$ line, showing a good level of agreement. However, this result is not as good as the one observed in the main text (Fig. 6.2 panel **d**) for the BIC.

The sample was fabricated by drilling twenty blind holes in aluminum with a CNC machine. The size of the plate is 18x18x1 inch. The diameter of the holes is $1/2$ inch. The four throughout holes corresponding to the input energy channels have also been drilled using a CNC machine. In this case, the diameter is $5/64$ inch ($\sim$ 2 mm). The pressure field has been measured by scanning the surface with a microphone attached to a magnet following the movement of a metallic rod outside the waveguide. Four speakers have been used as excitation system, emitting a pulse centered at 5 kHz and spannning from 4

kHz to 6 kHz. The amplitude of each speaker has been normalized to obtain the same spectral response on top of the speaker. The overall scanned area is 10 cm by 10 cm with a step of 0.5 cm. Each position is repeated several times and the resulting signal is time-averaged in order to reduce noise. Measurements shown here have been done under laboratory environmental conditions ($T = 21.5°$C and $HR = 10\%$).

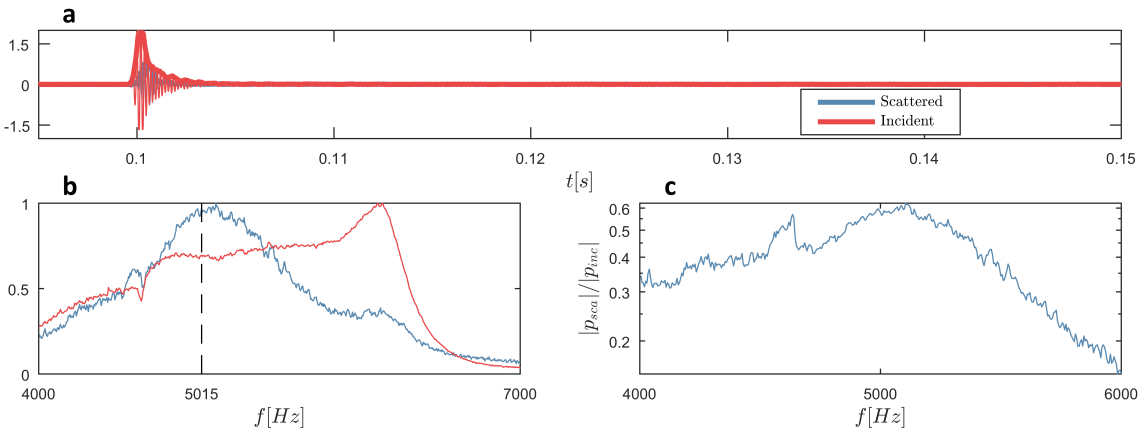

Figure C.4: Experimental results from the uncovered $\ell = 2$ designed plate. Panel **a** shows the incident and scattered signal and envelope at a given position ($x = 0$, $y = 35$ mm, $z = 22$ mm). Panel **b** shows the normalized spectrum for both the incident and the scattered field. Panel **c** shows the ratio between the scattered spectrum and the incident one in the experiment.

Figure C.4 presents the analysis for the uncovered plate experiment, with the same structure as in Fig. 6.3. Panel **a** shows the temporal signal, both for the incident (blue) and the scattered field (red). Compared to the Fig. 6.3, the tail of the scattered field is much shorter, indicating that there is no high-quality resonance present in the structure. Furthermore, in this case the scattered field is completely masked by the incident signal, while we had the opposite situation in the covered scenario. Panel **b** shows the spectral content of both fields (incident and scattered). They have been normalized for the sake of having a better visualization. It can be seen that the scattered field has its peak at the mode frequency. Even though, the resonance is much wider than the one shown in Fig. 6.3. Panel **c** depicts the ratio between the scattered spectrum and the incident one. The peak for this ratio is found at the mode frequency $\sim$ 5015 Hz. Once again, this result is different from the one in the covered case: there is no ratio higher than one, indicating that there is no field enhancement at any frequency, contrary to what was found in the covered waveguide.

Appendix D

Publications

D.1 International Journals

1. Marc Martí-Sabaté and Daniel Torrent. *Dipolar localization of waves in twisted phononic crystal plates.* Physical Review Applied, 15, L011001, 2021.

2. Marc Martí-Sabaté and Daniel Torrent. *Edge modes for flexural waves in quasi-periodic linear arrays of scatterers.* APL Materials, 9, 081107, 2021.

3. Marc Martí-Sabaté, Sébastien Guenneau and Daniel Torrent. *High-quality resonances in quasi-periodic clusters of scatterers for flexural waves.* AIP Advances, 12, 085303, 2022.

4. Marc Martí-Sabaté, Bahram Djafari-Rouhani and Daniel Torrent. *Bound states in the continuum in circular clusters of scatterers.* Physical Review Research, 5, 013131, 2023.

5. Marc Martí-Sabaté, Junfei Li, Bahram Djafari-Rouhani, Steven A. Cummer and Daniel Torrent. *Observation of two-dimensional acoustic bound states in the continuum.* arXiv:2306.15361, 2023. (Under review for Nature Communications)

D.2 International Meetings and Conferences

1. Marc Martí-Sabaté and Daniel Torrent. *Strong dipolar interaction in aperiodic Twisted Phononic Crystal Plates.* Metamaterials 2021. 2021 Fifteenth International Congress on Artificial Materials for Novel Wave Phenomena (Metamaterials), New York (USA), 2021.

2. Marc Martí-Sabaté and Daniel Torrent. *Multiple scattering analysis of resonant modes in quasi-periodic crystals*. Metamaterials XIII. SPIE Photonics Europe, Strasbourg (France), 2022.

3. Marc Martí-Sabaté, Sébastien Guenneau and Daniel Torrent. *Mode analysis in finite quasi-periodic arrays of scatterers for flexural waves.* Arctic Quasi Periodic Workshop, Luleå (Sweden), 2022.

4. Marc Martí-Sabaté and Daniel Torrent. *Multiple scattering analysis of quasi-periodic clusters of scatterers.* 19th U.S. National Congress on Theoretical and Applied Mechanics, Austin (USA), 2022.

5. Marc Martí-Sabaté, Sébastien Guenneau and Daniel Torrent. *High quality resonances in quasi-periodic distributions of scatterers.* META 2022, Torremolinos (Spain), 2022.

6. Marc Martí-Sabaté, Junfei Li, Bahram Djafari-Rouhani, Steven Cummer and Daniel Torrent. *Design and experimental verification of BICs in circular clusters of scatterers.* Multiple scattering in engineering and applied sciences workshop (MWSW04), Cambridge (United Kingdom), 2023.

7. Marc Martí-Sabaté and Daniel Torrent. *Multiple scattering analysis of the localization of flexural waves in thin elastic plates.* Multiple scattering in engineering and applied sciences workshop (MWSW04), Cambridge (United Kingdom), 2023.

8. Marc Martí-Sabaté, Junfei Li, Bahram Djafari-Rouhani, Steven Cummer and Daniel Torrent. *Tailoring bound states in the continuum by circular clusters of scatterers.* Phononics 2023: 6th International conference on phononic crystals/metamaterials/metasurfaces, phonon transport, topological transport, Manchester (United Kingdom), 2023.